The Biosynthesis of Opine Metallophores

By

Jeffrey S. McFarlane

B.S., Sterling College, 1997
M.A., Park University, 2002

Submitted to the graduate degree program in the Department of Molecular Biosciences and the Graduate Faculty of the University of Kansas in partial fulfillment of the requirements for the degree of Doctor of Philosophy

_____
Chairperson – Audrey Lamb

_____
Mark L. Richter

_____
Susan M. Egan

_____
Josephine Chandler

_____
Timothy Jackson

Date defended: 21 June, 2019

The dissertation committee for Jeffrey S. McFarlane certifies that this is the approved version of the following dissertation:

The Biosynthesis of Opine Metallophores

Chairperson – Audrey Lamb

Mark L. Richter

Susan M. Egan

Josephine Chandler

Timothy Jackson

Date approved: 21 June, 2019

Abstract

Metal acquisition is a necessity for all cells as metals are essential for the function of numerous metalloproteins and metalloenzymes. Bacterial pathogens employ several strategies for obtaining necessary metal including the direct import of metal ions, the import of metal-containing heme groups, and the secretion of biosynthesized small molecule metallophores to capture metals from the surrounding environment. Metallophore pathways are virulence factors that allow effective competition within the human host and the establishment of infection. They represent viable targets for the development of new antibiotic therapies and an understanding of the production and use of each metallophore contributes to a broader understanding of bacterial pathogenesis.

In 2015, Gi and Choi proposed the existence of a novel nicotianamine-like metallophore produced by two enzymes encoded in a four gene operon in *Pseudomonas aeruginosa*. Nicotianamines are plant-derived metallophores and *P. aeruginosa* biosynthesizes two well-studied metallophores, pyoverdin and pyochelin, making this hypothesis surprising. In 2016, Ghssein *et. al.* described a homologous system in *Staphylococcus aureus* producing a metallophore they named staphylopine biosynthesized by two primary enzymes, a nicotianamine synthase and an opine dehydrogenase.

Following heterologous expression of these two orthologous enzymes from the *P. aeruginosa* operon, a plate-reader screening assay was used to determine the substrates. With substrates known, the predicted structure of pseudopaline was confirmed by mass spectrometry. Pseudopaline is uses L-histidine and α-ketoglutarate as substrates in constrast to staphylopine which incorporates D-histidine and pyruvate. Steady-state kinetic parameters for the nicotianamine synthase in *S. aureus* and *P. aeruginosa* demonstrated slow k_{cat} values of 1.79 $\pm$ 0.02 and 1.07 $\pm$ 0.02 min^{-1} and K_m values of 13.0 $\pm$ 0.7 and 5.4 $\pm$ 0.4 μM respectively. Steady-state parameters had not been previously established for any nicotianamine synthase. This work

is detailed in chapter two. The recognition of the enzymatic determinants of opine metallophore production allowed targeted bioinformatics analyses that revealed the presence of like operons in disparate bacterial species living in diverse environments. These analyses are described in chapter one.

Opine dehydrogenase enzymes had been structurally characterized from two species (the soil bacterium *Arthrobacter* sp. 1C and the marine scallop *Pecten maximus*) prior to this work. *Yersinia pestis* has a homologous opine metallophore-producing operon. Heterologous expression of the *Y. pestis* opine dehydrogenase revealed a specificity for L-histidine and pyruvate, although expression of the *Y. pestis* nicotianamine synthase was unsuccessful and the structure of yersinopine remains presumptive. *Y. pestis* opine dehydrogenase enriched with selenomethionine crystallized and single wavelength anomalous dispersion (SAD) X-ray diffraction data were collected allowing structure solution. The *Y. pestis* opine dehydrogenase structure was then used as a molecular replacement model in the structure solution for data sets collected from *S. aureus* and *P. aeruginosa* opine dehydrogenase crystals, expanding the number of determined opine dehydrogenase structures in the Protein Data Bank from two to five. A steady-state comparison of these three opine dehydrogenases revealed differences in substrate specificity. *S. aureus* and *Y. pestis* use pyruvate and NADPH while *P. aeruginosa* uses α-ketoglutarate and can use either NADH or NADPH. These analyses are described in chapter three.

Opine dehydrogenases perform condensation and reduction steps on the prochiral α-carbon of an α-ketoacid and specifically generate one stereocenter, (R) or (S), depending on their structural family. Opine metallophore-producing opine dehydrogenases are in the family that produce (R) stereocenters. We demonstrated that the *S. aureus* and *P. aeruginosa* opine dehydrogenase reactions are reversible and catalyze the reverse reaction only with the (R) diastereomer of staphylopine and pseudopaline respectively. No catalysis was seen in the

presence of the (S) diastereomer. In the previously published opine dehydrogenase structures, $NADP^+$ was bound with at least partial electron density, but a structure with bound substrates had not been solved. Structures of *P. aeruginosa* opine dehydrogenase were solved with both the (R) and (S) diastereomers of pseudopaline. Interestingly, while complete density of (S)-pseudopaline was visualized at 1.64 Å, (R)-pseudopaline was progressively hydrolyzed by the cystal demonstrating reverse catalysis in the X-ray structures. Transient state kinetic analysis of *S. aureus* opine dehydrogenase revealed that product release was the rate-limiting step of catalysis. These data are described in chapter four.

Opine metallophores represent a new class of bacterial metallophore produced by a nicotianamine synthase and an opine dehydrogenase. Nicotianamine synthases remain poorly characterized and future work on the structure and kinetics of this enzyme family will be necessary to provide a mechanistic understanding of function. Our analysis of opine dehydrogenases from *S. aureus* and *P. aeruginosa* provides an excellent structure/function analysis and is the foundation for advanced kinetic analyses. These data, along with the expanding analysis of the functional roles of opine metallophore pathways *in vivo*, are leading toward a global model describing the function of these systems.

Acknowledgements

Thank you to the Department of Molecular Biosciences, to my fellow graduate students to my professors and to my committee members. My interactions within the department were consistently supportive making KU an enjoyable environment for pursing graduate work. Thank you to Annemarie Chilton and Kathy Meneely for their friendship as well as their instruction in fundamental biochemical techniques including protein purification, crystallization and assay development. They were always available to discuss problems and hypotheses which enriched my learning experience. I would like to thank two undergraduate students who worked on the opine metallophore project. Nick Martinez performed the early work on the purification of the *Y. pestis* nicotianamine synthase, a difficult task through which he demonstrated his perseverance. Cara Davis was able to purify the *Y. pestis* opine dehydrogenase, an enzyme that crystallized readily, and her work with the selenomethionine-enriched version of this protein ultimately led to our first opine dehydrogenase structure. Cara is pursuing her own graduate career and I am pleased to mark her among my colleagues. I am grateful to Catie Shelton for her quiet wisdom, for recommending the AHA fellowship opportunity to me and for sharing her experiences while pursuing a faculty position. Thanks to Trey Ronnebaum for kind encouragement and support, valuable scientific discussions and for the opportunity to collaborate on two projects ultimately leading to two publications. Thanks to Nikola Kenjic, who loves to talk science. Our discussions were of great benefit to me. Nikola's work ethic and perseverance set a great example of the skills necessary for those seeking success in scientific research.

Collaborators contributed in essential ways to this work. Thank you to Dr. Graham Moran for providing instruction in transient state kinetic methods and continuing to provide feedback throughout my transient state analysis. Thank you to Dr. Xiaoguang Lei whose students Jian Zhang and Sanshan Wang generated substrate and product compounds allowing new structural and kinetic studies. Thanks to the Dr. T. Christopher Gamblin lab for the generous use of

equipment. Thank you to the staff of the Stanford Synchrotron Radiation Lightsource who always demonstrated a willingness to go above an beyond in the support of our diffraction studies.

Finally, a huge thank you Dr. Audrey Lamb. In joining this laboratory I became and X-ray crystallographer and enzymologist, two fields in which I possessed prior interest, but limited knowledge. I am grateful for your mentorship, for your instruction in writing and publishing, in crystallography techniques, for pushing me to pursue fellowship and award opportunities, for guiding my future career and for your friendship. I am a proud Lamb protégé.

Table of Contents

List of Figures

List of Tables

Chapter 1

Introduction

Metallophores are small molecule metal chelators that are secreted by bacterial, fungal and plant cells into the external environment where they are coordinated by metal before returning to cell through dedicated transporters and releasing their metal cargo into the periplasm or cytosol. Metals such as iron, zinc and cobalt are essential to the function of metalloproteins and metalloenzymes, and thus survival, making metal acquisition a required function. Bacterial pathogens employ metallophores within the human body allowing them to compete for available metal and, in some species, cause infection.

Numerous metallophore biosynthetic pathways have been elucidated and characterized, but in this work a novel metallophore class, the opine metallophore, is identified and described. Opine metallophores are produced by two enzymes, a nicotianamine synthase and an opine dehydrogenase. This introductory chapter discusses the importance of metal acquisition, provides a summary of prior knowledge of nicotianamine synthase and opine dehydrogenase enzymes, and discusses the widespread occurrence of opine metallophore pathways in bacterial species. Subsequent chapters address the experimental work completed to characterize the opine metallophore pseudopaline, to determine X-ray crystal structures for several opine dehydrogenases, and to analyze the kinetic mechanisms of nicotianamine synthase and opine dehydrogenase enzymes.

Metal Uses and Acquisition

All bacteria require a variety of transition metals for growth because these metals are essential to numerous cellular processes. Notably, transition metals are incorporated into proteins to provide structural integrity, such as the role of Zn(II) in the coordination of two cysteines and two histidines to stabilize the $\beta\beta\alpha$ fold of C_2H_2 zinc finger domains that typically serve to bind DNA, RNA or other protein domains[1]. Metals also act as cofactors. Classic examples include the

transport of oxygen by hemoglobin using iron centers within heme porphyrin rings and the transfer of electrons by iron heme within a variety of cytochrome proteins. Metal cofactors are also used to catalyze the unique chemical transformations performed by metalloenzymes – enzymes that require one or metals for function. Examples are numerous, but we summarize a few here to emphasize both the vital role of metalloenzymes and the diversity of transition metals they utilize.

It is estimated that as many as one half of all proteins require metal for function[2, 3]. Iron is the most abundant transition metal in cells and is widely used by metalloproteins. An example of a well conserved metalloenzyme is Class I ribonucleotide reductases which contain a dinuclear iron center that generates a tyrosyl radical species used to initiate the reductase activity in the conversion of ribonucleotides to deoxyribonucleotides, a key step in DNA synthesis[4]. Nitrogenases represent a second important iron-utilizing metalloenzyme. They catalyze the reduction of N_2 to NH_3 by nitrogen-fixing organisms, a reaction central to the nitrogen cycle and vital to life on Earth. Electrons for this reduction are transferred in series from a reducing source to a 4Fe-4S cluster, an 8Fe-7S cluster and finally to an iron cofactor containing molybdenum, vanadium or iron alone[5, 6]. Zinc is the second most abundant cellular transition metal. While not redox active, zinc catalyzes acid/base chemistry in many enzymes. Examples include the promotion of proton abstraction by histidine in the conversion of ethanol to acetaldehyde by alcohol dehydrogenase[7], and the activation of water as a nucleophile in the production of bicarbonate from CO_2 and H_2O by carbonic anhydrase[8]. Human superoxide dismutase, which protects the cell against free radical damage, uses Cu(I) and Cu(II) redox states of copper to bind superoxide performing a homolytic cleavage of a copper-oxygen bond releasing molecular oxygen and hydrogen peroxide[9]. Nickel and cobalt are not used as widely by enzymes, but are still essential to many organisms. Urease converts urea to CO_2 and NH_3 and uses two nickel atoms in the binding of urea and activation of water as a nucleophile[10]. In *Helicobacter pylori*, the ammonia produced by urease raises the pH of the stomach lining allowing growth[11], and urea-derived NH_3 provides a nitrogen source to pathogens infecting the human urinary tract[12]. Cobalt

forms the metal center of cobalamin, the vitamin B_{12}-derived cofactor capable of forming an unusual cobalt-carbon adduct that plays a central role in the conversion of homocysteine to methionine by methionine synthase[13].

The formation of metalloproteins within the cell requires a homeostatic supply of necessary metals, including Fe, Zn, Cu, Co and Ni, from the nutrient pool in the surrounding environment. Yet metal availability is not always assured. For example, biologically available iron exists in two oxidation states, Fe(II) and Fe(III). While Fe(II) is readily soluble, it oxidizes to Fe(III) in aerobic environments and at neutral pH forming ferric oxyhydroxide precipitates[14]. The concentration of freely soluble Fe(III) is estimated to be only 10^{-18} M in water[15] and thus cellular access to the second most abundant metal in the Earth's crust is severely limited. The human body prevents the loss of iron to insoluble ferric oxyhydroxides by sequestering it. Transferrin and lactoferrin proteins perform this task by binding Fe(III) in the extracellular space. This form of sequestration serves a dual purpose as it also creates a severe metal limitation for pathogenic bacteria seeking to colonize human tissues and sets up a competition between bacteria and the human host for available metal.

Despite potentially limited available quantities, cells exhibit a remarkable capacity to concentrate metal intracellularly. The bacterial pathogen *Pseudomonas aeruginosa*, when grown in LB media, is able to concentrate 4 μM iron present in the media to 4.2 mM in the cytosol. Similarly, zinc is concentrated from 15 μM to 2.5 mM and copper from 152 nM to 302 μM[16]. Given the necessity of a variety of transition metals, and their scarcity in many environments, it is not surprising to find that organisms employ a variety of mechanisms to acquire, retain and traffic metal. *Pseudomonas aeruginosa* serves as an excellent case study of many of the metal acquisition strategies that have evolved[17]. *P. aeruginosa* encodes many transport systems. In anaerobic or microaerobic environments such as biofilms Fe(II) remains reduced and soluble and is transported across the inner membrane by the FeoABC transport system[18]. Iron containing heme molecules are an abundant source of iron. The Phu pathway, with a TonB-dependent

surface receptor and inner membrane ABC transport system[19] is able to import heme where it is shuttled into the cytoplasm[20] to be degraded by HemO, a heme oxygenase, that releases Fe(II)[21]. Several zinc transport systems are active during zinc limitation including the ZnuABCD pathway and an operon containing genes Pa4834-4837, to be described in detail below[22]. Transport systems have also been described for copper[23, 24] and molybdenum[25].

Metallophores

In a more proactive approach, cells biosynthesize and secrete small molecule metallophores, with oxygen, nitrogen or sulfur-containing ligands that form high affinity metal chelates (we use the term metallophore, rather than siderophore which means iron carrier, as many siderophores have also been shown to chelate other essential metals making metallophore the preferred general terminology). In complex with metal, metallophores are recognized by receptors and taken back up into the cell to deliver their metal cargo for use in metabolism. It has been frequently observed that single species encode multiple such metallophore biosynthetic pathways, themselves a wealth of natural product diversity that have inspired considerable investigation[26]. The apparent cellular need for multiple metallophores suggests that differences in the affinity or specificity of the metallophore for metal, or regulatory control of different operons, allows cells to adapt to varied environments by adjusting their acquisition strategy to match metal availability. The affinity and specificity of a metallophore is dependent both on the structure of the metallophore (geometry and ligands) and the nature of the metal (ionic radius and ionic charge). Hard soft acid base (HSAB) theory[27] aids in the prediction of affinity between metals species and potential ligands. For example, Fe(III) has a higher ionic charge to ionic radius ratio (z/IR) than Ni(II) or Zn(II) and will coordinate more favorably with hard donating ligands such as carboxylate oxygens forming bonds that are closer to the ionic limit[28]. This does not necessarily confer specificity because a non-target metal with a higher charge to radius ratio would bind competitively. Likewise, lower affinity metals that exist at a higher concentration in the local environment may also compete for ligand. Transition metals that are softer Lewis acids, such as

Cu(I), Co(II), Ni(II) or Zn(II) coordinate ligands through interactions that are more covalent than ionic. Reduced donor ligands such as nitrogen found in secondary amines, imidazole or thiolate groups coordinate soft Lewis acid transition metals with greater affinity. Thus, metallophore diversity may in part be explained by the advantage of an organism able to produce metallophores with structural differences that confer varied metal affinity and specificity. In the following section we present a selection of characterized metallophores from representative pathways to illustrate this structural and functional diversity.

Oxygen-containing ligands, such as hydroxyls, carboxylates, hydroxamates, phenolates and catecholates form the core functional groups for a variety of metallophores (**Figure 1-1** shows the metallophores described below). Citrate, a central metabolite possessing three carboxylate and one hydroxyl functional group, is able to solubilize ferric hydroxides. Ferric citrate is transported by *Escherichia coli,*[29] and *Bradyrhizobium japonicum* produces citrate as an exogenous metallophore under metal limitation[30]. Carboxylate groups are common to many metallophores such as staphyloferrin B (which incorporates a citrate precursor)[31] from *S. aureus*, and mugineic acid[32], a phytometallophore. Mugineic acid contains carboxylate, hydroxyl and amine ligand groups and while it is typically referred to as a siderophore, mugineic acid derivatives are also responsible for the mobilization of copper, zinc and manganese from soil, although the uptake of these metals is much slower than for iron chelates[33]. Pyoverdin, the virulence factor produced by *P. aeruginosa* during infection, uses both hydroxamate and catecholate chelating groups containing oxygen ligand atoms and is one of the most highly studied metallophores; research that has revealed diverse functions. Fe(III) coordinates pyoverdin with a pFe = 27[34] (pMetal is the negative $\log_{10}$ of the free metal concentration when total metal concentration is 10^{-6} M and total ligand concentration is 10^{-5} M) allowing it to compete with human transferrin for iron and making it essential to pathogenesis[35]. Pyochelin incorporates phenolate, thiazoline and thiazolidine rings into its structure altering metal binding affinity. Fe(III) coordinates pyochelin with much lower affinity (pFe = 16) than pyoverdin, but pyochelin has similar affinity for Zn(II) (pZn =

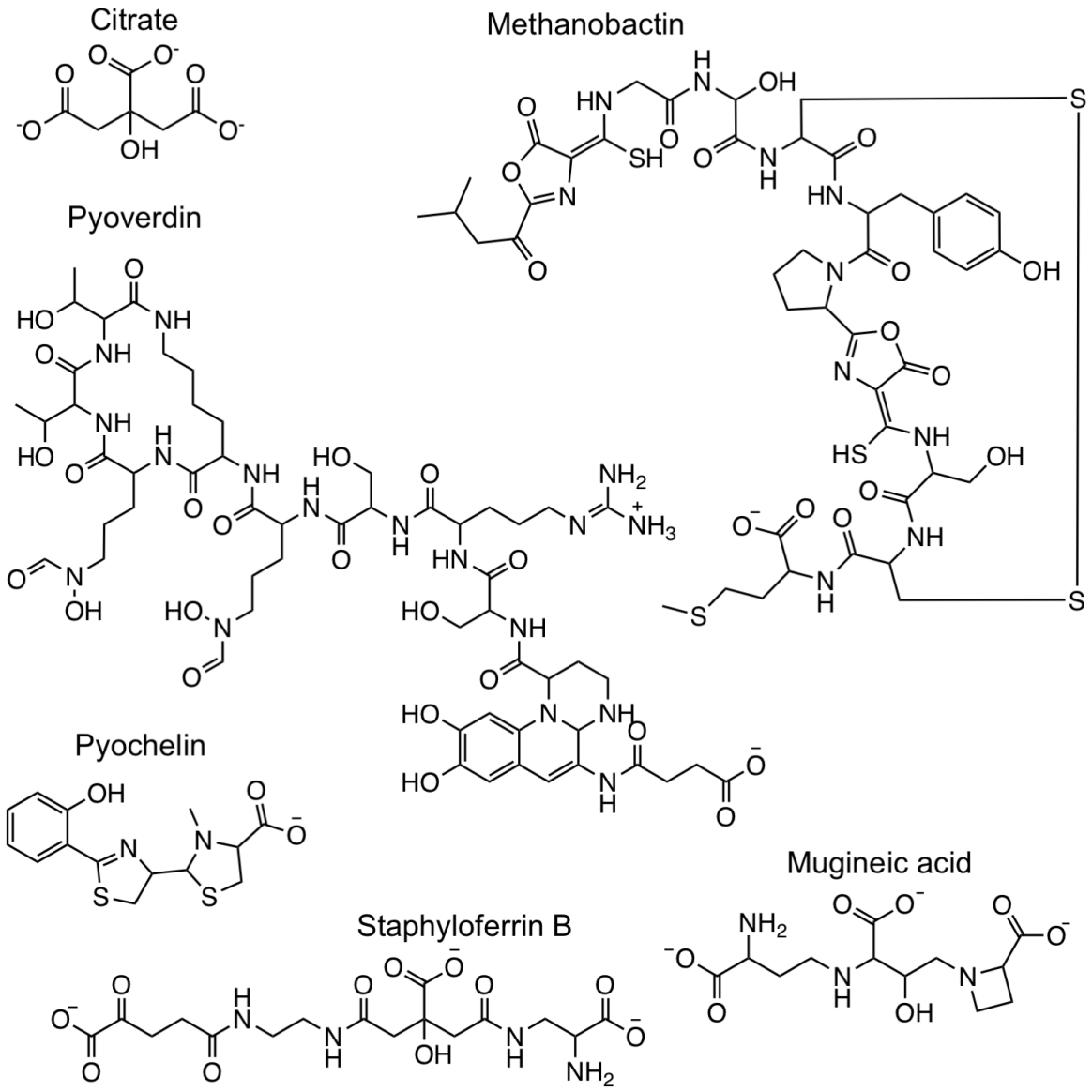

Figure 1-1. Example metallophores. Citrate is produced as a metallophore by *Bradyrhizobium japonicum*. Methanobactin as produced by *Methylosinus trichosporium* OB3b. Pyoverdin and pyochelin as produced by *Pseudomonas aeruginosa*. Staphyloferrin B as produced by *Staphylococcus aureus*. Mugineic acid as produced from a nicotianamine precursor by plants such as *Hordeum vulgare* (barley).

11.8) and Cu(II) (pCu = 14.9)[36]. Interestingly, *P. aeruginosa* growing in the presence of elevated copper increases expression of pyoverdin which uptakes Cu(II) at a much lower rate than iron[37], but decreases expression of pyochelin which has a Cu(II) affinity similar to that of Fe(III)[38]. This may be a means of limiting copper toxicity due to Fenton chemistry[39] and points to the nuanced control of metal homeostasis by metallophore pathways[38]. Methanobactins are metallophores produced by methanotrophic bacteria that require high concentrations of copper for incorporation into methane monooxygenases[40]. They serve as an example of the relationship between metallophore structure and metal affinity. They chelate Cu(II) using tetrahedral geometry formed from two thiols and two nitrogen heterocycles (shown in **Figure 1-1** as oxozolone rings as found in *Methylosinus trichosporium* OB3b methanobactin, but other variations exist in different strains) and are taken up into the cell through a TonB-dependent transport system [41]. The above examples illustrate the value of maintaining pathways for multiple types of metallophores within an organism's genome. These variant metallophores allow the maintenance of cellular homeostasis for multiple transition metals under changing environmental conditions.

The Identification of Opine Metallophore Pathways

Given that *Pseudomonas aeruginosa* and *Staphylococcus aureus* each produce two well characterized metallophores, pyoverdin and pyochelin (*P. aeruginosa*) and staphyloferrin A and B (*S. aureus*), it was initially surprising when Gi *et. al.*, in 2015, hypothesized that a novel nicotianamine-like metallophore was being produced by a four-gene operon in *P. aeruginosa* (**Figure 1-2**). *P. aeruginosa* is a gram-negative commensal, opportunistic pathogen that is increasingly resistant to available antibiotics. It is a leading cause of nosocomial pneumonia and wound infections and causes chronic infection in most cystic fibrosis patients shortening life expectancy[42, 43]. The *P. aeruginosa* operon contains four genes given the locus tags *Pa4834-Pa4837*[44] and since renamed *zrmABCD*[45] or *cntIMLO*[46] by different researchers, as described below.

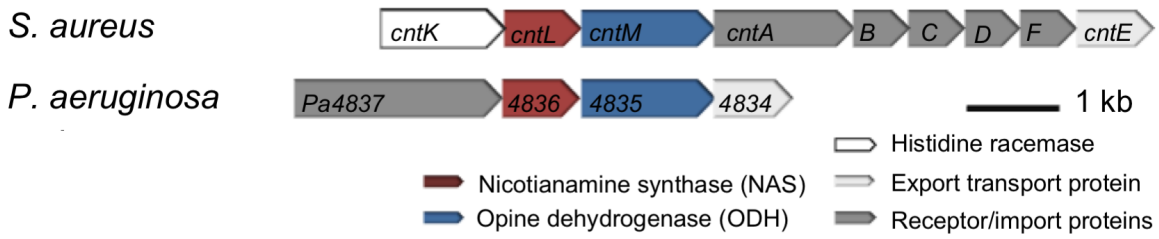

Figure 1-2. Homologous opine metallophore operons from three bacterial pathogens.

In 2015, Gi *et. al.* published a study[47] in which they collected airway mucus secretions (AMS) from cultured normal human tracheal epithelial cells and used them as a culture medium for a series of bacterial pathogens including *S. aureus*, *Salmonella enterica* and *P. aeruginosa* (PAO1). Only *P. aeruginosa* retained viability after 16 hours of incubation in AMS. A microarray analysis of *P. aeruginosa* cultured in AMS demonstrated the upregulation of numerous metal acquisition genes, including those involved in pyoverdin and pyochelin biosynthesis. The *Pa4834-37* operon showed an 8-fold increase in expression. Gi *et. al.* then demonstrated that Δ*Pa4834* mutants lost their viability in AMS while pyoverdine and pyochelin mutants remained viable within error of controls. Gi *et. al.* hypothesized that *Pa4836* encoded a nicotianamine synthase enzyme based on bioinformatic analysis and proposed that the operon was producing a nicotianamine-like metallophore. They demonstrated that viability for Δ*Pa4834* mutants in AMS could be recovered by supplementation with nicotianamine and used ICP-MS to demonstrate an approximately 20-fold increase in intracellular iron concentration for PAO1 in comparison to Δ*Pa4834*. Finally, Gi *et. al.* observed a 100-fold attenuation of growth for Δ*Pa4834* in a murine acute airway infection model and a 1000-fold attenuation in a murine burn wound infection model (n=3 for both studies, comparisons were with PAO1). This work offered the first hypothesis for the function of the *Pa4834-37* operon and demonstrated a direct role in two infectious disease models.

Early bioinformatic analysis of the *P. aeruginosa* genome predicted that *Pa4834* was an inner membrane transport protein of the EamA efflux family and that *Pa4837* was a TonB-dependent receptor located in the outer membrane[48]. Gene expression profiles under disease conditions and in metal limited environments strongly suggested an association with metal uptake during infection. mRNA expression of *Pa4835* and *Pa4836* in isolates from three burn wound patients showed an 8-fold increase in expression levels, and isolates from sputum samples from four cystic fibrosis patients showed a 9-fold increase, both in comparison to planktonic growth[49, 50]. In a murine pneumonia model, transcriptomic analysis showed an 8-fold and 18-fold increase

in *Pa4835* and *Pa4836* expression, respectively, in comparison to *in vitro* controls[51]. The *Pa4834-4837* operon is clearly upregulated during infection making an understanding of its functional role pertinent.

As work on *P. aeruginosa* was accumulating, different research groups were studying a similar operon in *S. aureus*; work that converged in 2016 and 2017. *S. aureus* is a gram-positive cocci that acts as a commensal, opportunistic pathogen colonizing the skin and respiratory tracts of up to 30% of U.S. adults[52]. *S. aureus* is the leading cause of endocarditis, an infection of the heart valve leaflets, and of bacteremia, an infection of the blood. These conditions have mortality rates of up to 66% for endocarditis and up to 50% for bacteremia[53]. Methicillin resistant *S. aureus* alone causes infections leading to over 11,000 deaths per year in the United States[54]. This represents nearly half of all deaths due to antibiotic resistant infections.

S. aureus employs urease, a nickel dependent enzyme, as a virulence factor in urinary tract infections[12]. *Hiron et. al.*, in 2010, identified four operons potentially associated with nickel uptake in *S. aureus*. The operons named *opp1*, *opp2*, *opp4* and *opp5a* (oligopeptide permease) had gene homology with the *nikABCDE* nickel permease system in *E. coli*[55]. A subsequent study found that the *opp1* operon was responsible for nickel and cobalt uptake under metal limiting conditions with expression that was responsive to zinc deficiency[56]. Additionally, cobalt and zinc present in the media was found to compete with nickel uptake suggesting either direct competition in the uptake pathway or through a regulatory control. They renamed the operon *cntABCDF* (**Figure 1-2**). Purified CntA, incubated with *S. aureus* culture supernatants grown under conditions of nickel limitation, was shown by mass spectroscopy to bind nickel in complex with a molecule that had a mass of 327 Da[57]. The authors suggested that this 327 Da molecule could be a metallophore biosynthesized by *S. aureus*.

Opine Metallophore Biosynthesis

Identification of the metallophore associated with the *cntABCDF* operon in *S. aureus* came in 2016 when Ghssein *et. al.* hypothesized that it was being produced by three genes, immediately upstream of *cntABCDF*, that they named *cntKLM*[58] (**Figure 1-2**). The entire *cntKLMABCDF* operon was overexpressed in *E. coli* and ICP-MS and ESI-MS of the *E. coli* supernatants were used to confirm the presence of chelation complexes in which the non-metal portion had a mass of 327.06 Da. MS/MS fragmentation led to the identification of a new metallophore they named staphylopine. Using WT *S. aureus* as well as cntL and cntA-F mutants they demonstrated a role for staphylopine in the uptake, not only of nickel, but of additional transition metals including Fe, Zn and Co. This work also established that two core enzymes, a nicotianamine synthase (SaNAS, CntL) and an opine dehydrogenase (SaODH, CntM), biosynthesize staphylopine in *S. aureus* (a third enzyme, CntK, which is a histidine racemase, is required to produce D-histidine as a substrate) (**Figure 1-3A**). Song *et. al.* were able to crystallize the CntA receptor with staphylopine in complex with Zn(II), Ni(II) and Co(II) providing structural evidence for the re-uptake of staphylopine in complex with metal. All three metals coordinated staphylopine with octahedral geometry[59] (**Figure 1-4**).

A two-enzyme biosynthesis, with no direct requirement for ATP, is quite modest in comparison to the many established, often complicated, metallophore biosynthetic pathways. Nicotianamine synthases use *S*-adenosyl-L-methionine (SAM) as a substrate, performing an aminobutyrate transfer from the methionine of SAM, and forming a secondary amine with either an amino acid or a second aminobutyrate[60, 61]. In grassy plants, this reaction is known to be processive resulting in three aminobutyrates linked in series forming the siderophore nicotianamine[61]. Opine dehydrogenases form secondary amines between an amino acid substrate and an α-keto acid substrate. Opines have diverse functional roles. *Agrobacterium tumefaciens* infects plants leading to tumor formation. A key virulence factor for tumorigenesis is opine dehydrogenase expression that results in the incorporation of plant amino acids and a-keto

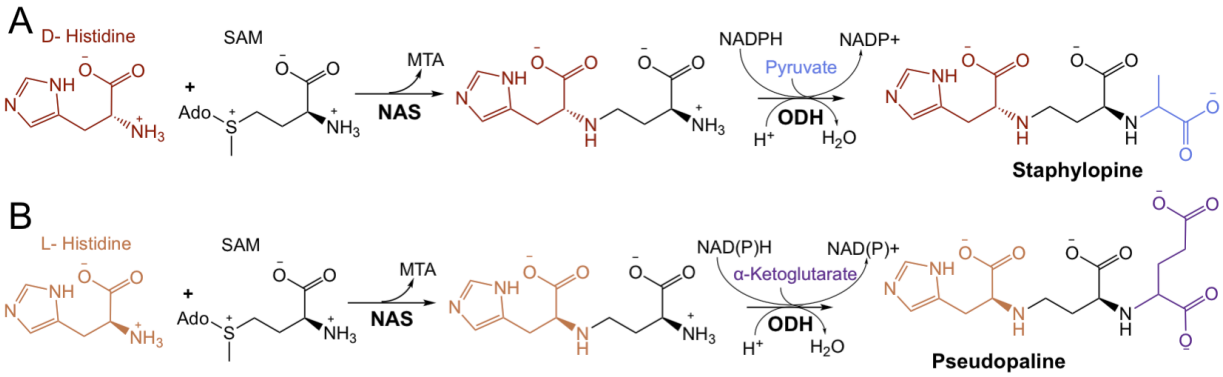

Figure 1-3. Opine metallophore biosynthesis. A. Staphylopine biosynthesis in *S. aureus*. D-Histidine is made by CntK, a histidine racemase. CntL, a nicotianamine synthase (NAS) uses D-Histidine and S-adenosyl-L-methionine (SAM) to produce a nicotianamine-like product, D-Histidine-nicotianamine (D-HisNA). CntM, an opine dehydrogenase (ODH) uses D-HisNA and pyruvate as substrates with NADPH as a co-substrate producing the metallophore staphylopine. **B.** Pseudopaline biosynthesis in *P. aeruginosa*. L-Histidine is the amino acid substrate for the NAS and α-ketoglutarate is the α-keto acid substrate for the ODH. The *P. aeruginosa* ODH is nonspecific, using NADH or NADPH.

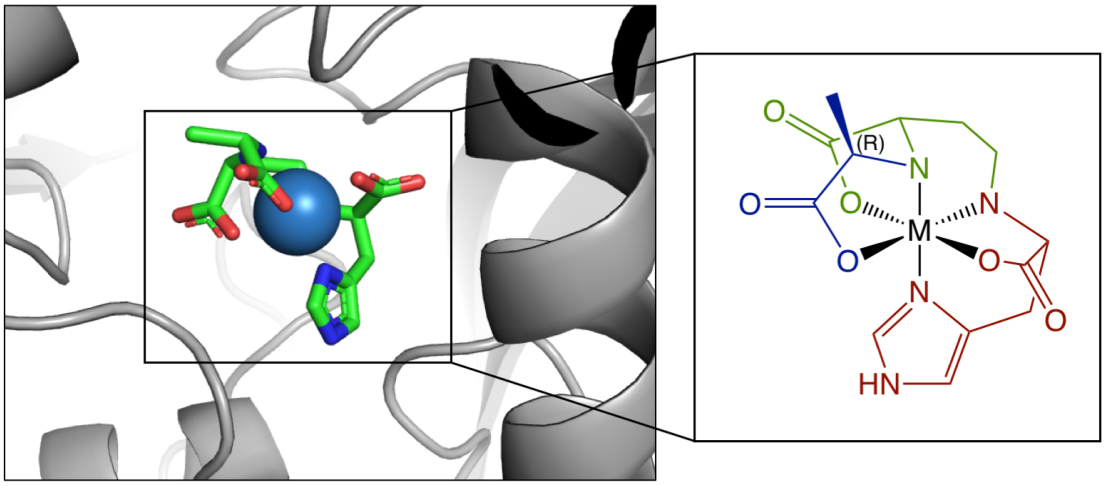

Figure 1-4. Staphylopine bound to CntA (PDB:5HYG). Co-crystal structure of staphylopine (green carbons) in complex with zinc (blue sphere) and bound to the CntA receptor (left panel). Coordination geometry is octahedral based on the crystal structure (right panel) (blue – pyruvate moiety, green – aminobutyrate moiety, red – D-histidine moiety).

acids into opine that only the bacterium can metabolize. In molluscs and cephalopod muscle tissue opine dehydrogenases replace lactate dehydrogenase allowing the continuation of glycolysis through the regeneration of NAD^+ during anaerobiosis[62]. While nicotianamine synthases and opine dehydrogenases had not previously been found in a concerted pathway their respective chemistries are compatible, with the NAS generating a modified amino acid-nicotianamine product accepted as a substrate by the ODH.

S. aureus NAS (SaNAS) and ODH (SaODH) have significant homology with Pa4835 (PaODH) and Pa4836 (PaNAS). Pa4835 and Pa4836 were first proposed by Gi. *et. al.* to be producing a nicotianamine-like metallophore. To examine this possibility in *P. aeruginosa*, an assay was developed combining the PaNAS and PaODH with SAM and NADPH and screening different combinations of amino acid and α-keto acid substrates[63]. This work is described in detail in chapter two. Enzyme turnover was measured as a loss of absorbance at 340 nm as NADPH is oxidized by PaODH during the reaction. Screening of 126 amino acid and α-keto acid substrate combinations revealed catalysis with only one pair, L-histidine and α-ketoglutarate. Mass spectrometry analysis confirmed that the *P. aeruginosa* NAS and ODH use one aminobutyrate moiety derived from SAM, one L-histidine and one α-ketoglutarate in the production of a metallophore compound named pseudopaline[63] (**Figure 1-3B**). This demonstrates both the specificity of the enzymes for these substrates and the inability of the *P. aeruginosa* NAS to form a true nicotianamine product using a processive reaction with SAM alone.

Reconstituting both the *P. aeruginosa* and *S. aureus* pathways with purified enzymes revealed several differences in substrate selection[63]. The NAS enzymes showed opposite stereo-selectivity. *S. aureus* specifically incorporated D-histidine and encodes a racemase for production of the D-amino acid, whereas *P. aeruginosa* used only L-histidine. The ODHs also showed differential substrate recognition. *P. aeruginosa* incorporates α-ketoglutarate and shows no evidence of turnover with either of the smaller, metabolically available α-keto acids pyruvate or

oxaloacetate, whereas *S. aureus* used pyruvate and turned over at a reduced rate with oxaloacetate, but not at all with α-ketoglutarate[63]. These subtle differences in chemistry result in an additional available carboxylate group for metal coordination by pseudopaline and opposite stereochemistry for the histidine moiety leading to differences in stereochemistry and, potentially, differential receptor recognition.

Additional functional studies are beginning to appear in the literature. Mastropasqua *et. al.* demonstrated that the pseudopaline operon in *P. aeruginosa* PA14 is transcriptionally activated by Zn limitation, is directly regulated by the zinc-uptake regulator ZUR and that inactivation of ZrmA (TonB-dependent receptor, Pa4837) or ZrmB (PaNAS) and ZnuABC (inner membrane ABC transport proteins for zinc uptake) severely restricted growth in zinc-limited media. They constructed a ZrmA/ZnuA double mutant and found that the mutant was unable to cause acute lung infections in mice in comparison to the wild-type PA14[45]. L'Hospice *et. al.* also confirmed that pseudopaline expression is responsive to Zn limitation. Growing *P. aeruginosa* in minimal succinate media led to the biosynthesis of pseudopaline which was detected using ICP-MS and ESI-MS confirming the *in vivo* production of pseudopaline with the composition described above[46]. L'Hospice *et. al.* named the operon *cntIMLO* due to its additional role in nickel uptake and homology with staphylopine biosynthesis, while the *zrmABCD* (zinc regulated metallophore) gene name given by Mastropasqua *et. al*. is based on the role in zinc uptake and regulation by zinc availability. Staphylopine has also been associated with zinc acquisition by Grim *et. al.*[64]

Two studies have examined the promoter region for the staphylopine and pseudopaline operons. Fojcik *et. al.* found that the *cntKLMABCDF* operon contains two promoters. The first precedes *cntKLM* and the second, an internal promoter, precedes *cntABCDF*. The *cntKLM* promoter contains both a FUR box (ferric uptake regulator) and a ZUR box (zinc uptake regulator). The internal promoter contains a FUR and ZUR box that overlap allowing binding of FUR or ZUR, but not both repressors. Functional analysis revealed that *cntKLM* (the biosynthetic genes for staphylopine production) are expressed under both iron and zinc limitation and are thus tightly

controlled, while the cooperative regulation of *cntABCDF* led to weaker repression[65]. This may allow the uptake system to be expressed for the transport of xenosiderophores while repressing the more metabolically expensive biosynthesis under less severe metal limitation. Hermansen *et. al.* analyzed the zrmABCD promoter from strains of *P. aeruginosa* derived from patients with chronic cystic fibrosis and found the frequent occurrence of variations leading to increased expression of pseudopaline, including in strains that had lost the ability to produce pyoverdin. This represents a potentially adaptive response to metal limitation during chronic infection[66].

These studies have demonstrated pseudopaline and staphylopine-dependent uptake of a spectrum of metals *in vivo* including Fe, Zn, Co and Ni, justifying the use of the broad term metallophore. The identification of pseudopaline and staphylopine illuminates two homologous enzyme pathways, each performing variations of similar chemistries and resulting in novel metallophore products. These systems play a significant role in infection, but their interplay with known metallophore systems such as pyoverdin (*P. aeruginosa*) and staphyloferrin (*S. aureus*) remains uncertain raising new considerations for future model studies. The biosynthesis of opine metallophores does not use non-ribosomal peptide synthases (NRPS), polyketide synthases (PKS) or ribosomally synthesized and post-translationally modified peptides (RiPPs), as is typical for metallophore biosynthesis. Rather, opine metallophores are biosynthesized by a new enzyme combination, a nicotianamine synthase and an opine dehydrogenase. The unique specificity and stereoselectivity of these enzymes is revealed by the subtle differences in pseudopaline and staphylopine structure. As homologous operons have been identified in a surprisingly diverse group of species, including the pathogens *Yersinia pestis*, *Serratia marcescans*, and *Streptococcus pneumoniae*, it is likely further diversity will be revealed in this emerging class of metallophores. In the following section we provide a review of the existing literature on the nicotianamine synthase and opine dehydrogenase enzyme classes.

Nicotianamine Synthase

Nicotianamine synthases are SAM-dependent aminoalkyltransferases known to produce the metal carrier nicotianamine found within plants. Nicotianamine is the precursor to a larger family of metallophores known as mugineic acids (MA). While nicotianamine can be isolated from all plants, MA and MA derivatives are found only in graminaceous or grassy plants where they are secreted from root tissue into the surrounding soil to capture iron and other transition metals including Mn, Cu and Zn[33]. The mugineic acid family of molecules are the only known phytosiderophores (siderophores produced by plants) (**Figure 1-5, 1-6A**).

The incorporation of the aminobutyrate portion of L-methionine into mugineic acid and 2'-deoxymugineic acid was determined by feeding studies. L-[1-C^{13}]-methionine administered to Barley (*Hordeum vulgare*) roots following hydroponic growth in iron deficient conditions resulted in C^{13} incorporated at positions C1, C4' and C4'' of mugineic acid, suggesting that each aminobutyrate moiety of mugineic acid is derived from one methionine (**Figure 1-5**). Additional isotope feeding studies with barley root extracts were used to confirm the *in vitro* biosynthesis of nicotianamine and mugineic acid via the addition of free L-[1-C^{14}]-methionine or [C^{14}]-SAM containing L-[1-C^{14}]-methionine[67]. Incorporation was significantly faster in the presence of [C^{14}]-SAM than for L-[1-C^{14}]-methionine. Additionally, L-[1-C^{14}]-methionine required the addition of ATP. These data suggest that SAM is the direct precursor of nicotianamine. Further studies in the presence and absence of NADH and α-ketoglutarate revealed that mugineic acid derivatives are formed from nicotianamine though deamination followed by reduction to 2'-deoxymugineic acid[61, 68] (**Figure 1-5**). A small molecule crystal structure of mugineic acid was solved in 1981 demonstrating the formation of an azetidine ring (4-membered heterocycle with 3 carbons and 1 nitrogen) from the first aminobutyrate moiety[32]. While numerous investigators contributed to the early elucidation of mugineic acid biosynthesis, the kinetic mechanisms employed by these enzymes remain unexamined.

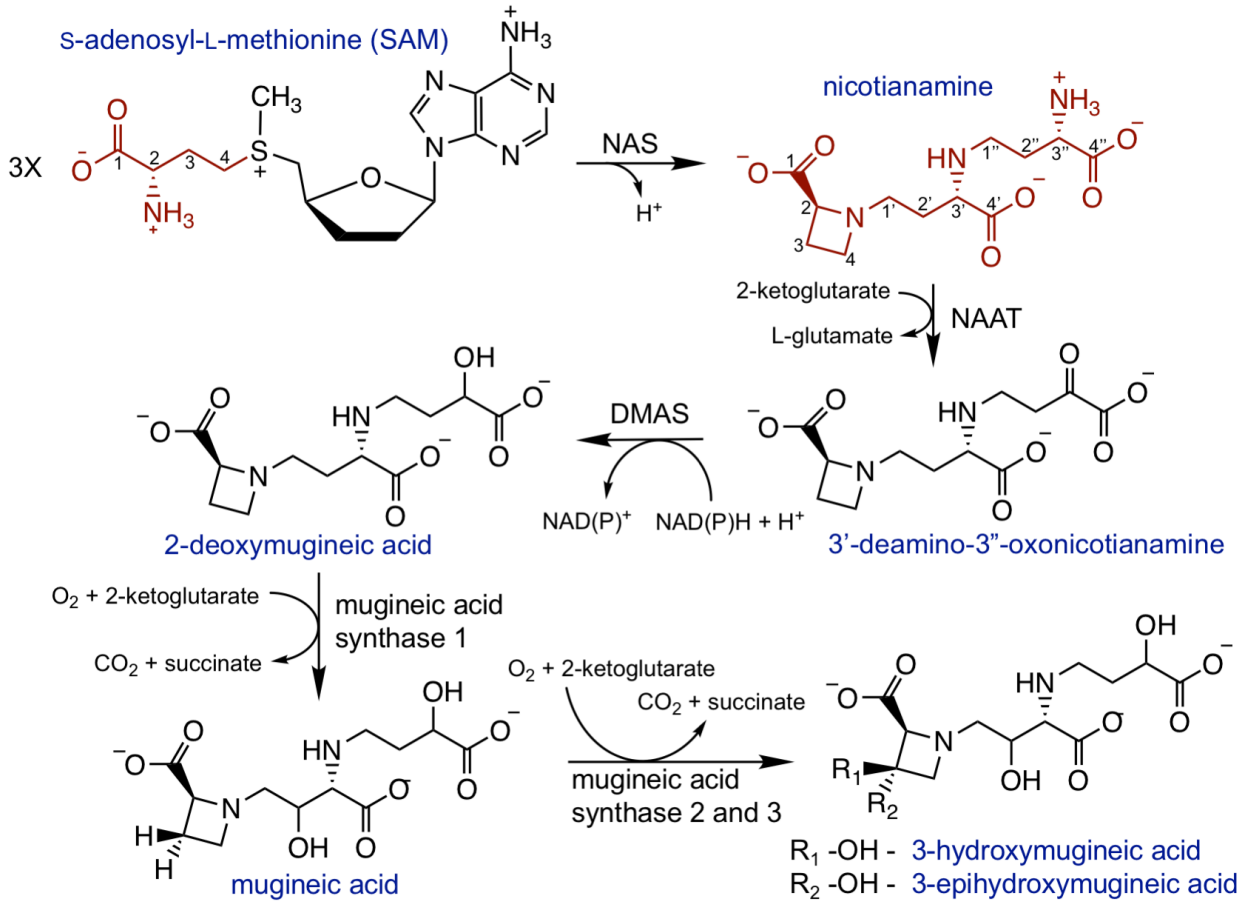

Figure 1-5. Phytosiderophore biosynthesis. The aminobutyrate moiety (red) of S-adenosyl-L-methionine forms the backbone of phytosiderophores. Nicotianamine is used within the plant for metal transport and is a precursor for secreted mugineic acid metallophores. NAS – nicotianamine synthase. NAAT – nicotianamine aminotransferase. DMAS – deoxymugineic acid synthase (3''-oxonicotianamine:NAD(P)H oxidoreductase). Mugineic acid synthases 1, 2 and 3 are also known as Isd1, Isd2 and Isd3. Pathway based on work completed in *Hordeum vulgare* and *Secale cereale*[70-72]

Bioinformatic analysis reveals that the SAM binding domain of nicotianamine synthases has sequence and structural homology with class I, Rossmann-like fold, SAM-dependent methyltransferases[69]. SAM-dependent aminoalkyltransferases conserve a residue in the SAM binding loop that may free the aminobutyrate for linkage with a second substrate rather than the more common methyl transfer reaction. This difference lies in the presence or absence of a negatively charged aspartate that bridges the methionine of SAM via a water molecule in class I SAM methyltransferases. In *Methanothermobacter thermautotrophicus* NAS and *P. aeruginosa* NAS this residue is a phenylalanine, while in *S. aureus* and *Y. pestis* NAS it is a leucine, preventing the establishment of a water bridge.

The only structure of a nicotianamine synthase is from *M. thermautotrophicus* (PDB: 3FPE, 3FPG, 3FPF, 3FPH). MtNAS produces a variant of nicotianamine, with the common name thermonicotianamine, in which L-glutamate is linked to two successive L-aminobutyrates from SAM (**Figure 1-6B**). The enzyme crystallized with thermonicotianamine in the active site even though no ligands were added during crystallization suggesting that the product co-purified. Additional structures, including those of an E81Q mutant (E81 is predicted act as a general base in concert with Y107), allowed the capture of SAM and L-glutamate in one structure, and methylthioadenosine (MTA) and thermonicotianamine in another (**Figure 1-7**). Taken together these structures led the authors to describe a processivity in which the initial substrate, L-glutamate, is activated as a nucleophile by proton transfer through a Y107/E81 relay performing a nucleophilic attack on C4 of an adjacently bound SAM[60]. The L-glutamate-aminobutyrate intermediate shifts deeper into the active site allowing MTA to be released and a second SAM to bind. The nucleophilic activation and attack is repeated with the primary amine of the L-glutamate-aminobutyrate acting as the second nucleophile. The reaction as followed by HPLC was very slow, described as a few turnovers in tens of minutes, leading the authors to suggest that an undetermined mechanism may speed the process *in vivo*. A subsequent structure co-crystallized

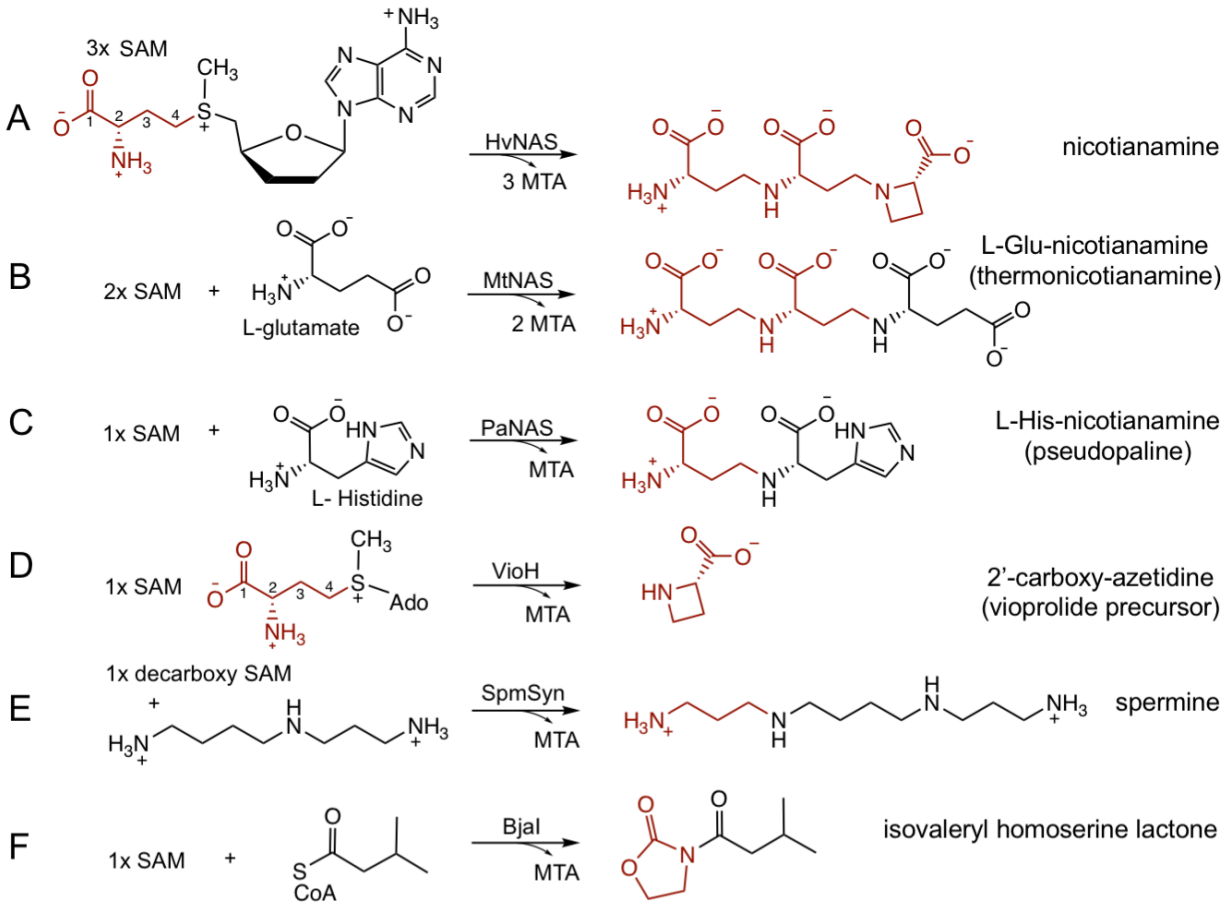

Figure 1-6. SAM-dependent aminoalkyltransferase reactions. A. *Hordeum vulgare* (Barley) nicotianamine synthase produces the metallophore nicotianamine. **B.** *Methanothermobacter thermautotrophicus* nicotianamine synthase produces the metallophore thermonicotianamine. **C.** *P. aeruginosa* nicotianamine synthase produces the precursor of pseudopaline. **D.** VioH from *Cysotobacter violaceus* of vioprolide biosynthesis produces azetidine-2-carboxylic acid. **E.** Spermidine synthase from *Homo sapiens* produces the polyamine spermine. **F.** BjaI, an acylhomoserine lactone synthase, from *Bradyrhizobium japonicum* produces an acylhomoserine lactone used in quorum sensing.

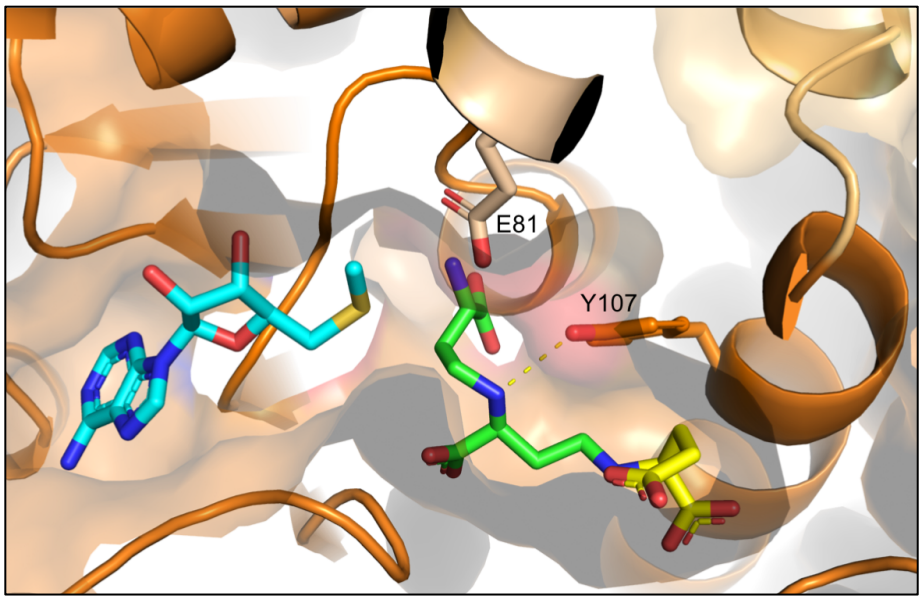

Figure 1-7. MtNAS active site (PDB:3fpf). Methylthioadenosine (MTA, cyan carbons) binds to a conserved Rossmann-like, SAM binding domain. Thermonicotianamine (SAM-derived aminobutyrates, green carbons; glutamate, yellow carbons) is bound in a long pocket that allows progression of the substrates deeper into the active site as the final product is formed. Y107 has been proposed as the catalytic base that deprotonates the primary amine of glutamate in the first step, and of aminobutyrate in the second step. As shown, Y107 is 3.0 Å from the secondary amine nitrogen of the terminal aminobutyrate.

with the L-glutamate-aminobutyrate (PDB: 3O31) provided further evidence for the shift of the substrate deeper into the active site pocket as catalysis proceeds[73].

Kawai *et. al.* proposed a chemical mechanism for the formation of nicotianamine in which NAS binds two SAM molecules concurrently[74]. While reasonable, this hypothesis preceded any available structural evidence and requires that the NAS bind two SAM molecules and precludes azetidine ring formation until the aminobutyrate elongation steps are complete. The MtNAS structural data suggests that L-glutamate binds first serving as the initial nucleophile and that only one SAM occupies the enzyme active site at a time. If plant NAS binds only one SAM, the azetidine ring would be formed in the first chemical step. The resulting azetidine-2-carboxylic acid product would remain in the active site and act as the nucleophile in a linkage with aminobutyrate from a second SAM. Precedent exists for this chemical step by the enzyme VioH in the vioprolide secondary natural product pathway.

VioH is a sequence homolog of class I SAM-dependent methyltransferases and is expressed in the vioprolide biosynthetic pathway. Yan *et. al.* demonstrated its role in cyclizing the aminobutyrate of SAM to form azetidine-2-carboxylic acid[75] (**Figure 1-6D**), a non-proteinogenic amino acid first identified in plants in the 1950's[76]. Azetidine-2-carboxylic acid is methylated by VioG and incorporated into a larger peptolide product ultimately leading to vioprolide. This is the first direct evidence, outside of plant NAS enzymes, of a class I SAM-dependent aminoalkyltransferase performing an azetidine ring formation. In the case of VioH, an azetidine ring is formed, but the enzyme is not processive. An understanding of the structural basis for the occurence of processivity and azetidine ring formation remains elusive.

Other structurally characterized SAM-dependent aminoalkyltransferases include human spermine synthase (PDB:3C6K) which forms the polyamine spermine from spermidine and one decarboxy-SAM (SAM in which the methionine residue is decarboxylated)(**Figure 1-6E**)[77, 78]. Spermine and related polyamines are involved in diverse gene expression and cell proliferation control mechanisms[79]. The SAM binding domain of human spermine synthase is conserved with

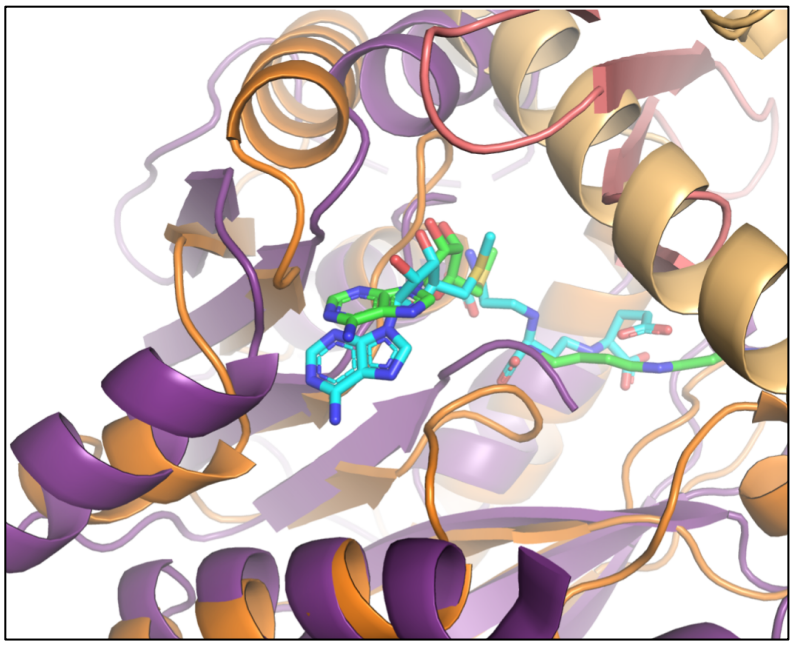

Figure 1-8. Overlay of spermine synthase (SpmSyn; PDB:3c6k; purple) and *M. thermautotrophicus* nicotianamine synthase (MtNAS; PDB:3fpf; orange). A class I SAM binding domain is broadly conserved in each enzyme (dark purple and dark orange) with an rmsd of 4.96 Å over 152 residues. The MTA product is bound in these structures in similar position (green - SpmSyn; cyan - MtNAS;) The N-terminal cap domain which defines the substrate binding pocket has completely different architecture. In SpmSyn the cap domain is predominantly anti-parallel β sheets while the MtNAS cap domain is composed of long α-helices (light purple and light orange). Spermidine (green) is bound to SpmSyn. Thermonicotianamine (cyan) is bound to MtNAS.

MtNAS (4.96 Å rmsd over 152 Cα), but the substrate binding domain is largely β-strand in contrast to the α-helical domain of MtNAS (**Figure 1-8**). Complexes of spermine synthase with MTA and spermine or spermidine demonstrate a mechanism similar to MtNAS where an aspartate/tyrosine pair activate the primary amine of spermine or spermidine to serve as a nucleophile in the attack of C4 of the L-methionine of SAM.

Two other enzyme classes perform SAM-dependent aminoalkyltransfer reactions, but neither are structural homologs of nicotianamine synthases. Aminocyclopropane carboxylate synthase is an enzyme in the ethylene biosynthetic pathway in plants[80]. It uses pyridoxal phosphate to produce 1-aminocyclopropane-1-carboxylate from SAM, generating MTA, and is structurally related to PLP-dependent transferases[69]. Acylhomoserine lactone (AHL) synthases perform aminobutyrate transfers from SAM to an acyl chain donated by an acyl-CoA substrate[81]. This is followed by lactonization by the C1 carboxylate to the C4 carbon of the L-methionine (**Figure 1-6F**). AHL synthases are distant structural homologs of GNAT family enzymes[69].

SAM-dependent aminoalkyltransferases are a diverse family of enzymes that generate a variety of secondary natural products. Within this family, nicotianamine synthase structure and mechanism is poorly understood with a number of open questions remaining. In particular the basis for NAS processivity and the determinants of substrate recognition and azetidine ring formation require further study.

Opine dehydrogenase

The term opine is derived from the molecule N^{α}-(1-R-carboxyethyl)-L-arginine, formed through the condensation of pyruvate and L-arginine and extracted from *Octopus octopodia* muscle tissue (**Figure 1-9A**). It was given the common name octopine by K. Morizawa in 1927[82]. The opine ending has been retained as the common name for compounds formed through condensation of α-keto acids and amino acids. This condensation is performed by an opine dehydrogenase, again the common name for a family NAD(P)H-dependent oxidoreductases (EC

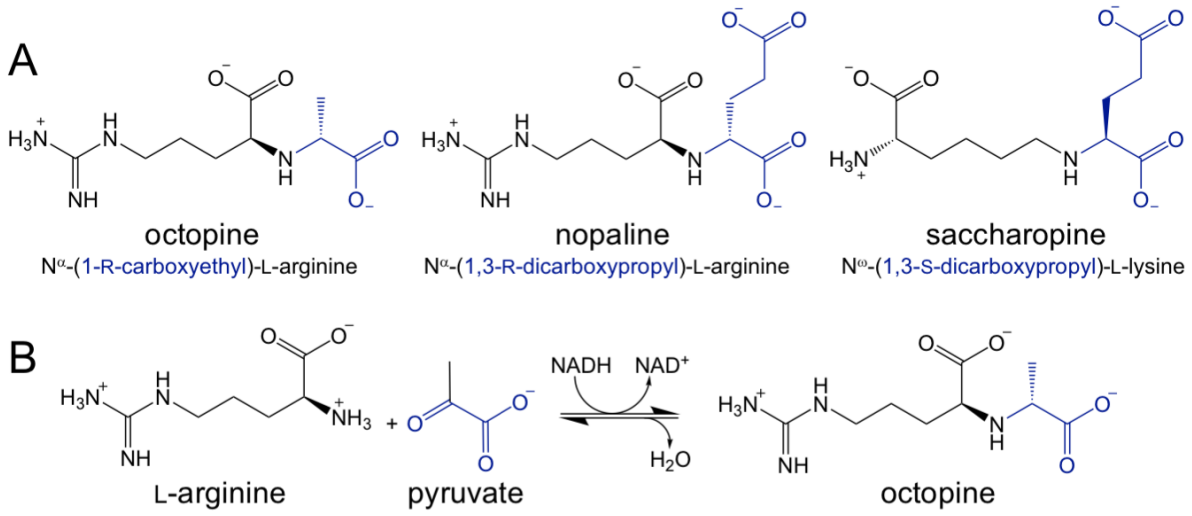

Figure 1-9. A) Common opines. **B)** Octopine biosynthesis.

1.5.1.-) that catalyze the condensation the α or ω amino group from an amino acid with the α-carbon of an α-keto acid (**Figure 1-9B**). Terminology for both the enzyme family and their products is confusing due the frequent use of common names and abbreviations. The topic of nomenclature as well as the occurrence and functional roles of opines has been treated in an extensive review article by Thompson and Donkersloot published in 1992[62]. In the following section, we address nomenclature and summarize key points from the early literature and more recent findings (since 1992) with the objective of providing context for an understanding of opine dehydrogenases involved in opine metallophore biosynthesis.

Opine compounds have frequently been given abbreviated names in the literature. Octopine or N^{α}-(1-R-carboxyethyl)-L-arginine[83], nopaline or N^{α}-(1,3-R-dicarboxypropyl)-L-arginine[84], and saccharopine or N^{ω}-(1,3-S-dicarboxypropyl)-L-lysine[85] are three examples (**Figure 1-5A**). N^{α} designates that the amino group bonded to the Cα of arginine forms a secondary amine by condensation, whereas N^{ω} would designate the ω amino group from the side chain. The α-carbon of the α-keto acid is prochiral and so 1-R-carboxyethyl identifies the stereochemistry of the prochiral carbon after condensation and reduction, and identifies pyruvate as the α-keto acid substrate (carboxymethyl indicates glyoxylate and 1,3-dicarboxypropyl indicates α-ketoglutarate as α-keto acid substrates). Finally, L-arginine designates the amino acid substrate. The enzymes catalyzing these reactions are also frequently referred to using common names without universal standards. For example, octopine synthase, from *Agrobacterium tumifaciens*, and octopine dehydrogenase, from a variety of marine invertebrates, both produce the same compound, octopine, or N^{α}-(1-R-carboxyethyl)-L-arginine. Additionally, many of the enzymes are less specific and generate several products. Octopine synthase can use L-lysine, L-histidine and L-methionine amino acids generating compounds with the common names lysopine, histopine and methiopine respectively[86]. In this text, we will use the term opine dehydrogenase to identify the broad family

of enzymes and the term opine to refer to the product of the condensation reaction performed by opine dehydrogenases.

Despite the naming amalgam, opine dehydrogenases can be distinguished by several defining features. The reaction catalyzed is reversible, as shown in **Figure 1-9A** for octopine dehydrogenase. Both the formation of opines and their hydrolysis is biologically relevant. Opine dehydrogenases typically use NAD(P)H, donating a hydride to reduce the Schiff base intermediate and complete the condensation (an example of a flavin-dependent opine dehydrogenase from *Pseudomonas putida* was recently described[87]). The opine dehydrogenases with X-ray crystal structures that have been deposited in the PDB can be divided into two classes based on structural homology of the domains[88]. A representative of the first class is N-(1-R-carboxyethyl)-L-norvaline dehydrogenase from *Arthrobacter sp.* strain 1C (PDB: 1BG6)[88]. This class contains a Rossmann-like NAD(P)H-binding domain and an α-helical substrate binding or catalytic domain (**Figure 1-10A**). A number of enzymes with homology for this class have been characterized using steady-state kinetic methods. To date members of this group have been shown to produce (R) stereocenters at the prochiral carbon of the α-keto acid upon condensation with an amino acid[89]. The second class of opine dehydrogenases, also called saccharopine dehydrogenases from their identification in *Saccharomyces cerevisiae*, performs the last step in the biosynthesis of lysine in the α-aminoadipate pathway (PDB: 2Q99)[90]. Saccharopine dehydrogenase contains two Rossmann-like fold domains, one responsible for NAD(P)H-binding and the other for substrate binding (**Figure 1-10B**). The characterized members of this second class produce (S) stereocenters at the prochiral carbon of the α-keto acid upon condensation with an amino acid[91]. Interestingly, SaODH, PaODH and YpODH have structural similarity to the (R) forming opine dehydrogenases, but SaODH and the CntA receptor have been investigated using (S)-staphylopine. The accepted chemical mechanism for both enzyme classes involves the deprotonation of the nucleophilic amine of the amino acid (N^{α} or N^{ω}) activating it for an attack on

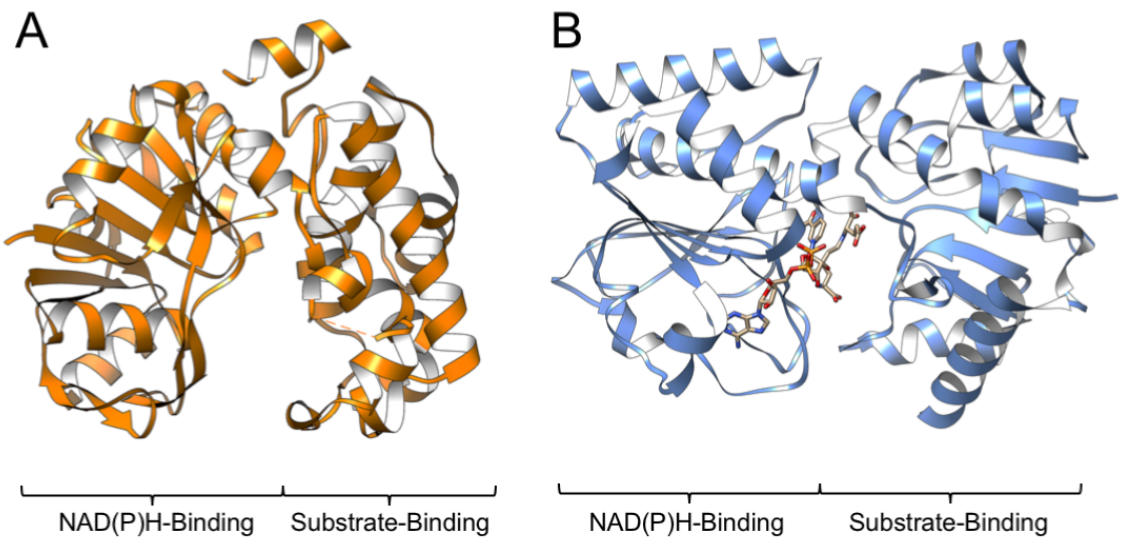

Figure 1-10. Opine dehydrogenase structural differences. A) N^{α}-(1-R-carboxyethyl)-L-norvaline dehydrogenase from *Arthrobacter sp.* strain 1C (PDB:1BG6) containing one Rossmann-like fold domain that binds NAD(P)H (left unmodeled by the authors due to weak nicotinamide density) and one α-helical substrate-binding domain. **B)** Saccharopine dehydrogenase (PDB:3UH1) containing two Rossmann-like fold domains. Shown with bound NADH and saccharopine ligands (tan carbons).

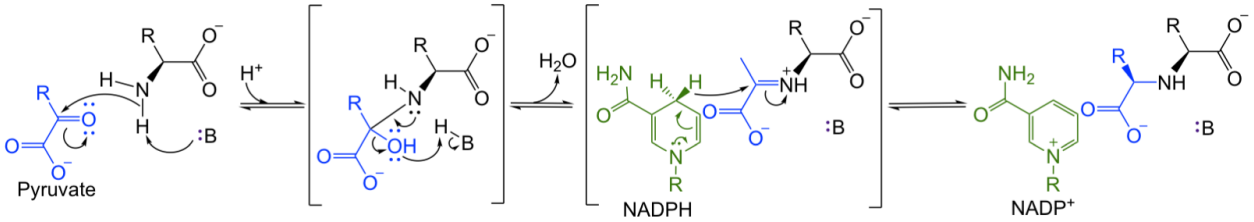

Figure 1-11. General opine dehydrogenase mechanism. Generalized α-keto acid (blue). Generalized amino acid (black). NAD(P)H nicotinamide (green).

carbon C2 of the α-keto acid leading to water release and the formation of a Schiff base intermediate that is reduced by hydride transfer from NAD(P)H forming the opine product[92, 93] (**Figure 1-11**).

The kinetic mechanism of several opine dehydrogenases has been investigated using steady-state analysis in both reaction directions in the presence and absence of inhibitors. Here we summarize the results of this analysis for octopine dehydrogenase (class I) from *Pecten maximus* (king scallop), the best characterized opine dehydrogenase and a structural homolog of opine metallophore-forming opine dehydrogenases. Anna Olomucki and colleagues published an extensive analysis of octopine dehydrogenase from *P. maximus* in over a dozen papers in the 1970's. They are well-written, provide valuable information and offer interesting historical perspective on the field of enzymology. Octopine dehydrogenase was purified from *P. maximus* muscle tissue and the K_m values were determined to be 1.5 mM for the substrates octopine, arginine and pyruvate, 150 μM for NAD^+ and 40 μM for NADH[94] (Scheme in **Figure 9B**). Equilibrium ultracentrifugation was used to determine a molecular weight for the purified enzyme of 38 kDa corresponding to a monomer[95]. Photooxidation experiments demonstrated the protection of histidine by the holoenzyme suggesting its role as a catalytic residue[96, 97]. Circular dichroism demonstrated the αβ structure of the protein and optical-rotatory dispersion experiments showed perturbation upon NADH binding with a 1:1, NADH to enzyme stoichiometry[98]. Small angle X-ray scattering demonstrated a reduction of the radius of gyration by 2.4 Å in the presence of the three substrates, NADH, arginine and pyruvate, suggesting a conformational closure of the holoenzyme[99]. K_d values for NADH (20 μM), NAD^+ (260 μM) and ternary complexes of NADH and octopine (0.9 μM) were determined by intrinsic NADH fluorescence[100, 101]. Hydride transfer from NADH is delivered to the substrate from the *pro*-S face of the nicotinamide as determined using (S) or (R) 4-^{3}H-NADH as a cosubstrate[102].

These foundational studies set the stage for a description of the kinetic mechanism for octopine dehydrogenase in 1975 using initial velocity, product inhibition, pre-steady state burst and hydride transfer isotope effect experiments[103, 104]. Initial velocity and product inhibition studies were performed for each substrate in both the forward and reverse reactions. NADH was found to be a competitive inhibitor of NAD^+ and noncompetitive for (R)-octopine consistent with NAD binding independently of octopine. The authors also observed differing patterns of inhibition for L-arginine and pyruvate suggesting that these substrates bind independently. Burst experiments were carried out on a stopped-flow spectrophotometer with a 3-4 ms dead time using 10 μM octopine dehydrogenase pre-incubated with NAD^+ or NADH and mixed with saturating substrate at high (~6 mM) or low (~200 μM, below K_m) concentrations. At high concentration of (R)-octopine or of L-arginine and pyruvate a burst was observed and that occurred within the dead time of the stopped-flow instrument. Measurement of a (R)-^{2}H-octopine isotope effect for hydride transfer showed smaller secondary isotope effects at high substrate concentration that increased at lower concentrations of substrate. 4S-[4-^{2}H]-NADH showed a small secondary isotope effect independent of concentration. These data led the authors to suggest that product dissociation, and not hydride transfer, is the rate-limiting reaction step for octopine dehydrogenase. While the authors propose an ordered sequential mechanism for the reaction, they note that their data indicate independent binding and release of NADH/NAD^+ and L-arginine, pyruvate/(R)-octopine from the active site.

In 2008, the X-ray crystal structure of octopine dehydrogenase from *P. maximus* (PmODH) was solved with NADH bound at 2.1 Å[105]. PmODH and ArODH (*Arthrobacter sp.* strain 1C) share conserved structure in both the NAD(P)H-binding and α-helical catalytic domains with an r.m.s.d. of 3.89 Å over 208 Cα residues. ArODH and YpODH (*Yersinia pestis*) have higher structural homology with an r.m.s.d. of 2.43 Å over 307 Cα residues (both determined by PDBeFold) (**Figure 1-12**). PmODH crystallized as a monomer consistent with the analytical centrifugation data.

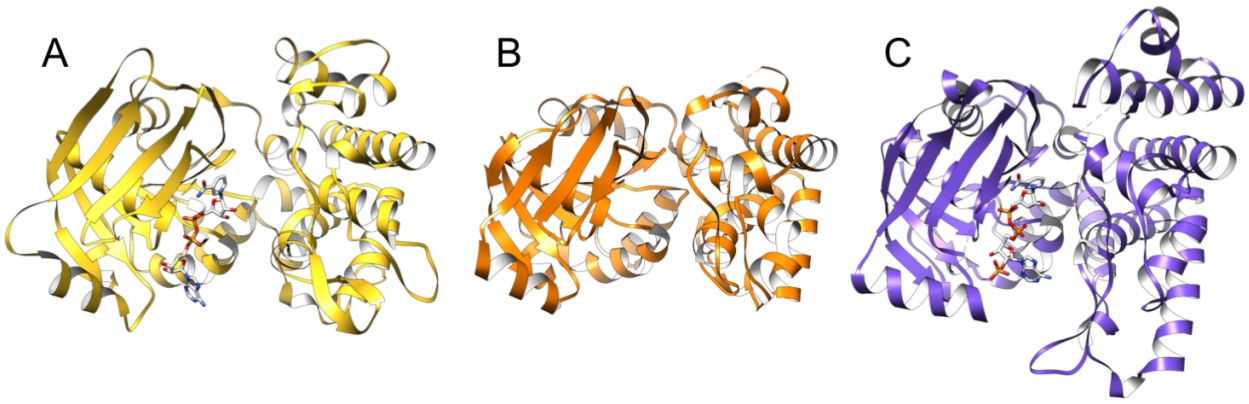

Figure 1-12. Opine dehydrogenases. A. Octopine (N^{α}-(R-1-carboxyethyl)-L-arginine) dehydrogenase from *Pecten maximus* with NADH bound (white carbons). **B.** N^{α}-(1-R-carboxyethyl)-L-norvaline dehydrogenase from *Arthrobacter sp.* Strain 1C. **C.** Yersinopine dehydrogenase from *Yersinia pestis*.

Opine Metallophore Diversity

The study of opine metallophore pathways has thus far been focused on bacterial pathogens and limited to *Staphylococcus aureus*, *Pseudomonas aeruginosa* and a partial characterization of *Yersinia pestis*, but all three of these pathways produce variant opine metallophores[63, 106]. Operons containing a nicotianamine synthase followed by an opine dehydrogenase along with assorted transport and receptor proteins are widespread across bacterial species suggesting that opine metallophores are produced by bacteria growing in a variety of environments. We have used the Enzyme Function Initiative-Enzyme Similarity Tool to explore this diversity[107]. Using PaODH as a query sequence we performed a BLAST search with E value set to 5 and the maximum retrieved sequences set to 1000. A sequence similarity network (SSN) was created using an alignment score threshold of 50 and a sequence length minimum of 420 residues (these cut-offs were chosen to limit hits to those that aligned over the full sequence length which eliminated ~100 sequences). This returned 354 PaODH homologs in a single cluster and these were used to generate a genome neighborhood network. The homolgous sequences from each species in the SSN were also aligned using MUSCLE in MEGA10[108] and used to generate a phylogeny by maximum likelihood methodology. A simplified version of this phylogeny is shown with four groups designated I, II, III and IV in **Figure 1-13A**. A representative selection of the 354 genome neighborhoods analyzed were selected for **Figure 1-13B**. These represent the major phylogenetic groups and illustrate predicted variation in the enzymes present in operons from different species.

Group I is composed of *Staphylococci* with a variety of species including, but not limited to, *S. aureus*, *S. epidermidis, S. xylosus, S. pasteuri, S. warneri, S. chromgenes* and *S. delphini*. Also included are two hits for *Streptococcus pneumoniae* (ODH Uniprot IDs: A0A0U0FDR0 and A0A0Y2A305), though a homologous ODH is not found when searching the *S. pneumoniae* Reference Protein Database within the NCBI blastp suite, suggesting that this operon is not universally conserved in *S. pneumoniae*. A hallmark of the group I organisms is the presence of

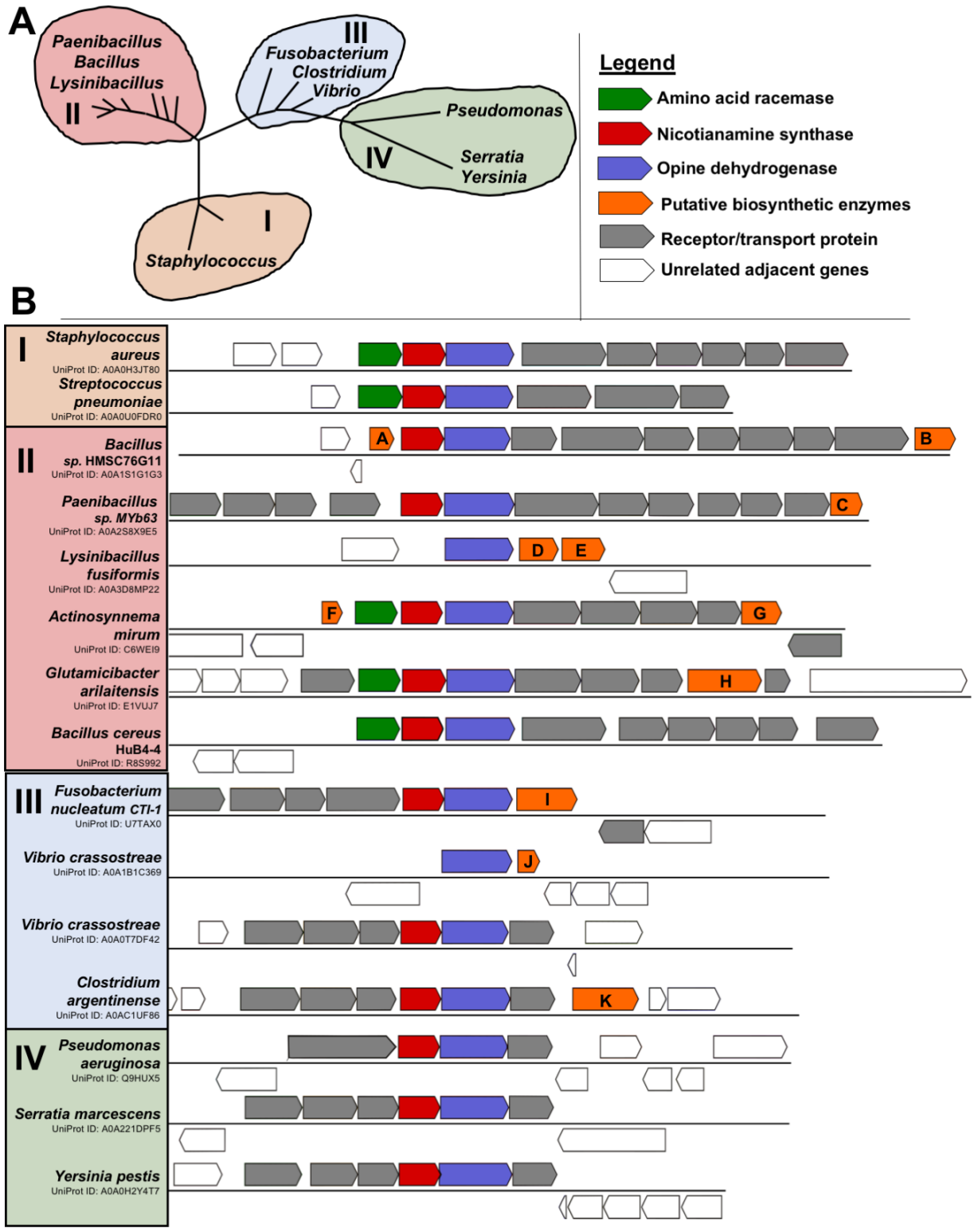
A
Paenibacillus
Bacillus
Lysinibacillus
II
III
Fusobacterium
Clostridium
Vibrio
Pseudomonas
IV
Serratia
Yersinia
I
Staphylococcus
Legend
Amino acid racemase
Nicotianamine synthase
Opine dehydrogenase
Putative biosynthetic enzymes
Receptor/transport protein
Unrelated adjacent genes
B
I
Staphylococcus aureus
UniProt ID: A0A0H3JT80
Streptococcus pneumoniae
UniProt ID: A0A0U0FDR0
II
Bacillus sp. HMSC76G11
UniProt ID: A0A1S1G1G3
Paenibacillus sp. MYb63
UniProt ID: A0A2S8X9E5
Lysinibacillus fusiformis
UniProt ID: A0A3D8MP22
Actinosynnema mirum
UniProt ID: C6WEI9
Glutamicibacter arilaitensis
UniProt ID: E1VUJ7
Bacillus cereus HuB4-4
UniProt ID: R8S992
III
Fusobacterium nucleatum CTI-1
UniProt ID: U7TAX0
Vibrio crassostreae
UniProt ID: A0A1B1C369
Vibrio crassostreae
UniProt ID: A0A0T7DF42
Clostridium argentinense
UniProt ID: A0AC1UF86
IV
Pseudomonas aeruginosa
UniProt ID: Q9HUX5
Serratia marcescens
UniProt ID: A0A221DPF5
Yersinia pestis
UniProt ID: A0A0H2Y4T7
A
B
C
D
E
F
G
H
I
J
K

Figure 1-13. Genome neighborhood network for opine metallophore pathways. A) Simplified phylogeny generated by maximum likelihood method in MEGA10. The full phylogeny contains 354 organisms. **B)** Genome neighborhood network. Produced using Enzyme Function Initiative Genome Neighborhood Tool as described in text. Predicted ODH (blue), predicted NAS (red), predicted racemase (green), predicted enzymes that may contribute in unidentified roles to opine metallophore biosynthesis (orange), predicted transport proteins (gray) and genes predicted not to be associated with opine metallophore production (white). Uniprot description of enzymes predicted and labeled in orange above (in each case the protein was inferred based on sequence and/or homology with ortholog proteins. Gene name is listed first, if available, followed by UniProt protein name): **A.** luxS. S-ribosylhomocysteine lysase **B.** purU. Formyltetrahydrofolate deformylase. **C.** Class I SAM-dependent methyltransferase. **D.** Short-chain dehydrogenase/reductase. **E.** GNAT family N-acetyltransferase. **F.** Uncharacterized protein. **G.** SAM-dependent methyltransferase. **H.** ipdA. Dihydrolipoyl dehydrogenase. **I.** metK. S-adenosylmethionine synthase. **J.** Uncharacterized protein. Possible acyl-CoA-acyltransferase. **K.** Polymerase/histidinol phosphatase domain protein.

a predicted amino acid racemase, most often identified as a predicted diaminopimelate epimerase homolog (E.C. 5.1.1.7). In *S. aureus* this enzyme converts L-histidine to D-histidine[58]. D-Histidine is then incorporated into staphylopine by SaNAS which specifically recognizes the (D) enantiomer[63]. Whether some opine metallophore pathways incorporate a non-histidine amino acid is undetermined, but the presence of an amino acid racemase in the operons of this group suggests that the opine product will conserve stereochemistry at this position.

Groups II and III are very diverse, exhibiting different combinations of both enzymes and predicted transport proteins. The species within these groups have wide-ranging habitats from *Bacillus cereus* found in soil, *Vibrio crassostreae* that colonize oysters[109], and *Glutamicibacter arilaitensis* found on the surface of cheese[110]; to several less common pathogens such as *Fusobacterium nucleatum*, a commensal periodontal pathogen[111], and *Clostridium agentinense*, an anaerobe that produces botulinum toxin[112]. An amino acid racemase is conserved in some, but not all species suggesting differing product stereochemistry, even within the same genus (ex. *Bacillus*). Two rare examples of ODH homologs in the absence of a NAS are found in *Lysinibacillus fusiformis* and *Vibrio crassostreae* (which also has an NAS-containing operon). In both cases predicted transport proteins are absent from the operon, though additional enzymes are present (a short chain dehydrogenase/reductase and GNAT family N-acetyltransferase in *Lysinibacillus fusiformis* and a predicted acyl-Coa-acyltransferase in *Vibrio crassostreae*) suggesting a different functional role for these operons. Several species (ex. Paenibacillus sp. MYb63 and Actinosynnema mirum) contain a predicted class I SAM-dependent methytransferase at the end of the operon. *Glutamicibacter arilaitensis* has a predicted dihydrolipoyl dehydrogenase (E.C. 1.8.1.4, dihydolipoamide:NAD^+ oxidoreducatase), involved in the oxidation dihydrolipoamide to form a disulfide-linked 5-membered ring in lipoamide. What role this enzyme might play within an opine metallophore pathway is unknown, but dihydrolipoyl dehydrogenase homologs are also found just downstream of the pseudopaline operon in *P. aeruginosa*, sometimes annotated as mycothione reductase (E.C. 1.8.1.15). *Clostridium agentinense* encodes

a predicted histidinol phosphatase (E.C. 3.1.3.15) suggesting that L-histindol rather than L-histidine may serve as the substrate for the NAS in *C. argentinense*.

Group IV contains several major human pathogens including *Pseudomonas aeruginosa*, *Serratia marcescens* and *Yersinia pestis*. The operons within these Gram-negative species contain an EamA family inner membrane efflux protein and typically encode inner membrane ABC transport proteins. They do not have an amino acid racemase. In *Pseudomonas aeruginosa*, inner membrane ABC transporters are absent suggesting that this function is encoded elsewhere within the *P. aeruginosa* genome. Despite encoding only two enzymes, an NAS and an ODH, product diversity exists as demonstrated for the *P. aeruginosa* and *Y. pestis* ODH enzymes which utilize α-ketoglutarate and pyruvate respectively[106].

Using the Enzyme Function Initiative-Enzyme Similarity Tool[107], but replacing PaODH with PaNAS as a query sequence, reveals many operons with homologous NAS enzymes that do not contain an ODH. This suggests the presence of nicotianamine-like metallophores in many bacteria that are not "finished" by formation of a secondary amine linkage with an α-keto acid. For this analysis we performed a BLAST search with an E value set to 5 and the maximum retrieved sequences set to 1000. A sequence similarity network (SSN) was created using an alignment score threshold of 15 and no sequence length restrictions. This returned 391 PaNAS homologs in a single cluster and these were used to generate a genome neighborhood network (GNN). The majority of the operons in this GNN were duplicated in our search based on PaODH (above); however, PaNAS homologs were frequently found to exist in the absence of an ODH homolog (unlike the PaODH homologs which rarely existed without a preceding NAS homolog). Here we present nine such operons to demonstrate the existing species and pathway diversity (**Figure 1-14**).

In addition to an NAS, many of these operons contain additional predicted enzymes and likely biosynthesize metallophores with unique chemical structures. The NAS genes varied

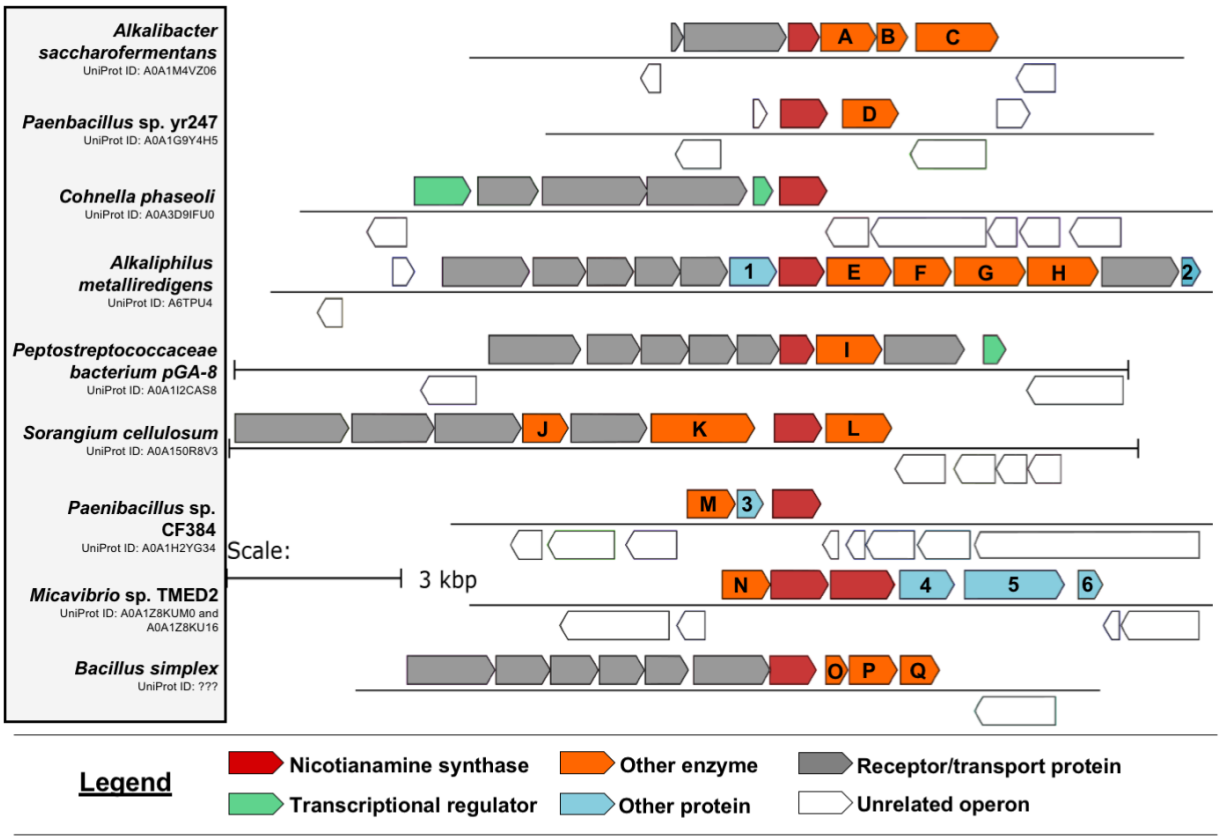

Figure 1-14. Genome neighborhood network of PaNAS homologs. Produced using Enzyme Function Initiative Genome Neighborhood Tool as described in text. Predicted NAS (red), predicted enzymes that may contribute in unidentified roles to nicotianamine-like metallophore biosynthesis (orange), other proteins (blue), predicted transport proteins (gray), genes predicted not to be associated with opine metallophore production (white). UniProt description of enzymes predicted and labeled in orange or blue above (in each case the UniProt protein name given was inferred based on sequence and/or homology with ortholog protein): **A.** Phosphatidylglycerol lysyltransferase **B.** CDP-diacylglycerol-serine O-phosphatidyltransferase **C.** Nicotinate phosphoribosyltransferase **D.** Predicted oxidoreductase **E.** Uncharacterized PLP-dependent protein **F.** Histidyl-tRNA synthetase-like protein **G.** Uncharacterized protein (ATP grasp domain) **H.** Uncharacterized protein (ATP grasp domain) **I.** Uncharacterized PLP-dependent enzyme **J.** Uncharacterized protein (Methyltransferase domain) **K.** Asparagine synthetase B **L.**

Aminotransferase **M.** Aldo/keto reductase **N.** SAM-dependent methyltransferase **O.** Catechol-2,3-dioxygenase membrane subunit **P.** Glyoxylase/bleomycin resistance/dioxygenase **Q.** FMN-dependent NADH-azoreductase **1.** Uncharacterized protein **2.** Uncharacterized protein **3.** Uncharacterized damage-inducible protein **4.** Uncharacterized protein **5.** Uncharacterized protein (TPR motif) **6.** Uncharacterized protein (response regulator)

significantly in length from 182 amino acids for the bacterium *Akalkibacter saccharofermentans* to 374 amino acids in the bacterium *Micavibrio sp. TMED2* suggesting the potential for differences in substrate recognition and/or processivity. As observed for the opine metallophore operons above, diverse niches are again evident for the nicotianamine-like metallophore operons. Examples include *Alkaliphilus metalliredigens*, isolated from sodium borate leachate ponds containing sodium at concentrations of up to 12 g/L and a pH of 9.5[113]; *Cohnella phaseoli*, isolated from runner bean (*Phaseolus coccineus*) root nodules[114]; *Peptostreptococcaceae bacterium pGA-8*, a clostridial species that has been shown to be overrepresented in the human gut microbiome in patients with colorectal cancer[115]; *Micavibrio sp.* TMED2, a predatory bacterium that attaches to the surface of a variety of Gram-negative pathogens to extract nutrients that has been proposed as a potential antimicrobial strategy[116]; and *Sorangium cellulosum*, a soil bacterium known for its 13 Mbp genome, the largest identified bacterial genome[117]. In some operons, rationalizing the hypothetical product is possible. In *Cohnella phaseoli*, the NAS (275 amino acids) is the lone enzyme and likely produces a nicotianamine-like metallophore. The *Micavibrio sp.* TMED2 operon has three predicted enzymes found in association with three additional uncharacterized proteins. The first enzyme is a SAM-dependent methyltransferase. Interestingly, it is followed by two consecutive NAS homologues that are 333 and 374 amino acids respectively, both much larger than PaNAS at 264 amino acids. This operon contains no associated transport function. *Peptostreptococcaceae bacterium pGA-8* encodes transport proteins as well as a NAS and a predicted PLP-dependent enzyme suggesting a transamination of the primary amine of the nicotianamine-like product to a ketone suggesting similarity to mugineic acid biosynthesis (**Figure 1-5**). For many other operons the final product is difficult to predict. In addition to a NAS homologue, *Akaliphilus metalliredigens* contains four additional potential enzymes. The predicted function of these four are an uncharacterized PLP-dependent protein, a histidyl-tRNA synthetase-like protein, and two uncharacterized proteins with ATP-grasp domains often associated with the ligation of carboxylate-containing molecules (often amino acids) with molecules containing thiol

or amino groups. Just this sample of nine NAS-based pathways represent an assortment of novel secondary natural products and likely metallophores.

Conclusion

The biosynthesis of metallophores has been established in a wide range of bacterial, fungal and plant species. Metal acquisition is critical to normal plant growth and is essential to the pathogenesis of many infectious bacteria, as metals are required for cellular metabolism, largely for incorporation into metalloproteins and enzymes. Genes associated with metal acquisition are consistently among the most highly expressed transcripts during infection in both model systems and from human isolates. Metal acquisition represents a core biological process making it both an area of fundamental scientific interest and a potential target for the development of new therapeutics.

Nicotianamine synthase and opine dehydrogenase enzymes work together to produce a new metallophore type, the opine metallophore, with several unique features. This pathway uses comparatively few cellular resources relative to the common, but more complex, NRPS and PKS pathways that generate most metallophores. Opine metallophores have already been shown to be broad spectrum metal chelators bringing multiple transition metals into the bacterial cell under metal-limitation and infectious disease conditions. Nicotianamine synthases are known to produce phytosiderophores in plants, but characterization in the archeal species *M. thermautotrophicus* and the bacterial species *S. aureus* and *P. aeruginosa* demonstrates the prevalence of NAS enzymes in bacterial metallophore biosynthesis. Secondary natural product biosynthesis is a new functional role for opine dehydrogenases that are typically associated with primary metabolism in marine animals and plant-based bacterial infections. Yet the co-occurrence of NAS and ODH enzymes, likely for metallophore production, is frequent for a range of bacteria. Continued study of both the biosynthesis and biological significance of opine metallophores contributes to a vital understanding of the metal acquisition pathways essential to life.

References

[1] Krishna, S. S., Majumdar, I., and Grishin, N. V. (2003) Structural classification of zinc fingers: survey and summary, *Nucleic Acids Res 31*, 532-550.

[2] Thomson, A. J., and Gray, H. B. (1998) Bio-inorganic chemistry, *Current Opinion in Chemical Biology 2*, 4.

[3] Andreini, C., Bertini, I., and Rosato, A. (2009) Metalloproteomes: A Bioinformatic Approach, *Accounts of Chemical Research 42*, 9.

[4] Eklund, H., Uhlin, U., Farnegardh, M., Logan, D. T., and Nordlund, P. (2001) Structure and function of the radical enzyme ribonucleotide reductase, *Progress in Biophysics and Molecular Biology 77*, 92.

[5] Peters, J. W., and Szilagyi, R. K. (2006) Exploring new frontiers of nitrogenase structure and mechanism, *Curr Opin Chem Biol 10*, 101-108.

[6] Hoffman, B. M., Lukoyanov, D., Yang, Z. Y., Dean, D. R., and Seefeldt, L. C. (2014) Mechanism of nitrogen fixation by nitrogenase: the next stage, *Chem Rev 114*, 4041-4062.

[7] Raj, S. B., Ramaswamy, S., and Plapp, B. V. (2014) Yeast alcohol dehydrogenase structure and catalysis, *Biochemistry 53*, 5791-5803.

[8] Lindskog, S. (1997) Structure and Mechanism of Carbonic Anhydrase, *Pharmcol. Ther. 74*, 20.

[9] Hart, P. J., Balbirnie, M. M., Ogihara, N. L., Nersissian, A. M., Weiss, M. S., Valentine, J. S., and Eisenberg, D. (1999) A Structure-Based Mechanism for Copper-Zinc Superoxide Dismutase, *Biochemistry 38*, 12.

[10] Benini, S., Rypniewski, W. R., Wilson, K. S., Miletti, S., Ciurli, S., and Mangani, S. (1999) A new proposal for urease mechanism based on the crystal structures of the native and inhibited enzyme from Bacillus pasteurii: why urea hydrolysis costs two nickels, *Structure 7*, 205-216.

[11] Mobley, H. (1996) The role of Helicobacter pylori urease in the pathogenesis of gastritis and peptic ulceration, *Alimentary pharmacology & therapeutics 10*, 57-64.

[12] Konieczna, I., Zarnowiec, P., Kwinkowski, M., Kolesinska, B., Fraczyk , J., Kaminski, Z., and Kaca, W. (2012) Bacterial Urease and its Role in Long-Lasting Human Disease, *Current Protein and Peptide Science 13*, 789-806.

[13] Banerjee, R., and Ragsdale, S. W. (2003) The Many Faces of Vitamin B12: Catalysis by Cobalamin-Dependent Enzymes, *Annual Review of Biochemistry 72*, 209-247.

[14] Latimer, W. M. (1938) *The oxidation states of the elements and their potentials in aqueous solutions*, Prentice Hall, New York.

[15] Biedermann, G., and Schinler, P. (1957) On the Solubility Product of Precipitated Iron (III) Hydroxide, *Acta Chem. Scand. 11*, 10.

[16] Cunrath, O., Geoffroy, V. A., and Schalk, I. J. (2016) Metallome of Pseudomonas aeruginosa: a role for siderophores, *Environ Microbiol 18*, 3258-3267.

[17] Schalk, I. J., and Cunrath, O. (2016) An overview of the biological metal uptake pathways in Pseudomonas aeruginosa, *Environ Microbiol 18*, 3227-3246.

[18] Kammler, M., Schon, C., and Hantke, K. (1993) Characterization of the Ferrous Iron Uptake System of *Escherichia coli*, *Journal of Bacteriology 175*, 8.

[19] Ochsner, U. A., Johnson, Z., and Vasil, M. L. (2000) Genetics and regulation of two distinct haem-uptake systems, *phu* and *has*, in *Pseudomonas aeruginosa*, *Microbiology 146*, 14.

[20] Lansky, I. B., Lukat-Rodgers, G. S., Block, D., Rodgers, K. R., Ratliff, M., and Wilks, A. (2006) The cytoplasmic heme-binding protein (PhuS) from the heme uptake system of Pseudomonas aeruginosa is an intracellular heme-trafficking protein to the delta-regioselective heme oxygenase, *J Biol Chem 281*, 13652-13662.

[21] Barker, K. D., Barkovits, K., and Wilks, A. (2012) Metabolic flux of extracellular heme uptake in Pseudomonas aeruginosa is driven by the iron-regulated heme oxygenase (HemO), *J Biol Chem 287*, 18342-18350.
[22] Pederick, V. G., Eijkelkamp, B. A., Begg, S. L., Ween, M. P., McAllister, L. J., Paton, J. C., and McDevitt, C. A. (2015) ZnuA and zinc homeostasis in Pseudomonas aeruginosa, *Sci Rep 5*, 13139.
[23] Yoneyama, H., and Nakae, T. (1996) Protein C (OprC) of the outer membrane of *Pseudomonas aeruginosa* is a copper-regulated channel protein, *Microbiology 142*, 8.
[24] Frangipani, E., and Haas, D. (2009) Copper acquisition by the SenC protein regulates aerobic respiration in Pseudomonas aeruginosa PAO1, *FEMS Microbiol Lett 298*, 234-240.
[25] Pederick, V. G., Eijkelkamp, B. A., Ween, M. P., Begg, S. L., Paton, J. C., and McDevitt, C. A. (2014) Acquisition and role of molybdate in Pseudomonas aeruginosa, *Appl Environ Microbiol 80*, 6843-6852.
[26] Johnstone, T. C., and Nolan, E. M. (2015) Beyond iron: non-classical biological functions of bacterial siderophores, *Dalton Trans 44*, 6320-6339.
[27] Pearson, R. G. (1963) Hard and Soft Acids and Bases, *J Am Chem Soc 85*:22, 3533-3539.
[28] Duckworth, O. W., Bargar, J. R., and Sposito, G. (2009) Quantitative Structure-Activity Relationships for Aqueous Metal-Siderophore Complexes, *Environ. Sci. Technol. 43*, 343.
[29] Ferguson, A. D. (2002) Structural Basis of Gating by the Outer Membrane Transporter FecA, *Science (American Association for the Advancement of Science) 295*, 1715-1719.
[30] Guerinot, M. L., Meidl, E. J., and Plessner, O. (1990) Citrate as a Siderophore in *Bradyrhizobium japonicum*, *Journal of Bacteriology 172*, 6.
[31] Madsen, J. L., Johnstone, T. C., and Nolan, E. M. (2015) Chemical Synthesis of Staphyloferrin B Affords Insight into the Molecular Structure, Iron Chelation, and Biological Activity of a Polycarboxylate Siderophore Deployed by the Human Pathogen Staphylococcus aureus, *J Am Chem Soc 137*, 9117-9127.
[32] Sugiura, Y., and Tanaka, H. (1981) Structure, Properties, and Transport Mechanism of Iron(III) Complex of Mugineic Acid, a Possible Phytosiderophore, *J Am Chem Soc 103*, 4.
[33] Romheld, V. (1991) The role of phytosiderophores in acquisition of iron and other micronutrients in graminaceous species: An ecological approach, *Plant and Soil 130*, 8.
[34] Albrecht-Gary, A.-M., Blanc, S., Rochel, N., Ocaktan, A. Z., and Abdallah, M. A. (1994) Bacterial Iron Transport: Coordination Properties of Pyoverdin PaA, a Peptidic Siderophore of Pseudomonas aeruginosa, *Inorganic Chemistry 33*, 6391-6402.
[35] Meyer, J., Neely, A., Stintzi, A., Georges, C., and Holder, I. A. (1996) Pyoverdin is essential for virulence of Pseudomonas aeruginosa, *Infection and Immunity 64*, 518-523.
[36] Brandel, J., Humbert, N., Elhabiri, M., Schalk, I. J., Mislin, G. L., and Albrecht-Gary, A. M. (2012) Pyochelin, a siderophore of Pseudomonas aeruginosa: physicochemical characterization of the iron(III), copper(II) and zinc(II) complexes, *Dalton Trans 41*, 2820-2834.
[37] Braud, A., Hoegy, F., Jezequel, K., Lebeau, T., and Schalk, I. J. (2009) New insights into the metal specificity of the Pseudomonas aeruginosa pyoverdine-iron uptake pathway, *Environ Microbiol 11*, 1079-1091.
[38] Teitzel, G. M., Geddie, A., De Long, S. K., Kirisits, M. J., Whiteley, M., and Parsek, M. R. (2006) Survival and growth in the presence of elevated copper: transcriptional profiling of copper-stressed Pseudomonas aeruginosa, *J Bacteriol 188*, 7242-7256.
[39] Osman, D., and Cavet, J. S. (2008) Chapter 8 - Copper Homeostasis in Bacteria, In *Advances in Applied Microbiology* (Laskin, A. I., Sariaslani, S., and Gadd, G. M., Eds.), pp 217-247, Academic Press.

[40] Semrau, J. D., DiSpirito, A. A., and Yoon, S. (2010) Methanotrophs and copper, *FEMS Microbiol Rev 34*, 496-531.
[41] Kenney, G. E., and Rosenzweig, A. C. (2018) Chalkophores, *Annual Review of Biochemistry 87*, 645-676.
[42] Gellatly, S. L., and Hancock, R. E. (2013) Pseudomonas aeruginosa: new insights into pathogenesis and host defenses, *Pathog Dis 67*, 159-173.
[43] Lyczak, J., Cannon, C. L., and Pier, G. B. (2000) Establishment of *Pseudomonas aeruginosa* infection: lessons from a versitile opportunist, *Microbes and Infection 2*, 10.
[44] Winsor, G. L., Griffiths, E. J., Lo, R., Dhillon, B. K., Shay, J. A., and Brinkman, F. S. (2016) Enhanced annotations and features for comparing thousands of Pseudomonas genomes in the Pseudomonas genome database, *Nucleic Acids Res 44*, D646-653.
[45] Mastropasqua, M. C., D'Orazio, M., Cerasi, M., Pacello, F., Gismondi, A., Canini, A., Canuti, L., Consalvo, A., Ciavardelli, D., Chirullo, B., Pasquali, P., and Battistoni, A. (2017) Growth of Pseudomonas aeruginosa in zinc poor environments is promoted by a nicotianamine-related metallophore, *Mol Microbiol 106*, 543-561.
[46] Lhospice, S., Gomez, N. O., Ouerdane, L., Brutesco, C., Ghssein, G., Hajjar, C., Liratni, A., Wang, S., Richaud, P., Bleves, S., Ball, G., Borezée-Durant, E., Lobinski, R., Pignol, D., Arnoux, P., and Voulhoux, R. (2017) Pseudomonas aeruginosa zinc uptake in chelating environment is primarily mediated by the metallophore pseudopaline, *Scientific Reports 7*, 1-10.
[47] Gi, M., Lee, K. M., Kim, S. C., Yoon, J. H., Yoon, S. S., and Choi, J. Y. (2015) A novel siderophore system is essential for the growth of Pseudomonas aeruginosa in airway mucus, *Sci Rep 5*, 1-15.
[48] Doerks, T., Copley, R. R., Schultz, J., Ponting, C. P., and Bork, P. (2002) Systematic identification of novel protein domain families associated with nuclear functions, *Genome Res 12*, 47-56.
[49] Bielecki, P., Puchalka, J., Wos-Oxley, M. L., Loessner, H., Glik, J., Kawecki, M., Nowak, M., Tummler, B., Weiss, S., and dos Santos, V. A. (2011) In-vivo expression profiling of Pseudomonas aeruginosa infections reveals niche-specific and strain-independent transcriptional programs, *PLoS One 6*, e24235.
[50] Bielecki, P., Komor, U., Bielecka, A., Musken, M., Puchalka, J., Pletz, M. W., Ballmann, M., Martins dos Santos, V. A., Weiss, S., and Haussler, S. (2013) Ex vivo transcriptional profiling reveals a common set of genes important for the adaptation of Pseudomonas aeruginosa to chronically infected host sites, *Environ Microbiol 15*, 570-587.
[51] Damron, F. H., Oglesby-Sherrouse, A. G., Wilks, A., and Barbier, M. (2016) Dual-seq transcriptomics reveals the battle for iron during Pseudomonas aeruginosa acute murine pneumonia, *Sci Rep 6*, 39172.
[52] Wertheim, H. F. L., Melles, D. C., Vos, M. C., van Leeuwen, W., van Belkum, A., Verbrugh, H. A., and Nouwen, J. L. (2005) The role of nasal carriage in Staphylococcus aureus infections, *The Lancet Infectious Diseases 5*, 751-762.
[53] Tong, S. Y., Davis, J. S., Eichenberger, E., Holland, T. L., and Fowler, V. G., Jr. (2015) Staphylococcus aureus infections: epidemiology, pathophysiology, clinical manifestations, and management, *Clin Microbiol Rev 28*, 603-661.
[54] CDC. (2016) Antibiotic/ Antimicrobial Resistance: Biggest Threats, Centers for Disease Control and Prevention, https://www.cdc.gov/drugresistance/biggest_threats.html.
[55] Hiron, A., Posteraro, B., Carriere, M., Remy, L., Delporte, C., La Sorda, M., Sanguinetti, M., Juillard, V., and Borezee-Durant, E. (2010) A nickel ABC-transporter of Staphylococcus aureus is involved in urinary tract infection, *Mol Microbiol 77*, 1246-1260.
[56] Remy, L., Carriere, M., Derre-Bobillot, A., Martini, C., Sanguinetti, M., and Borezee-Durant, E. (2013) The Staphylococcus aureus Opp1 ABC transporter imports nickel and cobalt in zinc-depleted conditions and contributes to virulence, *Mol Microbiol 87*, 730-743.

[57] Lebrette, H., Borezee-Durant, E., Martin, L., Richaud, P., Boeri Erba, E., and Cavazza, C. (2015) Novel insights into nickel import in Staphylococcus aureus: the positive role of free histidine and structural characterization of a new thiazolidine-type nickel chelator, *Metallomics 7*, 613-621.
[58] Ghssein, G., Brutesco, C., Ouerdane, L., Fojcik, C., Izaute, A., Wang, S. L., Hajjar, C., Lobinski, R., Lemaire, D., Richaud, P., Voulhoux, R., Espaillat, A., Cava, F., Pignol, D., Borezee-Durant, E., and Arnoux, P. (2016) Biosynthesis of a broad-spectrum nicotianamine-like metallophore in Staphylococcus aureus, *Science 352*, 1105-1109.
[59] Song, L., Zhang, Y., Chen, W., Gu, T., Zhang, S. Y., and Ji, Q. (2018) Mechanistic insights into staphylopine-mediated metal acquisition, *Proc Natl Acad Sci U S A*.
[60] Dreyfus, C., Lemaire, D., Mari, S., Pignol, D., and Arnoux, P. (2009) Crystallographic snapshots of iterative substrate translocations during nicotianamine synthesis in Archaea, *Proc Natl Acad Sci U S A 106*, 16180-16184.
[61] Higuichi, K., Kanazawa, K., Nishizawa, N.-K., Chino, M., and Mori, S. (1994) Purification and characterization of nicotianamine synthase form Fe-deficient barley roots, *Plant and Soil 165*, 7.
[62] Thompson, J., and Donkersloot, J. A. (1992) N-(Carboxyalkyl) Amino Acids: Occurence, Synthesis, and Functions, *Annu Rev Biochem 61*, 40.
[63] McFarlane, J. S., and Lamb, A. L. (2017) Biosynthesis of an Opine Metallophore by Pseudomonas aeruginosa, *Biochemistry 56*, 5967-5971.
[64] Grim, K. P., San Francisco, B., Radin, J. N., Brazel, E. B., Kelliher, J. L., Parraga Solorzano, P. K., Kim, P. C., McDevitt, C. A., and Kehl-Fie, T. E. (2017) The Metallophore Staphylopine Enables Staphylococcus aureus To Compete with the Host for Zinc and Overcome Nutritional Immunity, *MBio 8*, 1-16.
[65] Fojcik, C., Arnoux, P., Ouerdane, L., Aigle, M., Alfonsi, L., and Borezee-Durant, E. (2018) Independent and cooperative regulation of staphylopine biosynthesis and trafficking by Fur and Zur, *Mol Microbiol*.
[66] Hermansen, G. M. M., Hansen, M. L., Khademi, S. M. H., and Jelsbak, L. (2018) Intergenic evolution during host adaptation increases expression of the metallophore pseudopaline in Pseudomonas aeruginosa, *Microbiology*.
[67] Shojima, S., Nishizawa, N., Fushiya, S., Nozoe, S., Irifune, T., and Mori, S. (1990) Biosynthesis of Phytosiderophores, *Plant Physiol 93*, 1497-1503.
[68] Kawai, S., Itoh, K., and Takagi, S.-i. (1993) Incorporation of 15N and 14C of methionine into the mugineic acid family of phytosiderophores in iron-deficient barley roots, *Physiologia Plantarum 88*, 7.
[69] Kozbial, P. Z., and Mushegian, A. R. (2005) Natural history of S-adenosylmethionine-binding proteins, *BMC Struct Biol 5*, 19.
[70] Higuchi, K., Suzuki, K., Nakanishi, H., Yamaguichi, H., Nishizawa, N.-K., and Mori, S. (1999) Cloning of Nicotianamine Synthase Genes, Novel Genes Involved in the Biosynthesis of Phytosiderophores, *Plant Physiol 119*, 9.
[71] Ma, J. F., Shinada, T., Matsuda, C., and Nomoto, K. (1995) Biosynthesis of Phytosiderophores, Mugineic Acids, Associated with Methionine Cycling, *The Journal of Biological Chemistry 270*, 6.
[72] Ma, J. F., and Nomoto, K. (1994) Biosynthetic pathways of 3-epihydroxymugineic acid and 3-hydroxymugineic acid in gramineous plants, *Soil Science and Plant Nutrition 40*, 311-317.
[73] Dreyfus, C., Larrouy, M., Cavelier, F., Martinez, J., Pignol, D., and Arnoux, P. (2011) The crystallographic structure of thermoNicotianamine synthase with a synthetic reaction intermediate highlights the sequential processing mechanism, *Chem Commun (Camb) 47*, 5825-5827.

[74] Kawai, S., Itoh, K., Takagi, S.-i., Iwashita, T., and Nomoto, K. (1988) Studies on Phytosiderophores: Biosynthesis of Mugineic Acid and 2'-Deoxymugineic Acid in *Hordeum vulgare* L. Var. Minorimugi, *Tetrahedron Letters 29*, 4.
[75] Yan, F., and Muller, R. (2019) Class I Methyltransferase VioH Catalyzes Unusual S-Adenosyl-l-methionine Cyclization Leading to 4-Methylazetidinecarboxylic Acid Formation during Vioprolide Biosynthesis, *ACS Chem Biol 14*, 99-105.
[76] Fowden, L. (1956) Azetidine-2-carboxylic Acid: a New Cyclic Imino Acid Occurring in Plants, *Biochem. J. 64*, 10.
[77] Wu, H., Min, J., Zeng, H., McCloskey, D. E., Ikeguchi, Y., Loppnau, P., Michael, A. J., Pegg, A. E., and Plotnikov, A. N. (2008) Crystal structure of human spermine synthase: implications of substrate binding and catalytic mechanism, *J Biol Chem 283*, 16135-16146.
[78] Wu, H., Min, J., Ikeguchi, Y., Zeng, H., Dong, A., Loppnau, P., Pegg, A. E., and Plotnikov, A. N. (2007) Structure and mechanim of spermidine synthases, *Biochemistry 46*, 8331-8339.
[79] Miller-Fleming, L., Olin-Sandoval, V., Campbell, K., and Ralser, M. (2015) Remaining Mysteries of Molecular Biology: The Role of Polyamines in the Cell, *Journal of Molecular Biology 427*, 3389-3406.
[80] Yu, Y.-B., Adams, D. O., and Yang, S. F. (1979) 1-Aminocyclopropanecarboxylate synthase, a key enzyme in ethylene biosynthesis, *Arch Biochem Biophys 198*, 7.
[81] Dong, S. H., Frane, N. D., Christensen, Q. H., Greenberg, E. P., Nagarajan, R., and Nair, S. K. (2017) Molecular basis for the substrate specificity of quorum signal synthases, *Proc Natl Acad Sci U S A 114*, 9092-9097.
[82] Morizawa, K. (1927) The extractive substances in *Octopus octopodia*, *Acta Scholae Medicinalis Universitatis Imperialis in Kioto 9*, 14.
[83] Van Thoai, N., and Robin, Y. (1959) Biosynthése de L'octopine et Répartition de L'enzyme L'opérant Chez Les Invertebrés, *Biochim Biophys Acta 35*, 446-453.
[84] Kemp, J. D., Sutton, D. W., and Hack, E. (1979) Purification and characterization of the crown gall specific enzyme nopaline synthase, *Biochemistry 18*, 6.
[85] Darling, S., and Larsen, P. O. (1961) Saccharopine, a new amino acid in Baker's and Brewer's yeast: 1. Isolation and properties, *Acta Chem. Scand. 15*, 7.
[86] Hack, E., and Kemp, J. D. (1980) Purification and Characterization of the Crown Gall-specific Enzyme, Octopine Synthase, *Plant Physiol 65*, 7.
[87] Watanabe, S., Sueda, R., Fukumori, F., and Watanabe, Y. (2015) Characterization of Flavin-Containing Opine Dehydrogenase from Bacteria, *PLoS One 10*, e0138434.
[88] K.L. Britton, Y. A. a. D. W. R. (1998) Crystal structure and active site location of N-(1-D-carboxylethyl)-L-norvaline dehydrogenase, *Nature Structural Biology 5*, 9.
[89] Biellmann, J., Branlant, G., and Wallen, L. (1977) Stereochemistry of octopine and of its isomers and their enzymatic properties, *Bioorganic Chemistry 6*, 89-93.
[90] Andi, B., Xu, H., Cook, P. F., and West, A. H. (2007) Crystal Structures of Ligand-Bound Saccharopine Dehydrogenase from Saccharomyces cerevisiae, *Biochemistry 46*, 12512-12521.
[91] Fujioka, M., and Tanaka, M. (1978) Enzymatic and Chemical Synthesis of *European Journal of Biochemistry 90*, 4.
[92] Muller, A., Janssen, F., and Grieshaber, M. K. (2007) Putative reaction mechanism of heterologously expressed octopine dehydrogenase from the great scallop, Pecten maximus (L), *FEBS J 274*, 6329-6339.
[93] Kumar, V. P., Thomas, L. M., Bobyk, K. D., Andi, B., Cook, P. F., and West, A. H. (2012) Evidence in support of lysine 77 and histidine 96 as acid-base catalytic residues in saccharopine dehydrogenase from Saccharomyces cerevisiae, *Biochemistry 51*, 857-866.

[94] Van Thoai, N., Huc, C., Ba Pho, D., and Olomucki, A. (1969) Octopine déshydrogénase Purification et propriétés catalytiques, *Biochimica et Biophysica Acta (BBA) - Enzymology 191*, 46 - 57.
[95] Olomucki, A., Huc, C., Lefebure, F., and van Thoai, N. (1972) Octopine Dehydrogenase: Evidence for a Single-Chain Structure, *European Journal of Biochemistry 28*, 261-268.
[96] Huc, C., Olomucki, A., Lé-Thi-Lan, Pho, D. B., and van Thoai, N. (1971) Essential Histidyl Residues of Octopine Dehydrogenase, *European Journal of Biochemistry 21*, 161-169.
[97] Thoméa-Beau, F., and Olomucki, A. (1973) Presence of a Single Essential Histidyl Residue in Octopine Dehydrogenase as Shown by Photooxidation, *European Journal of Biochemistry 39*, 557-562.
[98] Oriol, C., and Olomucki, A. (1972) Spectropolarimetric Studies of Binary and Ternary Complexes of Octopine Dehydrogenase, *European Journal of Biochemistry 29*, 288-292.
[99] Thome, F., Vachette, P., Dubord, C., and Olomucki, A. (1987) Conformational changes in octopine dehydrogenase induced by the binding of ligands, *Biochimica et Biophysica Acta (BBA) - Protein Structure and Molecular Enzymology 915*, 4.
[100] Luisi, P. L., Olomucki, A., Baici, A., and Karlovic, D. (1973) Fluorescence properties of octopine dehydrogenase, *Biochemistry 12*, 4100-4106.
[101] BAICI, A., LUISI, P. L., OLOMUCKI, A., DOUBLET, M.-O., and KLINCAK, J. (1974) Influence of Ligands on the Coenzyme Dissociation Constants in Octopine Dehydrogenase, *European Journal of Biochemistry 46*, 59-66.
[102] Biellmann, J. B., G; Olomucki, A. (1973) Sterochemistry of the hydrogen transfer to the coenzyme by octopine dehydrogenase, *FEBS Letters 32*, 3.
[103] Doublet, M. O., A. (1975) Investigations on the Kinetic Mechanism of OctopineDehydrogenase Part 1, *European Journal of Biochemistry 59*, 9.
[104] Doublet, M. O., A; Baici, A; Luisi, P.L. (1975) Investigations on the Kinetic Mechanism of OctopineDehydrogenase Part 2, *European Journal of Biochemistry 59*, 7.
[105] Smits, S. H., Mueller, A., Schmitt, L., and Grieshaber, M. K. (2008) A structural basis for substrate selectivity and stereoselectivity in octopine dehydrogenase from Pecten maximus, *J Mol Biol 381*, 200-211.
[106] McFarlane, J. S., Davis, C. L., and Lamb, A. L. (2018) Staphylopine, pseudopaline and yersinopine dehydrogenases: a structural and kinetic analysis of a new functional class of opine dehydrogenase, *J Biol Chem*.
[107] Zallot, R., Oberg, N. O., and Gerlt, J. A. (2018) 'Democratized' genomic enzymology web tools for functional assignment, *Curr Opin Chem Biol 47*, 77-85.
[108] Tamura, K., Stecher, G., Peterson, D., Filipski, A., and Kumar, S. (2013) MEGA6: Molecular Evolutionary Genetics Analysis version 6.0, *Mol Biol Evol 30*, 2725-2729.
[109] Bruto, M., James, A., Petton, B., Labreuche, Y., Chenivesse, S., Alunno-Bruscia, M., Polz, M. F., and Le Roux, F. (2017) Vibrio crassostreae, a benign oyster colonizer turned into a pathogen after plasmid acquisition, *ISME J 11*, 1043-1052.
[110] Monnet, C., Loux, V., Gibrat, J. F., Spinnler, E., Barbe, V., Vacherie, B., Gavory, F., Gourbeyre, E., Siguier, P., Chandler, M., Elleuch, R., Irlinger, F., and Vallaeys, T. (2010) The arthrobacter arilaitensis Re117 genome sequence reveals its genetic adaptation to the surface of cheese, *PLoS One 5*, e15489.
[111] Han, Y. W. (2015) Fusobacterium nucleatum: a commensal-turned pathogen, *Curr Opin Microbiol 23*, 141-147.
[112] Halpin, J. L., Hill, K., Johnson, S. L., Bruce, D. C., Shirey, T. B., Dykes, J. K., and Luquez, C. (2017) Finished Whole-Genome Sequence of Clostridium argentinense Producing Botulinum Neurotoxin Type G, *Genome Announc 5*.
[113] Roh, Y., Chon, C.-M., and Moon, J.-W. (2007) Metal reduction and biomineralization by an alkaliphilic metal-reducing bacterium, *Akaliphilus metalliredigens* (QYMF), *Geosciences Journal 11*, 9.

[114] Garcia-Fraile, P., Velazquez, E., Mateos, P. F., Martinez-Molina, E., and Rivas, R. (2008) Cohnella phaseoli sp. nov., isolated from root nodules of Phaseolus coccineus in Spain, and emended description of the genus Cohnella, *Int J Syst Evol Microbiol 58*, 1855-1859.
[115] Ahn, J., Sinha, R., Pei, Z., Dominianni, C., Wu, J., Shi, J., Goedert, J. J., Hayes, R. B., and Yang, L. (2013) Human gut microbiome and risk for colorectal cancer, *J Natl Cancer Inst 105*, 1907-1911.
[116] Dashiff, A., Junka, R. A., Libera, M., and Kadouri, D. E. (2011) Predation of human pathogens by the predatory bacteria Micavibrio aeruginosavorus and Bdellovibrio bacteriovorus, *J Appl Microbiol 110*, 431-444.
[117] Schneiker, S., Perlova, O., Kaiser, O., Gerth, K., Alici, A., Altmeyer, M. O., Bartels, D., Bekel, T., Beyer, S., Bode, E., Bode, H. B., Bolten, C. J., Choudhuri, J. V., Doss, S., Elnakady, Y. A., Frank, B., Gaigalat, L., Goesmann, A., Groeger, C., Gross, F., Jelsbak, L., Jelsbak, L., Kalinowski, J., Kegler, C., Knauber, T., Konietzny, S., Kopp, M., Krause, L., Krug, D., Linke, B., Mahmud, T., Martinez-Arias, R., McHardy, A. C., Merai, M., Meyer, F., Mormann, S., Munoz-Dorado, J., Perez, J., Pradella, S., Rachid, S., Raddatz, G., Rosenau, F., Ruckert, C., Sasse, F., Scharfe, M., Schuster, S. C., Suen, G., Treuner-Lange, A., Velicer, G. J., Vorholter, F. J., Weissman, K. J., Welch, R. D., Wenzel, S. C., Whitworth, D. E., Wilhelm, S., Wittmann, C., Blocker, H., Puhler, A., and Muller, R. (2007) Complete genome sequence of the myxobacterium Sorangium cellulosum, *Nat Biotechnol 25*, 1281-1289.

Chapter 2

Biosynthesis of an Opine Metallophore by *Pseudomonas aeruginosa*

Previously published as: McFarlane, J. S. and Lamb, A. L. (2017) Biosynthesis of an Opine Metallophore by *Pseudomonas aeruginosa*, *Biochemistry*. 56, 5967-5971.

Introduction

Pseudomonas aeruginosa produces two well characterized siderophores, pyoverdin and pyochelin, but a recent report suggests that an uncharacterized *P. aeruginosa* operon may be generating a novel nicotianamine-like metallophore[1]. A subsequent study confirmed the presence of a homologous operon in *Staphylococcus aureus* and identified the biosynthetic product, a metallophore that was named staphylopine. The staphylopine operon encodes three enzymes, a histidine racemase (CntK), a nicotianamine synthase (CntL) and an opine dehydrogenase (CntM)[2] (**Figure 2-1**).

The first enzyme, the histidine racemase, converts L-histidine to D-histidine. The second enzyme shares sequence identity with nicotianamine synthases (NAS), enzymes with *S*-adenosyl-L-methionine (SAM) dependent aminoalkyl transferase activity. Nicotianamine is a plant metallophore consisting of three aminobutyrate moieties derived from SAM. NAS enzymes transfer the aminobutyrate moiety in a reaction similar to that performed by spermidine synthase, which uses decarboxy-*S*-adenosyl-L-methionine as a substrate[3]. In *S. aureus,* NAS links the aminobutyrate moiety of SAM to the primary amine of D-histidine. This product then acts as a substrate for an opine dehydrogenase, the final enzyme in the pathway. Opine dehydrogenases (ODH) typically form a secondary amine by condensation of an amino acid with an α-keto acid. Opine products are diverse, as identified in crown gall tumors formed by *Agrobacterium tumefaciens*. In these infections, bacterial DNA encoding a variety of opine dehydrogenases is incorporated into the plant genome. The plant then produces opines, utilizing amino acids such as leucine and arginine and α-keto acids such as α-ketoglutarate and pyruvate, providing an

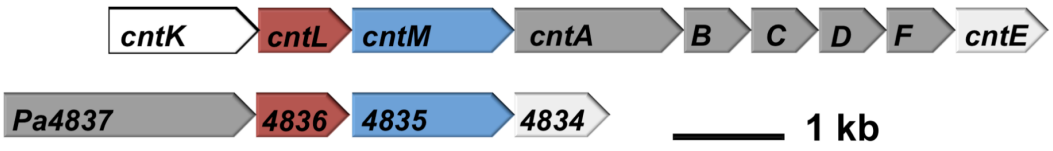

Figure 2-1. Map of homologous operons. Gene arrangement in opine metallophore operons. Upper: *S. aureus*. Lower: *P. aeruginosa*. CntL and Pa4836 (red): nicotinamine synthase. CntM and Pa4835 (blue): opine dehydrogenase. CntK: histidine racemase (white). CntA-F and Pa4837: import proteins (dark gray). CntE and Pa4834: export proteins (light gray).

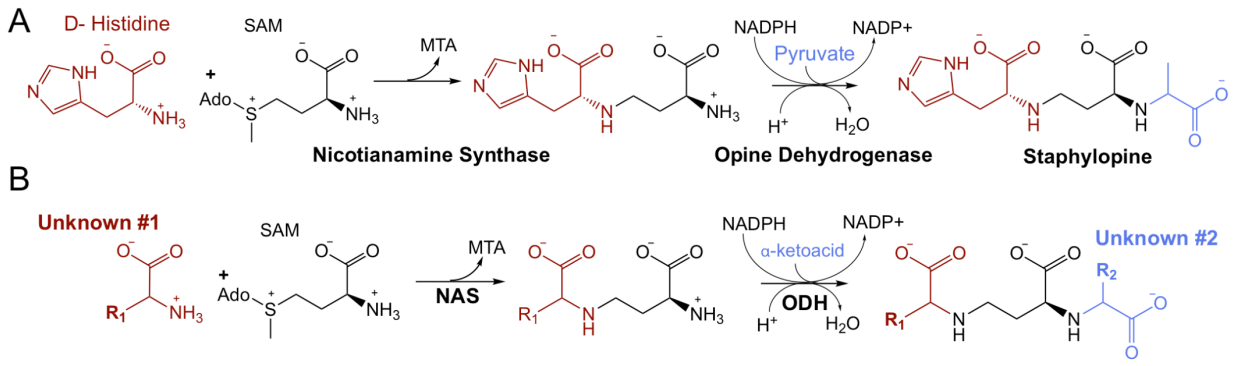

Figure 2-2. A) Staphylopine biosynthesis. (SAM is *S*-adenosyl-L-methionine, MTA is methylthioadenosine, and Ado is adenosine) **B) Pseudopaline biosynthesis hypothesis.**

energy source for the bacterial pathogen[4]. ODHs have also been described in marine molluscs, such as *Arctica islandica* (king scallop), where they catalyze the reductive condensation of an opine product from pyruvate and L-arginine[5]. This reaction regenerates NAD^+ in muscle tissue allowing glycolysis to continue under anaerobic conditions. In *S. aureus*, ODH uses the primary amine of the D-histidine-aminobutyrate product of NAS as a nucleophile in a condensation with pyruvate followed by hydride transfer from NADPH. Together, these three enzymes biosynthesize the opine metallophore staphylopine (**Figure 2-2A**).

The four-gene operon in *P. aeruginosa* encodes Pa4837, predicted to be an outer membrane TonB-dependent receptor, and Pa4834, predicted to be an EamA-like export transporter[6]. Notably, genes encoding inner membrane import function and outer membrane export function are absent suggesting that they are encoded elsewhere and/or may be shared with another pathway. This operon is also predicted to encode a NAS and ODH sharing 24% and 30% identity respectively with *S. aureus* as determined by Clustal Omega[7]. Further, both the *S. aureus* and *P. aeruginosa* NAS enzymes have active site residues conserved with the *M. thermautotrophicus* NAS[8] and both ODHs have GXGXXG/A NAD(P)H binding motifs. The entire operon is upregulated in *P. aeruginosa* clinical isolates from human burn wound and cystic fibrosis lung infections[9, 10] as well as in an airway mucus secretion growth model[1]. Further, transport mutants (Δ*Pa4834*) show significantly attenuated growth in murine airway and burn wound infection models[1]. Taken together, these data suggest that *P. aeruginosa* may be producing a metallophore similar to staphylopine and that this metallophore plays an important role in pathogenesis, surprising given the expanse of evolution separating the two species. We hypothesized that PaNAS would produce a nicotianamine product using SAM exclusively or in concert with an amino acid substrate (**unknown #1, Figure 2-2B**) and that PaODH would act on the NAS product by incorporating an α-keto acid (**unknown #2, Figure 2-2B**).

Materials and Methods

Protein Expression and Purification

Gene sequences for the *P. aeruginosa* PAO1 strain nicotianamine synthase (NAS) (PA4836) and opine dehydrogenase (ODH) (PA4835) were acquired from the *Pseudomonas* Genome Database[6]. Sequences for *S. aureus* were acquired from the methicillin-resistant Mu50 strain with NCBI accession numbers WP_001058848.1 (NAS) and WP_000040588.1 (ODH). These sequences were codon optimized for expression in *E. coli* by GenScript. The *P. aeruginosa* sequences were ligated into pET28b vectors and the *S. aureus* sequences were ligated into pET15TV-L vectors, both with N-terminal hexahistidine tags. The plasmids were transformed into New England Biolabs BL21 (DE3) cells for expression.

Following growth of a 50 mL overnight culture at 37 °C, baffled flasks with 1L of LB media containing 50 mg/mL kanamycin (pET28b) or 200 mg/mL ampicillin (pET15TV-L) were inoculated with 10 mL of overnight culture and grown to an O.D. of 0.6 at 37 °C. Cultures were induced with 200 µL of 1 M IPTG and grown overnight at their optimal expression temperature (25 °C for PaNAS, PaODH and SaODH and 15 °C for SaNAS). After 20 hours, cells were pelleted at 4225 x g for 10 minutes. The resulting pellet was resuspended in buffer A containing 50 mM potassium phosphate pH 8, 300 mM NaCl, 50 mM imidazole and 10% glycerol. Cells were French pressed 3 times and the lysate was centrifuged 1 hour at 23,426 x g. The lysate was loaded onto a GE Healthcare nickel-chelating fast flow sepharose column. NAS proteins were eluted using a linear gradient of increasing imidazole concentration up to 500 mM. Both NAS proteins elute with a peak at approximately 275 mM. The ODHs were purified using a step gradient of 500 mM imidazole, with steps of 20% to wash out contaminating protein and 55% to elute ODH. Eluted samples were loaded directly onto a GE Superdex 200 size exclusion chromatography column pre-equilibrated with 50 mM potassium phosphate pH 8, 150 mM sodium citrate and 20% glycerol for PaNAS, PaODH and SaODH. For SaNAS, 50 mM potassium phosphate pH 8, 100 mM sodium chloride and 10% glycerol was used as the size exclusion chromatography buffer. Following purification, protein was concentrated using Millipore Amicon centrifugation concentrators with 10,000 MWCO (NAS) or 30,000 MWCO (ODH), to final concentrations of 10-12 mg/mL. These preparations yield

20 mg (PaODH), 80 mg (SaODH), 100 mg (PaNAS) and 150 mg (SaNAS) per liter of culture. Purity of each protein was evaluated using 15% Tris-HCl SDS-PAGE. All were greater than 95% pure.

***P. aeruginosa* NAS binding affinity for SAM**

To determine the binding affinity of PaNAS for *S*-adenosyl-L-methionine (SAM), a Cary Eclipse fluorometer was set to an excitation wavelength of 280 nm and an emission wavelength of 380 nm with excitation and emission slits set to 20 nm. 100 nM PaNAS in 50 mM potassium phosphate pH 8 was added to a quartz fluorometry cuvette to give a total volume of 100 µL. Increasing concentrations of SAM were titrated from 0 - 25 µM after correcting for dilution. Each concentration was measured three times per experiment and each experiment was repeated three times.

Raw data showed a decrease in fluorescence of 50 AU while titrating from 0 to 15 µM SAM. Fluorescence intensities were corrected for the inner filter effect due to SAM absorbance at 280 nm using the equation[11]:

$$Fc = F \times 10^{\frac{\varepsilon C l}{2}}$$

where F is the measured fluorescence intensity, ε is the extinction coefficient of SAM measured at 280 nm and calculated using Beer's law, C is the concentration of SAM in M and *l* is the cuvette path length in cm^{-1}. The Stern-Volmer equation:

$$\frac{Fo}{Fc} = 1 + K_D[Q]$$

was initially used for K_D determination due to the observed red shifted emission spectrum for PaNAS, however a graph of Fo/F vs. [SAM] produced a line with downward curvature suggesting a difference in quenching between the two tryptophans in the protein[12]. The modified Stern-Volmer equation

$$\frac{Fo}{Fo-Fc} = \frac{1}{(f_a K_Q[Q])} + \frac{1}{f_a}$$

was then used to correct for this effect[11, 12]. f_a is the fractional number of fluorophores accessible to the quencher and [Q] is the concentration of quencher. Fo/(Fo-Fc) vs. 1/[Q] gave a straight line plot where the slope = $1/K_Q = K_D$ and the y-intercept = f_a. The change in fluorescence intensity was also plotted vs. [SAM]. The resulting curve was fit using the equation:

$$\frac{-\Delta Fc}{F} = \frac{[SAM]}{[SAM] + K_D}$$

where F is the maximal fluorescence change upon binding and K_D is the dissociation constant for SAM.

***P. aeruginosa* ODH binding affinity for NADPH**

To determine the binding affinity of NADPH for PaODH, a Cary Eclipse fluorometer was set to an excitation wavelength of 340 nm and an emission wavelength of 450 nm with excitation and emission slits set to 10 nm. NADPH in 50 mM potassium phosphate pH 8 was added to a quartz fluorometry cuvette to yield 100 µL of total volume with an NADPH concentration of 250 nM. PaODH was titrated in increasing concentrations from 0.2 - 25 µM after correction for dilution. Each concentration was measured three times for each experiment and each experiment was repeated three times. To correct for the inner filter effect caused by increasing concentrations of protein, the fluorescence for each PaODH concentration was measured in the absence of NADPH. A plot of the change in fluorescence vs. enzyme concentration fit to a straight line which was subtracted from the titrations with NADPH present. The resulting fluorescence values were fit to the equation below:

$$\Delta F = \frac{F \times [NADPH]}{[NADPH] + K_D}$$

Reconstitution of biosynthetic pathway (plate-reader assay)

To assay different combinations of potential amino acid and α-ketoacid substrates, an assay combining both biosynthetic enzymes was developed that monitored the oxidation of NADPH to $NADP^+$ by ODH as a loss of absorbance at 340 nm. Experiments were performed

using a Cary Eclipse spectrophotometer paired with a Cary 50MPR microplate reader using Costar 96 well flat-bottomed plates. Immediately prior to each experiment, a master mix of 2 μM NAS, 2 μM ODH, 200 μM SAM and 75 μM NADPH in 50 mM Tris pH 8 (*S. aureus*) or 50 mM potassium phosphate pH 8 (*P. aeruginosa*) was made. This master mix also contained 200 μM of either pyruvate, oxalaoacetate or 2-ketoglutarate. The master mix was dispensed into each of 24 wells and rocked gently for 30 seconds to mix. 2 μL of test amino acid solution was added to independent wells to a final concentration of 200 μM to initiate the reaction. Each amino acid was tested in triplicate wells. Absorbance readings at 340 nm were immediately initiated and recorded for 20 minutes at room temperature. To determine the rate of conversion of NADPH to $NADP^+$, a standard curve was generated for the absorbance by NADPH in the 96 well plate. This resulted in a linear plot. The equation calculated from the linear fit was used to convert absorbance values to NADPH concentrations. The 42 amino acids tested are shown in **Table 2-1.** To determine the specificity of SaODH for pyruvate, oxaloacetate or α-ketoglutarate the assay above was repeated with 2 μM SaNAS, 2 μM SaODH, 500 μM SAM, 75 μM NADPH, 2 mM α-ketoacid and 2 mM D-histidine in 50 mM Tris pH 8. These experiments were repeated three times on separate days. These conditions were also used to compare ketoacid substrate specificity for PaODH. Oxaloacetate is known to decompose to pyruvate over time[13]. To prevent this process from contributing to the reaction rate for the *S. aureus* enzymes, oxaloacetate was solubilized immediately prior to its addition to the reaction mixture. To confirm that pyruvate was not present in the oxaloacetate solution, we performed ^{13}C-NMR on a pyruvate standard and on an oxaloacetate sample. The resulting NMR spectrum showed no evidence of contaminating pyruvate in the oxaloacetate samples brought into solution and scanned for 20 minutes.

Progress curves to determine amino acid selectivity

To measure full progress curves, NADPH oxidation at 340 nm was recorded at 22 °C for 1 hour using a TgK stopped flow spectrometer with a xenon lamp. Final reaction concentrations following, 1:1 mixing of syringe one and two, were 2 μM NAS, 20 μM ODH, 400 μM SAM, 400 μM

Table 2-1. Compounds tested.

L-Amino Acids		**D-Amino Acids**	
L-2,4-Diaminobutyric	L-lysine	D-alanine	D-phenylalanine
L-alanine	L-methionine	D-arginine	D-proline
L-arginine	L-norleucine	D-asparagine	D-serine
L-asparagine	L-norvaline	D-aspartic acid	D-tryptophan
L-aspartic Acid	L-ornithine	D-glutamic acid	D-tyrosine
L-cysteine	L-phenylalanine	D-glutamine	D-valine
L-glutamic Acid	L-proline	D-histidine	
L-glutamine	L-serine	D-leucine	**2-Keto acids**
L-histidine	L-threonine	D-lysine	pyruvate
L-hydroxy-Proline	L-tryptophan	D-methionine	oxaloacetate
L-isoleucine	L-tyrosine	D-norleucine	α-ketoglutarate
L-leucine	L-valine	D-ornithine	

α-ketoacid (PaODH - α-ketoglutarate, SaODH - pyruvate), 200 μM NADPH and 25 μM or 12.5 μM histidine (PaODH - L-histidine, SaODH - D-histidine) combined in 50 mM pH 8 buffer (Pa - KP_i, Sa - Tris). Syringe 1 contained the above components except for histidine. Syringe 2 contained histidine in 50 mM pH 8 buffer (Pa - KP_i, Sa - Tris). Each reaction was performed twice and the resulting curves averaged.

Initial rate reactions to determine steady state kinetic parameters

NADPH oxidation at 340 nm was recorded at 22 °C using a TgK stopped flow spectrometer with a xenon lamp. Syringe one contained 2 μM NAS, 20 μM ODH, 1200 μM SAM, 400 μM NADPH, and 2000 μM pyruvate in 50 mM pH 8 buffer (Pa - KP_i, Sa - Tris). The non-rate-limiting concentration of all susbtrates was determined by comparing full progress curves as described above for varied concentrations of substrates and ODH enzyme. Syringe two contained L-histidine (PaNAS) or D-histidine (SaNAS) at decreasing concentrations following a two-fold serial dilution of histidine from a starting concentration of 800 μM down to 0.78 μM in the same buffer used in syringe one. The two syringes were mixed 1:1 and initial rates were recorded for 60 seconds and the concentration series was measured four times for each enzyme. Secondary plots of initial rates were fit as described below. The secondary plot of PaNAS was fit to the quadratic form of the velocity equation[14] to account for the high concentration of enzyme (1 μM) relative to the K_m (5.4 μM):

$$V_o = V_{max}\frac{([E_T] + [S_T] + [K_m]) - \sqrt{([E_T] + [S_T] + [K_m])^2 - 4[E_T][S_T]}}{2[E_T]}$$

The secondary plot of the SaNAS reaction with D-histidine was fit using the Michaelis-Menten equation:

$$V_o = \frac{V_{max}[S]}{K_m + [S]}$$

Mass spectrometry verification of pseudopaline and staphylopine production

Pseudopaline was produced by combining 10 μM PaNAS, 10 μM PaODH, 5 mM NADPH, 5 mM SAM, 5 mM L-histidine, and 5 mM α-ketoglutarate in 50 mM potassium phosphate pH 8. The total reaction volume was 1.5 mL and was incubated at room temperature for 2 hours while slowly rocking. After 2 hours the reaction was quenched and the protein precipitated by adding glacial acetic acid to a final concentration of 300 μM. Precipitated protein was pelleted by centrifugation for 10 min at 20,800 x g. The supernatant was removed and submitted for ESI-MS analysis. An Agilent quadrupole G6120A coupled to an Agilent 1200 HPLC using a Waters T3 C-18 column were used for sample separation and analysis. We predicted a mass for pseudopaline following acid quench of 386.1438 ($[M+H]^+$ of 387.1438). A product *m/z* of 387.15 was detected in positive mode from the first elution peak of the solvent front using a mobile phase of 99% Water (0.05% Formic Acid): 1% MeOH. This elution peak was also found to contain L-histidine (*m/z* 156.08). A high resolution mass spectrum (HRMS) was performed on a Waters LCT Premiere (Micromass, Ltd., Manchester UK) time of flight mass spectrometer with an electrospray ion source and determined to be *m/z* 387.1526 consistent with $[M+H]^+$ for pseudopaline. We predicted a mass for the NAS reaction product of *m/z* $[M+H]^+$ 258.12. At 1.51 min, a peak eluted with an *m/z* of 258.04 which we assume to be a small quantity of unconsumed NAS reaction product. We also performed a direct ESI-MS injection of supernatant from a separate reaction performed as described above. These samples were diluted 100-fold with LC-MS grade water (Sigma-Aldrich), and 10uL of each dilution was analyzed by flow injection over 2 minutes on an LCMS-IT-TOF (Shimadzu Scientific Instruments). Solvent conditions for injection were 60% of an aqueous 0.2% formic acid solution and 40% acetonitrile (Sigma Aldrich), with a total flow rate of 0.3 mL/min. An ESI source was used, and acquisition was performed in scan mode from 100-750 m/z for both positive- and negative ion modes. A 10 msec ion accumulation time was used, and event time was set to 100 msec. Using this technique, we again identified an *m/z* of 387.149 corresponding to the presence of pseudopaline. Staphylopine was produced by combining 10 μM SaNAS, 10 μM SaODH, 5 mM NADPH, 5 mM SAM, 5 mM D-histidine, and 5 mM pyruvate in 50

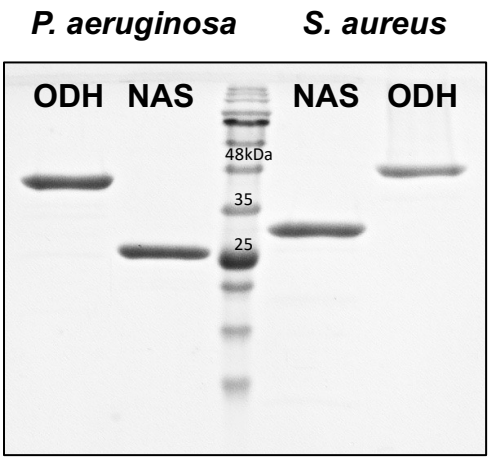

Figure 2-3. SDS PAGE analysis of purified proteins. Lanes: *P. aeruginosa* NAS and ODH and the *S. aureus* NAS and ODH. The ladder is a GOLDBIO BLUEstain protein ladder and the gel is 15% Tris-HCl.

mM potassium phosphate pH 8. Following a two hour incubation at room temperature, supernatants were prepared and mass spectrometry analysis was performed as described above for pseudopaline. A product *m/z* of 329.1441 was detected in positive mode from the first elution peak (0.33 min) of the solvent front using a mobile phase of 99% Water (0.05% Formic Acid): 1% MeOH. Staphylopine was also detected following direct injection of supernatants with an *m/z* of 329.143. These values correspond to the expected mass for staphylopine as first reported by Ghssein et al[2].

Results and Discussion

To test the hypothesis that the *P. aeruginosa* NAS and ODH also produce a metallophore product, the *P. aeruginosa* and *S. aureus* nicotianamine synthase (PaNAS and SaNAS) and opine dehydrogenase (PaODH and SaODH) enzymes were heterologously expressed and purified (**Figure 2-3**).

The affinity of PaNAS for SAM was measured by intrinsic tryptophan fluorescence while titrating SAM. The resulting dissociation constant was 1.2 ± 0.3 μM which is 57-fold tighter than the 68 μM value previously reported for SaNAS[2] (**Figure 2-4A**). The affinity of PaODH for NADPH was determined by measuring an increase in NADPH fluorescence, as enzyme was titrated. The resulting dissociation constant was 11 ± 1 μM, five-fold tighter than the 50 μM value reported for SaODH[2] (**Figure 2-4B**). A dissociation constant for NADH could not be determined in the concentration range used in this method, indicating a lower affinity of PaODH for NADH. These results confirm that PaNAS binds SAM and PaODH binds NADPH.

To identify the unknown *P. aeruginosa* NAS and ODH substrates, we reconstituted the biosynthetic pathway *in vitro* using purified protein. We expected to observe a decrease in absorbance at 340 nm as the NADPH was oxidized to $NADP^+$ by the PaODH in the presence of PaNAS, SAM, and the correct amino acid and α-keto acid substrates. Pyruvate, oxaloacetate and α-ketoglutarate were screened with SAM, but no oxidation was observed suggesting that SAM

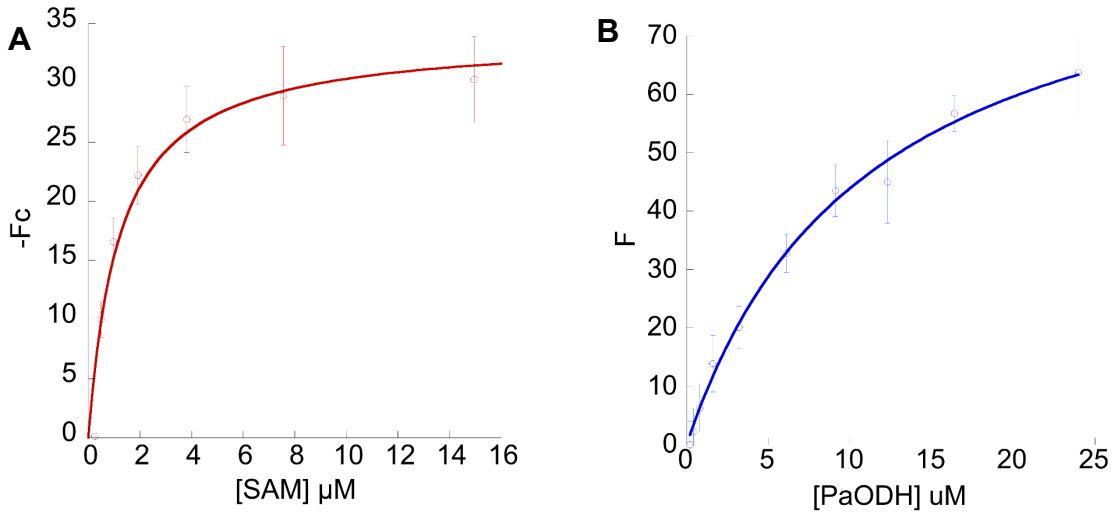

Figure 2-4. Binding isotherms. A) Fitted plot of decreasing PaNAS fluorescence vs. [SAM]. The resulting K_D is 1.2 ± 0.3 μM. **B)** Affinity of *P. aeruginosa* opine dehydrogenase for NADPH . The NADPH was excited at 340 nm and emission was measured at 450 nm. The resulting K_D was 11 ± 1 μM. Error is the standard deviation of three trials.

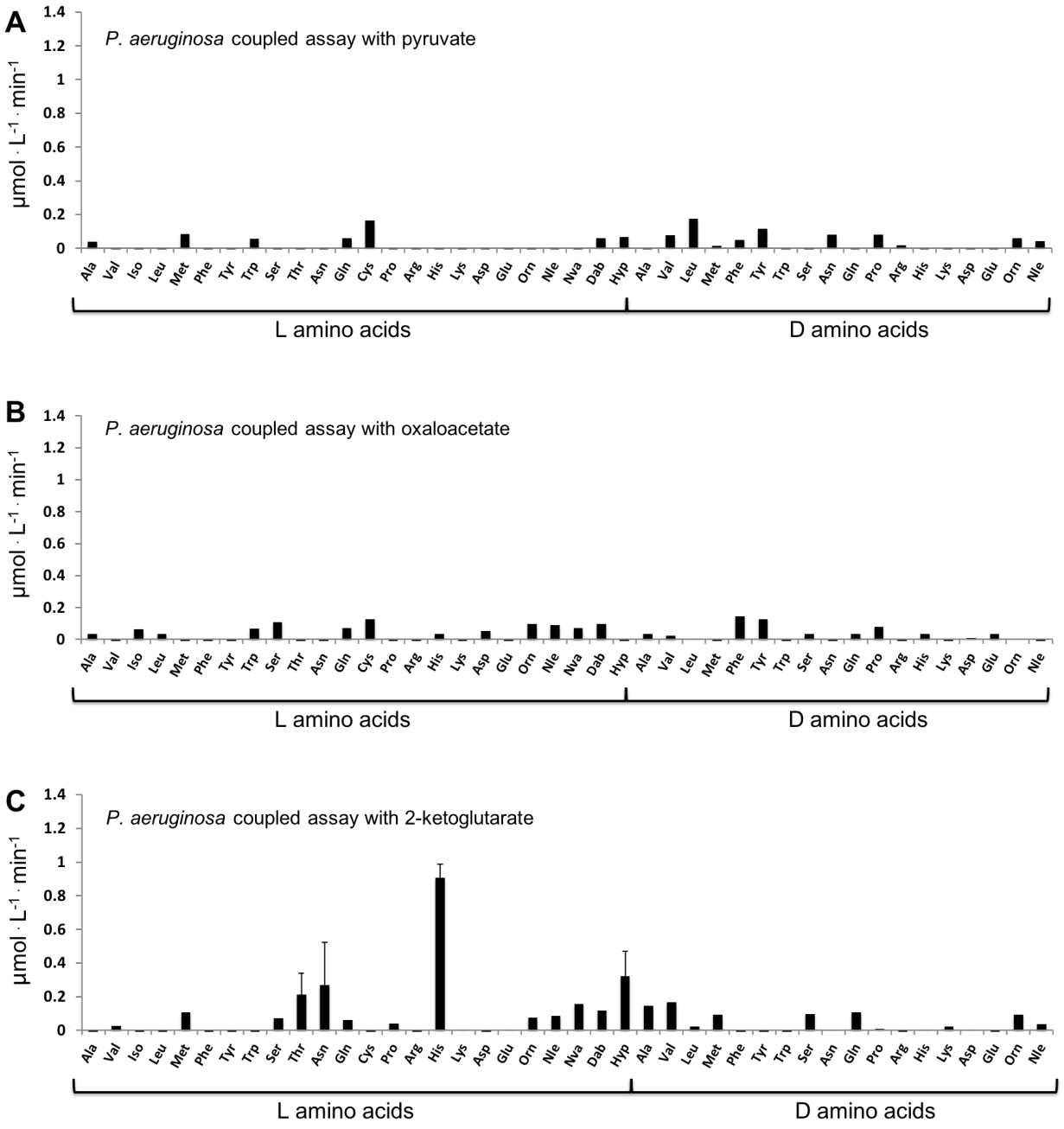

Figure 2-5. Reconstitution of *P. aeruginosa* biosynthetic pathways to determine amino acid specificity. Each error bar represents the standard deviation of three trials. Rates were determined using an NADPH standard curve and calculated in µmol · L^{-1} · min^{-1}. The non-standard abbreviations are as follows: Orn - ornithine, Nle - norleucine, Nva - norvaline, Dab - 2,4-diaminobutyric acid, Hyp - hydroxyproline **A)** *P. aeruginosa* activity in the presence of pyruvate

with varied amino acids. **B)** *P. aeruginosa* activity in the presence of oxaloacetate with varied amino acids. **C)** *P. aeruginosa* activity in the presence of 2-ketoglutarate with varied amino acids.

alone is not sufficient as a substrate for PaNAS. We screened 42 L- and D-amino acid substrates in combination with pyruvate, oxaloacetate or α-ketoglutarate. Several amino acids, L-threonine, L-asparagine and L-hydroxyproline (L-hyp), appeared to show limited turnover in this screen, while the combination of L-histidine and α-ketoglutarate resulted in significant oxidation of NADPH by PaODH (**Figure 2-5**).

To confirm PaNAS catalysis with L-histidine and α-ketoglutarate we measured full progress curves on a TgK stopped flow spectrometer. Using this more sensitive method, catalysis was observed only for L-histidine, indicating that the limited NADPH oxidation measured for L-Thr, L-Asn and L-Hyp in our amino acid screening was the result of variance in our plate reader measurements (**Figure 2-6A**). Steady state kinetic parameters for the PaNAS reaction with L-histidine were determined by fitting the Michealis-Menten equation to a secondary plot of initial rates measured by stopped flow spectrometry at varying L-histidine concentrations. Using this fit we determined a k_{cat} of 1.07 ± 0.02 min^{-1}, K_m of 5.4 ± 0.4 μM and k_{cat}/K_m of 3400 ± 200 $M^{-1}s^{-1}$ (**Figure 2-6C**). These results demonstrate that PaNAS is specific for L-histidine and that the *P. aeruginosa* biosynthetic pathway incorporates L-histidine, aminobutyrate and α-ketoglutarate to form an opine metallophore product (**Figure 2-6D**).

To confirm the mass of this product, we incubated the *P. aeruginosa* enzymes and substrates for two hours at room temperature and performed mass spectrometry, predicting that an opine product composed of one L-histidine, one aminobutyrate and one α-ketoglutarate would have a neutral mass of 386.14 Da. We considered the possibility that NAS could incorporate two aminobutyrate moieties as in *M. thermautotrophicus*[8] or three as in plant NAS enzymes[15]. This would result in neutral product masses of 487.20 and 588.25 Da. The product *m/z* species for the *P. aeruginosa* reaction had an $[M+H]^+$ HRMS *m/z* of 387.1529 (**Figure 2-7A-C**). Also observed was an *m/z* of 258.04 matching the $[M+H]^+$ for the NAS product (**Figure 2-7D**). No *m/z* matching

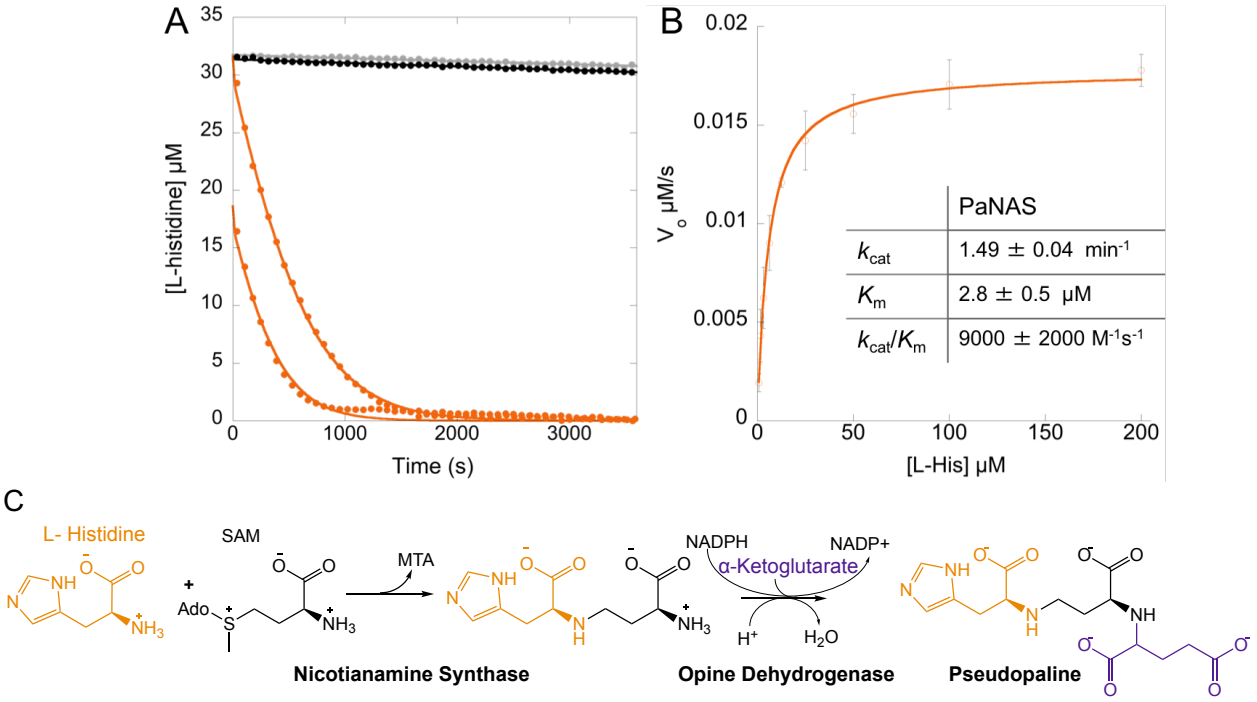

Figure 2-6. Pseudopaline biosynthesis A) *P. aeruginosa* NAS full progress curves. 0 µM amino acid (black), or 25 µM L-Thr, L-Asn, or L-Hyp (gray), or 25 µM (orange-top) or 12.5 µM L-histidine (orange-bottom) was combined with 2 µM PaNAS, 20 µM PaODH, 200 µM NADPH and 400 µM each of SAM and α-ketoglutarate in 50 mM KP_i pH 8 buffer. L-Thr and L-Asn are omitted for clarity as they overlay the 0 µM control. **B)** Secondary plots of initial rate experiments. PaNAS. Initial reaction rates measured as NADPH was oxidized by PaODH. L-histidine concentration was varied from 0.78 µM to 200 µM. Kinetic parameters determined by fitting the Michaelis-Menten equation to the secondary plot of initial rates. Error propagated based on the standard deviation of four trials. **C)** Pseudopaline biosynthesis.

A

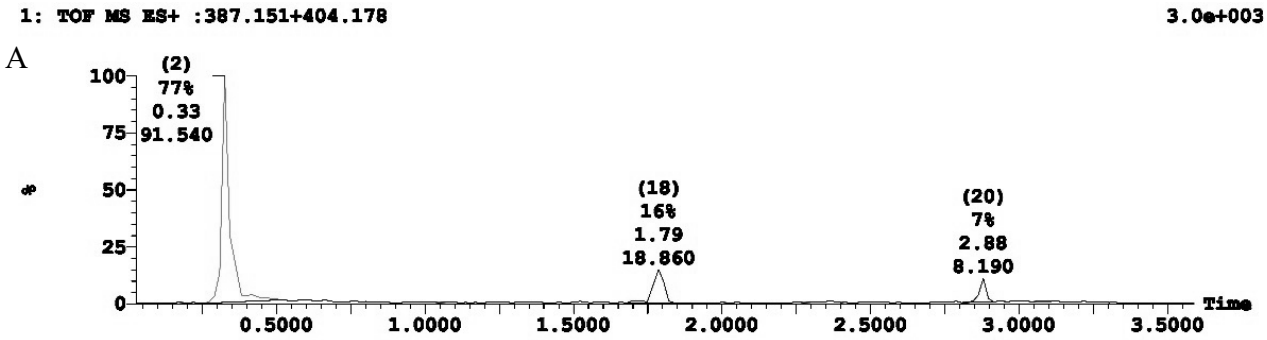
1: TOF MS ES+ :387.151+404.178
3.0e+003
(2)
77%
0.33
91.540
(18)
16%
1.79
18.860
(20)
7%
2.88
8.190
Time

B

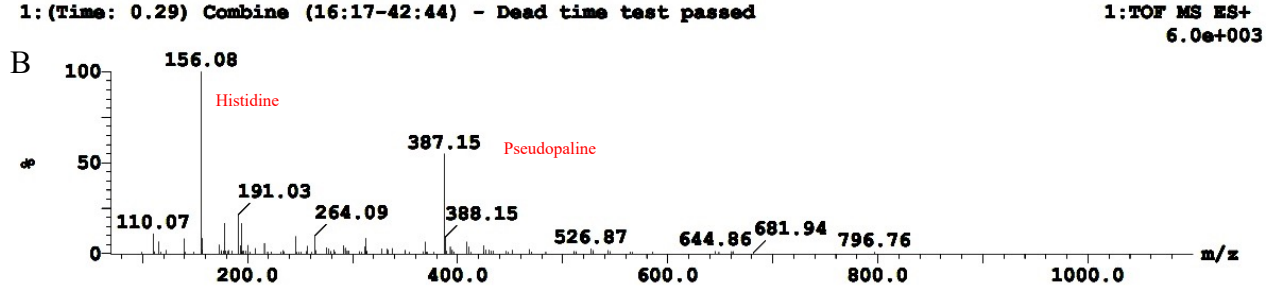
1:(Time: 0.29) Combine (16:17-42:44) - Dead time test passed
1:TOF MS ES+
6.0e+003
156.08
Histidine
387.15
Pseudopaline
191.03
110.07
264.09
388.15
526.87
644.86
681.94
796.76
m/z

C

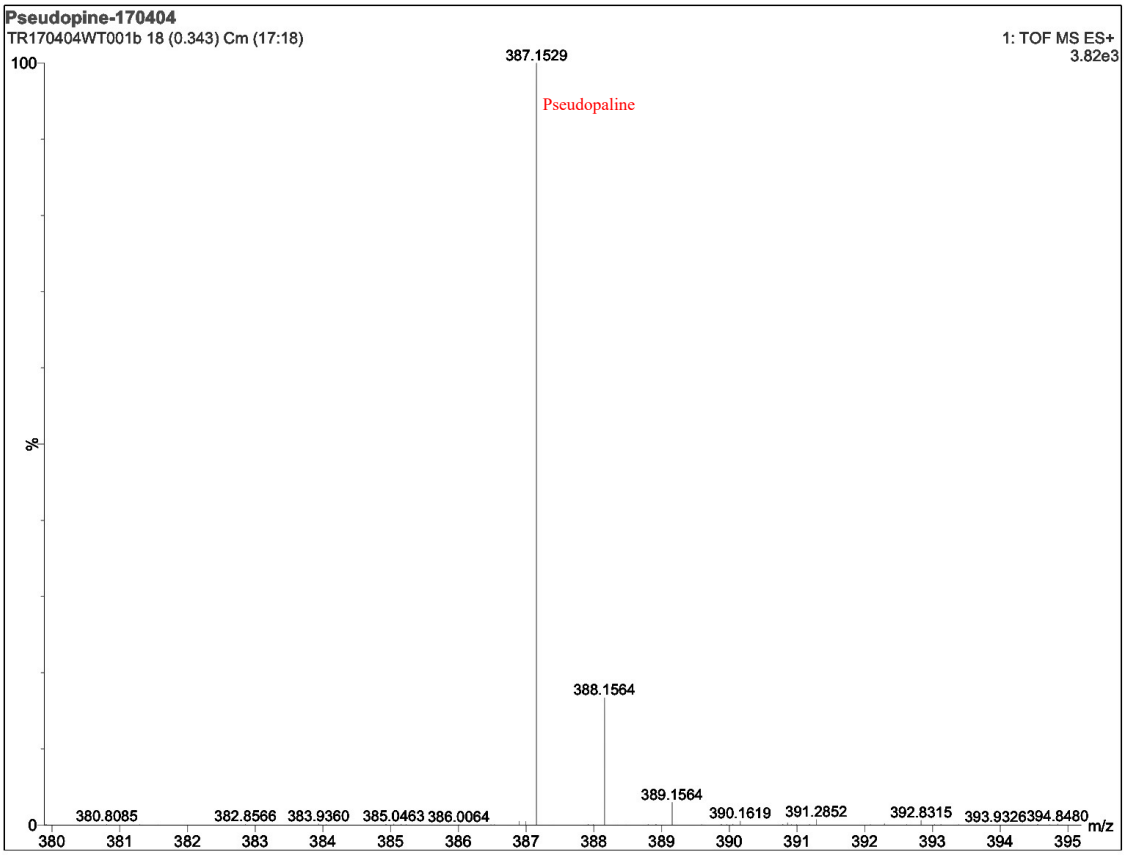
Pseudopine-170404
TR170404WT001b 18 (0.343) Cm (17:18)
1: TOF MS ES+
3.82e3
387.1529
Pseudopaline
388.1564
389.1564
380.8085
382.8566
383.9360
385.0463
386.0064
390.1619
391.2852
392.8315
393.9326
394.8480
m/z

D

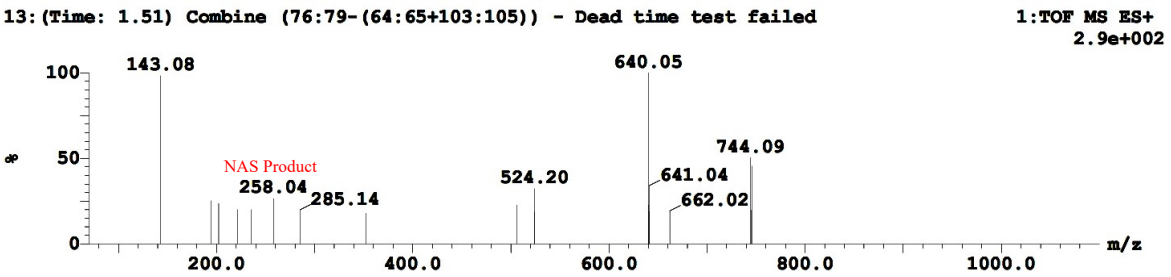

Figure 2-7. Pseudopaline mass spectrometry data. A) Extracted ion chromatogram for pseudopaline. The majority of pseudopaline eluted in the first peak at 0.33 min. **B)** ESI-MS spectrum for the 0.33 min elution peak showing pseudopaline. **C)** ESI-MS high resolution spectrum for pseudopaline from the 0.33 min elution peak. **D)** ESI-MS spectrum for the 1.51 min elution peak showing the NAS product.

products with 0, 2 or 3 aminobutyrates were observed leading us to propose an overall reaction scheme for the biosynthesis of a novel opine metallophore we name pseudopaline (**Figure 2-6C**).

As opine dehydrogenases use diverse amino acid and α-keto acid substrates, the substrate specificity of the *S. aureus* enzymes was examined. All 42 amino acids were tested in conjunction with pyruvate in the plate-reader screening assay. Only in the presence of D-histidine were we able to measure significant oxidation of NADPH (**Figure 2-8A**). This was confirmed by following a full progress curve of the reaction with D-histidine and pyruvate (**Figure 2-8B**). A secondary plot of SaNAS initial reaction rates measured by stopped flow spectrometry at varying concentrations of D-histidine allows us to determine a k_{cat} of 1.79 ± 0.02 min^{-1}, K_m of 13.0 ± 0.7 μM and k_{cat}/K_m of 2300 ± 100 $M^{-1}s^{-1}$ (**Figure 2-8C**).

As key intermediates in the citric acid cycle, we reasoned that oxaloacetate and α-ketoglutarate would be available for opine biosynthesis. Reactions with pyruvate and D-histidine resulted in a NADPH oxidation rate of 3.2 ± 0.3 $\mu mol \cdot L^{-1} \cdot min^{-1}$. In the presence of oxaloacetate the rate was 1.1 ± 0.2 $\mu mol \cdot L^{-1} \cdot min^{-1}$ and for α-ketoglutarate the rate was within error of zero (**Figure 2-9**). Catalysis with oxaloacetate suggests that *S. aureus* could be producing two staphylopine variants, one with pyruvate and an analog with oxaloacetate. However, the significantly lower initial rate with oxaloacetate may suggest that its incorporation is not physiologically relevant. While we can readily identify staphylopine with pyruvate incorporated by mass spectrometry (**Figure 2-10**), we have not identified an $[M+H]^+$ *m/z* corresponding to the production of the oxaloacetate variant.

Our results demonstrate that opine metallophores are not exclusive to the genus *Staphylococcus* but are also found in the widely diverged species *Pseudomonas aeruginosa*. Pseudopaline represents a third identified metallophore produced by *P. aeruginosa* in addition to the well characterized pyoverdin and pyochelin molecules. Pseudopaline and staphylopine incorporate an imidazole functional group from histidine with opposite stereochemistry.

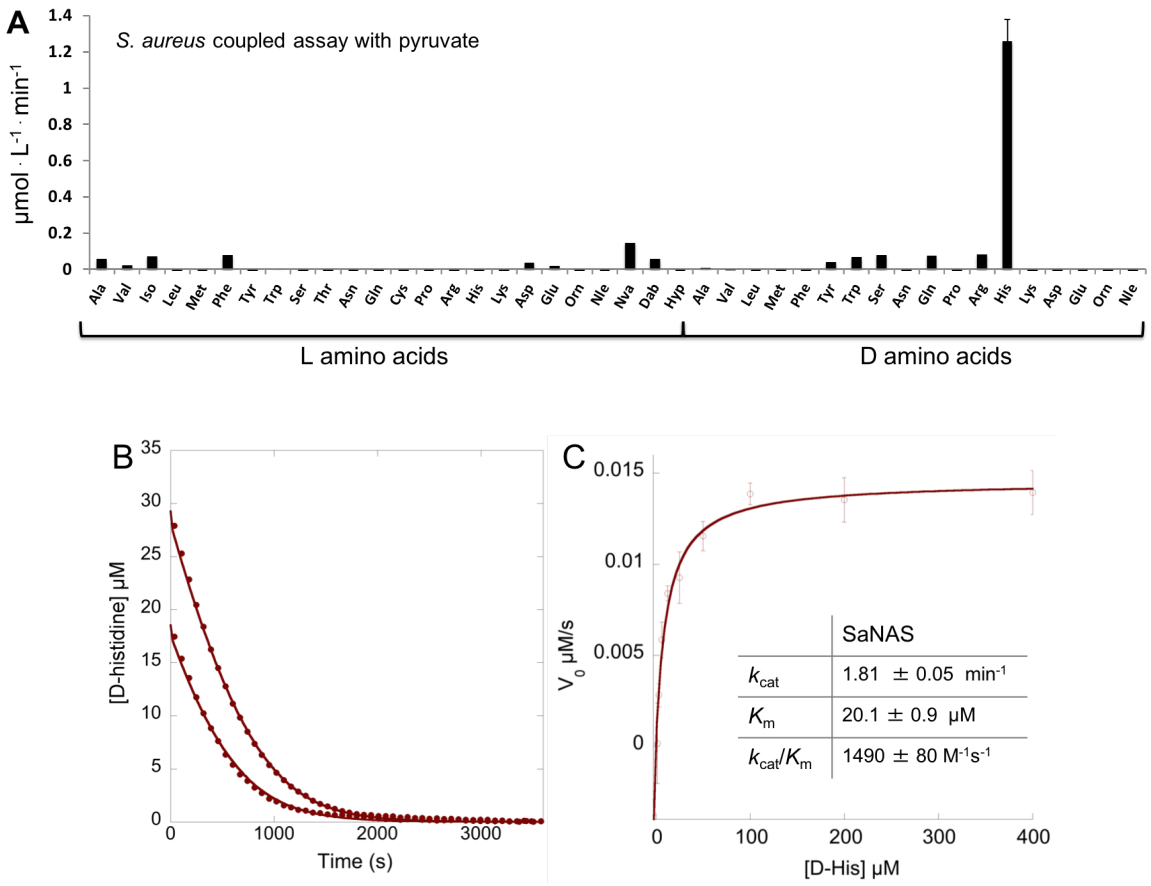

Figure 2-8. Reconstitution of *S. aureus* biosynthetic pathway to determine amino acid specificity and steady state kinetic parameters. Rates were determined using an NADPH standard curve and calculated in µmol · L^{-1} · min^{-1}. The non-standard abbreviations are as follows: Orn - ornithine, Nle - norleucine, Nva - norvaline, Dab - 2,4-diaminobutyric acid, Hyp - hydroxyproline **A)** *S. aureus* activity in the presence of pyruvate with varied amino acids. **B)** *S. aureus* NAS full progress curves. 25 µM (red-top) or 12.5 µM (red-bottom) D-histidine was combined with 2 µM SaNAS, 20 µM SaODH, 200 µM NADPH and 400 µM each of SAM and pyruvate in 50 mM Tris pH 8 buffer. **C)** Secondary plot of initial rate experiments. SaNAS. Initial reaction rates were measured as NADPH was oxidized by SaODH. D-histidine concentration was varied from 0.78 µM to 400 µM. Kinetic parameters determined by fitting the Michaelis-Menten equation to the secondary plot of initial rates. Error propagated based on the standard deviation of at least three trials.

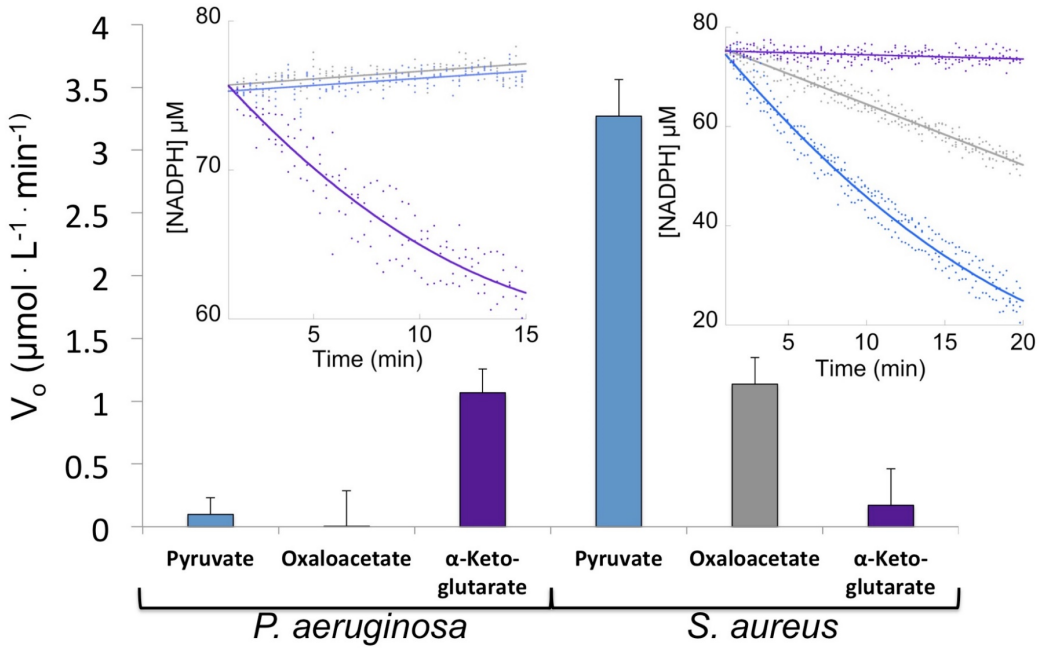

Figure 2-9. Opine dehydrogenase substrate specificity. Initial reaction rates by PaODH (left) and SaODH (right) with pyruvate, oxaloacetate or α-ketoglutarate. Rates were derived from the inset data (left - PaODH, right - SaODH). *P. aeruginosa* reactions used L-his while *S. aureus* reactions used D-his. 2 μM enzyme, 75 μM of NADPH, 500 μM SAM, 2 mM each of histidine and α-keto acid were combined in 50 mM KP_i (Pa) or Tris (Sa) pH 8 buffer.

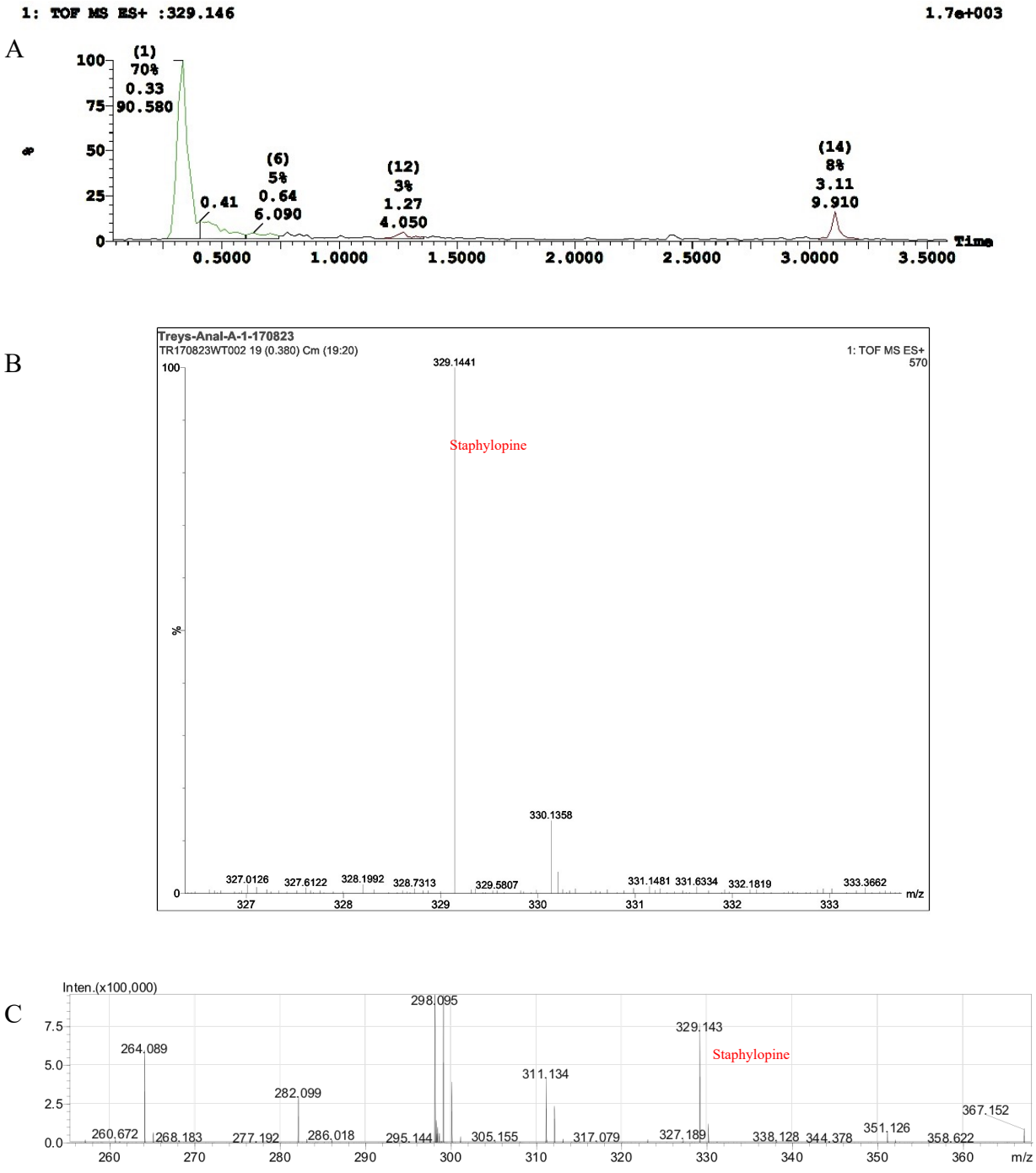

Figure 2-10. Staphylopine mass spectrometry data. A) Extracted ion chromatogram for staphylopine. The majority of staphylopine eluted in the first peak at 0.33 min. **B)** ESI-MS high resolution spectrum for staphylopine from the 0.33 min elution peak. **C)** ESI-MS spectrum for staphylopine following direct injection of supernatants.

Additionally, pseudopaline incorporates α-ketoglutarate into the metallophore scaffold, which is bulkier and contains an extra carboxyl group compared to the pyruvate-derived metallophore found in staphylopine, providing additional flexibility and potentially increased metal affinity. The *S. aureus* opine dehydrogenase catalytic activity with α-ketoglutarate is within error of zero, but SaODH accepts oxalaoacetate, also containing an additional carboxylate group, as a substrate alternative at 35% the steady-state rate of pyruvate (**Figure 2-9**). Conversely, *P. aeruginosa* shows no catalytic activity in the presence of pyruvate or oxaloacetate (within error of zero), but full activity with α-ketoglutarate (**Figure 2-9**).

The functional role of opine metallophores is not well established, but is associated with virulence in *S. aureus* and *P. aeruginosa*. Homologus operons are found in *Serratia marcescens* (WW4) and *Yersenia pestis* (CO92) suggesting that opine metallophores are produced by these pathogens. Gi et. al predicted the presence of NAS in the *P. aeruginosa* operon[1]. Their work demonstrates that the operon is involved in iron uptake during growth in culture derived airway mucus. This is significant as previous work has addressed iron uptake by pyoverdin and pyochelin, but the production of pseudopaline by *P. aeruginosa* must now also be considered in model systems. Staphylopine is involved in nickel and cobalt acquisition, but also takes up iron in metal-limited media[2]. The conservation of the histidine moiety in pseudopaline suggests a potential role in nickel and cobalt uptake in *P. aeruginosa* given the established role of histidine-dependent nickel transport by *S. aureus* NikA and staphylopine-dependent nickel and cobalt transport by CntA[16]. The role of trace elements in pathogenesis, such as nickel and cobalt, has received less scrutiny than for iron. However, urease, a nickel-dependent enzyme, is an established virulence factor in *S. aureus* where it is expressed in 90% of methicillin resistant strains[17]. Urease is also produced by *P. aeruginosa*[18]. Cobalt is required for the *P. aeruginosa* cobalamin-dependent ribonucleotide reductase (NrdJab), which is necessary for biofilm development under oxygen limited conditions[19]. While the presence of pseudopaline in *P.*

aeruginosa cultures will still need to be established to confirm production in vivo, these findings point to the importance of nickel and cobalt uptake in pathogenesis, suggesting a potential role for pseudopaline in the transport of these trace metals.

This work establishes the existence of an opine metallophore biosynthetic pathway in a second major pathogen, *P. aeruginosa*, and proposes the structure of the small molecule, pseudopaline. The characterization of the enzymes, nicotianamine synthase and opine dehydrogenase, reveals the recognition of amino acid substrates with opposite stereochemistry by the SaNAS and PaNAS, and the incorporation of different α-keto acids, pyruvate and oxaloacetate by SaODH and α-ketoglutarate by PaODH.

References

[1] Gi, M., Lee, K. M., Kim, S. C., Yoon, J. H., Yoon, S. S., and Choi, J. Y. (2015) A novel siderophore system is essential for the growth of Pseudomonas aeruginosa in airway mucus, *Sci Rep 5*, 1-15.

[2] Ghssein, G., Brutesco, C., Ouerdane, L., Fojcik, C., Izaute, A., Wang, S. L., Hajjar, C., Lobinski, R., Lemaire, D., Richaud, P., Voulhoux, R., Espaillat, A., Cava, F., Pignol, D., Borezee-Durant, E., and Arnoux, P. (2016) Biosynthesis of a broad-spectrum nicotianamine-like metallophore in Staphylococcus aureus, *Science 352*, 1105-1109.

[3] Wu, H., Min, J., Ikeguchi, Y., Zeng, H., Dong, A., Loppnau, P., Pegg, A. E., and Plotnikov, A. N. (2007) Structure and mechanim of spermidine synthases, *Biochemistry 46*, 8331-8339.

[4] Moore, L. W., Chilton, W. S., and Canfield, M. L. (1997) Diversity of Opines and Opine-Catabolizing Bacteria Isolated from Naturally Occurring Crown Gall Tumors, *Appl Environ Microbiol 63*, 201-207.

[5] Strahl, J., Dringen, R., Schmidt, M. M., Hardenberg, S., and Abele, D. (2011) Metabolic and physiological responses in tissues of the long-lived bivalve Arctica islandica to oxygen deficiency, *Comp Biochem Physiol A Mol Integr Physiol 158*, 513-519.

[6] Winsor, G. L., Griffiths, E. J., Lo, R., Dhillon, B. K., Shay, J. A., and Brinkman, F. S. (2016) Enhanced annotations and features for comparing thousands of Pseudomonas genomes in the Pseudomonas genome database, *Nucleic Acids Res 44*, D646-653.

[7] Sievers, F., Wilm, A., Dineen, D., Gibson, T. J., Karplus, K., Li, W., Lopez, R., McWilliam, H., Remmert, M., Soding, J., Thompson, J. D., and Higgins, D. G. (2011) Fast, scalable generation of high-quality protein multiple sequence alignments using Clustal Omega, *Mol Syst Biol 7*, 1-6.

[8] Dreyfus, C., Lemaire, D., Mari, S., Pignol, D., and Arnoux, P. (2009) Crystallographic snapshots of iterative substrate translocations during nicotianamine synthesis in Archaea, *Proc Natl Acad Sci U S A 106*, 16180-16184.

[9] Bielecki, P., Komor, U., Bielecka, A., Musken, M., Puchalka, J., Pletz, M. W., Ballmann, M., Martins dos Santos, V. A., Weiss, S., and Haussler, S. (2013) Ex vivo transcriptional profiling reveals a common set of genes important for the adaptation of Pseudomonas aeruginosa to chronically infected host sites, *Environ Microbiol 15*, 570-587.

[10] Bielecki, P., Puchalka, J., Wos-Oxley, M. L., Loessner, H., Glik, J., Kawecki, M., Nowak, M., Tummler, B., Weiss, S., and dos Santos, V. A. (2011) In-vivo expression profiling of Pseudomonas aeruginosa infections reveals niche-specific and strain-independent transcriptional programs, *PLoS One 6*, e24235.

[11] Maegley, K. A., Gonzalez, L., Smith, D. W., and Reich, N. O. (1992) Cofactor and DNA Interactions in *Eco*RI DNA Methyltransferase, *Journal of Biological Chemistry 267*, 6.

[12] Lakowicz, J. R. (2006) *Principles of Fluorescence Spectroscopy*, 3rd ed., Springer, New York.

[13] Buldain, G., Santos, C. d. l., and Frydman, B. (1985) Carbon-13 Nuclear Magnetic Resonance Spectra of the Hydrate, Keto and Enol forms of Oxalacetic Acid, *Magnetic Resonance in Chemistry 23*, 4.

[14] Morrison, J. F. (1969) Kinetics of the reversible inhibition of enzyme-catalyzed reactions by tight-binding inhibitors, *Biochim Biophys Acta 185*, 269-286.

[15] Shojima, S., Nishizawa, N., Fushiya, S., Nozoe, S., Irifune, T., and Mori, S. (1990) Biosynthesis of Phytosiderophores, *Plant Physiol 93*, 1497-1503.

[16] Lebrette, H., Borezee-Durant, E., Martin, L., Richaud, P., Boeri Erba, E., and Cavazza, C. (2015) Novel insights into nickel import in Staphylococcus aureus: the positive role of free histidine and structural characterization of a new thiazolidine-type nickel chelator, *Metallomics 7*, 613-621.

[17] Konieczna, I., Zarnowiec, P., Kwinkowski, M., Kolesinska, B., Fraczyk , J., Kaminski, Z., and Kaca, W. (2012) Bacterial Urease and its Role in Long-Lasting Human Disease, *Current Protein and Peptide Science 13*, 789-806.
[18] Zhang, Y., Rodionov, D. A., Gelfand, M. S., and Gladyshev, V. N. (2009) Comparative genomic analyses of nickel, cobalt and vitamin B12 utilization, *BMC Genomics 10*, 1-26.
[19] Crespo, A., Pedraz, L., Astola, J., and Torrents, E. (2016) Pseudomonas aeruginosa Exhibits Deficient Biofilm Formation in the Absence of Class II and III Ribonucleotide Reductases Due to Hindered Anaerobic Growth, *Front Microbiol 7*, 1-14.

Chapter 3

Structural characterization of pseudopaline, staphylopine and yersinopine dehydrogenase

Previously published as: McFarlane, J. S., Davis, C. L., and Lamb, A. L. (2018) Staphylopine, pseudopaline and yersinopine dehydrogenases: a structural and kinetic analysis of a new functional class of opine dehydrogenase, *J Biol Chem*. 293 (21):8009-8019.

Introduction

Opine dehydrogenases (ODH) are a family of NAD(P)H-dependent oxidoreductases (E.C. 1.5.1) that catalyze the condensation of an α or ω amino group from an amino acid with an α-keto acid followed by reduction with NAD(P)H, producing a family of products known as N-(carboxyalkyl) amino acids or opines (**Figure 3-1**) [1]. Opines are composed of a variety α-keto acid and amino acid substrates and have diverse functional roles. Octopine, isolated from octopus muscle by Morizawa in 1927, was the first described opine, composed of pyruvate and arginine [2]. ODHs are widespread in cephalopods and mollusks, such as *Pecten maximus*, the King Scallop, where they allow the continuation of glycolysis under anaerobic conditions by shunting pyruvate into opine products and regenerating NAD^+ [3]. Opines are also associated with crown gall tumor pathogenesis caused by *Agrobacterium tumifaciens*. In these plant infections, ODHs are encoded by the Ti plasmid. When expressed in the infected plant cell they convert plant metabolites into opines providing nutrients to the pathogen. Variant strains of *A. tumifaciens* have been shown to encode ODHs utilizing α-keto acids such as glyoxylate, pyruvate and α-ketoglutarate, and amino acids such as L-histidine, L-arginine, L-lysine and L-methionine [4]. ODHs have also been characterized in soil bacteria such as *Pseudomonas putida* [5], the yeast *Saccharomyces cerevisiae* [6], and *Arthrobacter* Sp. Strain 1C, which incorporates glyoxylate or pyruvate and several different amino acids into a variety of opines [7, 8]. These examples highlight the existence of diverse products by this enzyme family.

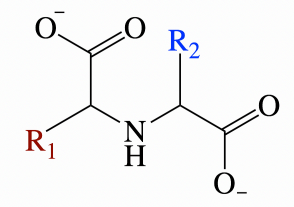

Figure 3-1. Generalized α-NH_2 opine. R1 (*red*) corresponds to the amino acid side chain. R2 (*blue*) corresponds to the variable position for the α-keto acid substrate.

Recently, novel opine compounds acting as metallophores have been identified [9-11], with variants found in *Staphylococcus aureus* (staphylopine) and *Pseudomonas aeruginosa* (pseudopaline). The occurrence of an additional variant in *Yersinia pestis* (yersinopine) has also been predicted and is explored further in this work. These opine metallophores play an important role in metal acquisition, with staphylopine involved in zinc [12], cobalt, nickel and iron uptake [9] and pseudopaline involved in zinc, cobalt [13] and iron [14] uptake. These metallophores are also associated with the pathogenesis of several disease states. In *S. aureus*, murine bacteremia and urinary tract infections are attenuated when the staphylopine receptor CntA is deleted [15]. Additionally, staphylopine production is upregulated in an endocarditis rat model [16]. *P. aeruginosa* burn wound and respiratory infections are attenuated for pseudopaline export transport mutants [14], and the pseudopaline pathway is upregulated in a murine acute pneumonia model [17] and in clinical isolates from burn and respiratory infections in humans [18, 19]. These findings suggest an important role for opine metallophores in infectious disease.

Opine metallophore biosynthesis requires two enzymes, a nicotianamine synthase (NAS) and an opine dehydrogenase (ODH). The nicotianamine synthase is an S-adenosyl-L-methionine (SAM)-dependent aminoalkyl transferase that forms a secondary amine between an amino acid and the aminobutyrate moiety of SAM (**Figure 3-2**). These enzymes are commonly associated with the production of the plant metallophore nicotianamine, composed of three aminobutyrate moieties derived from SAM[20]. *P. aeruginosa* NAS uses available L-histidine along with SAM in the production of L-His-Nicotianamine (L-HisNA), the substrate for PaODH. *S. aureus,* however, encodes a third enzyme, a histidine racemase, that generates D-histidine for use by the SaNAS in the production of D-His-Nicotianamine (D-HisNA), the substrate for SaODH. Each ODH binds HisNA substrate performing a reductive condensation with an α-keto acid, followed by reduction using NAD(P)H, and generating the opine metallophore product.

Two opine dehydrogenases have been structurally characterized: Norvaline dehydrogenase (N^2-(1-D-carboxylethyl)-L-norvaline:NAD^+ oxidoreductase) from *Arthrobacter* sp.

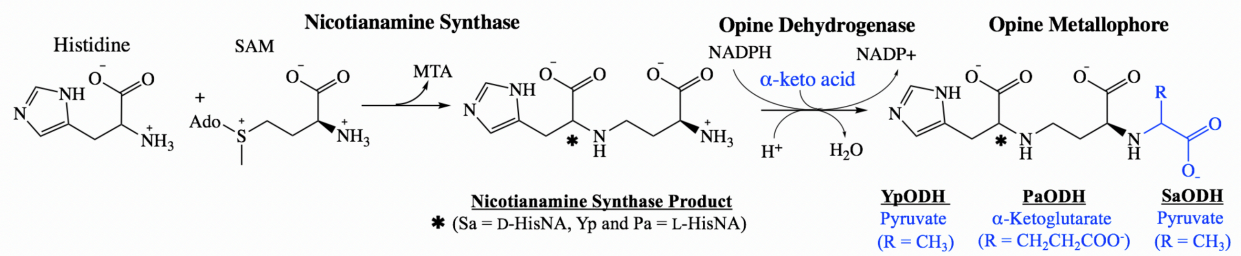

Figure 3-2. Opine metallophore biosynthesis. Generalized reaction scheme for opine metallophore production by NAS and ODH. SaODH recognizes D-HisNA (nicotianamine incorporating D-histidine), whereas YpODH and PaODH recognize L-HisNA (nicotianamine incorporating L-histidine). *R* represents the α-keto acid side chain incorporated by the ODH enzymes. *MTA*, methylthioadenosine.

Strain 1C (PDB: 1BG6) and octopine dehydrogenase (N^2-(D-1-carboxyethyl)-L-arginine:NAD^+ oxidoreductase) from *Pecten maximus* (PDB: 3C7A, 3C7C, 3C7D and 3IQD). These two enzymes have different functional roles and low sequence identity (≤16%) when compared to staphylopine, pseudopaline and yersinopine dehydrogenase. We determined X-ray crystal structures of Sa, Pa and YpODH to expand the structural characterization of this enzyme class. Additionally, we observe differential substrate specificity by yersinopine dehydrogenase (YpODH - *Y. pestis*), pseudopaline dehydrogenase (PaODH - *P. aeruginosa*) and staphylopine dehydrogenase (SaODH - *S. aureus*). The substrate specificity for each enzyme was demonstrated using a steady-state kinetic approach and the structural determinants of this specificity were investigated using x-ray crystallography.

Materials and Methods

Preparation of Overexpression Plasmids

S. aureus and *P. aeruginosa* ODH and NAS genes were prepared for overexpression as previously described [10]. The gene sequence for the *Y. pestis* CO92 strain ODH (YPO1347) was acquired from NCBI with accession number YP_002346370.1. This sequence was codon optimized for expression in *E. coli* by GenScript and ligated into pET-15TV with an N-terminal hexahistidine affinity tag. The plasmids were transformed into New England Biolabs BL21 (DE3) cells for expression.

Protein Expression and Purification

S. aureus and *P. aeruginosa* ODH and NAS were expressed and purified as previously described [10]. For YpODH, baffled flasks with 1 l of LB Miller media containing 200 µg/ml ampicillin were inoculated with 10 ml of overnight culture (50 ml grown at 37 °C, 225 rpm) and grown to an O.D. of 0.6 at 37 °C (2-3 hrs.). Cultures were induced with 200 µl of 1 M isopropyl β-D-1-thiogalactopyranoside (IPTG) and grown 21 hours at 15 °C. Cells were centrifuged at 4225 x g for 10 minutes. The pellet was resuspended in 50 mM potassium phosphate pH 8, 300 mM NaCl, 50 mM imidazole and 10% (v/v) glycerol. Cells were French pressed 3 times at 15000 psi and the

lysate was centrifuged for 1 hour at 23,426 x g before loading onto a GE Healthcare nickel-chelating fast flow sepharose column equilibrated with the same buffer. Protein was eluted using a linear gradient of increasing imidazole up to 500 mM. YpODH elutes at 185 mM imidazole. Protein was loaded onto a GE Superdex 200 size exclusion chromatography column equilibrated with 50 mM potassium phosphate pH 8, 150 mM sodium citrate and 20% (v/v) glycerol. YpODH eluted at a molecular weight of 93 kDa, roughly equivalent to a dimer of the 50.9 kDa YpODH protein. YpODH was concentrated using Millipore Amicon centrifugation concentrators with 30,000 MWCO to a final concentration of 8 mg/ml as measured by Bradford assay prior to flash freezing aliquots in liquid nitrogen. This preparation yields 25 mg per liter of culture.

Selenomethionine (SeMet) Substituted YpODH Expression and Purification

YpODH-SeMet was produced by inhibiting methionine biosynthesis following the method of Van Duyne and Clardy [21], with the exception that pET15TV-YpODH cultures were grown in M9 minimal media at 37°C to an OD_{600} of 0.7 prior to the addition of the amino acid mix containing 60 mg of selenomethionine. Subsequent expression and purification steps were carried out as described above for native protein except that 1.5 µM Tris(2-carboxyethyl)phosphine (TCEP) was added to YpODH-SeMet prior to injection onto the GE Superdex 200 size exclusion chromatography column equilibrated with 50 mM potassium phosphate pH 8, 150 mM sodium citrate, 20% glycerol, and 1 mM TCEP. Collected protein was concentrated to 8.4 mg/ml and frozen in liquid nitrogen with a yield of 13 mg per liter of culture.

Initial rate reactions to determine steady state kinetic parameters

Initial rates were measured by observing NADPH oxidation as a loss of absorbance at 340 nm using a TgK stopped flow spectrometer with a xenon lamp at 22 °C. The reaction buffer was 50 mM Tris pH 8.0 (Sa) or 50 mM potassium phosphate pH 8.0 (Yp and Pa). NAS (46 µM SaNAS or 56 µM PaNAS) was incubated with 4 mM histidine (D-His for SaNAS or L-His for PaNAS) and 4 mM S-adenosyl-L-methionine (SAM) for 75 minutes at 22 °C to produce D- or L-HisNA in non-rate-limiting excess. ODH at 2 µM and 400 µM NAD(P)H (SaODH and PaODH) or 600 µM

NAD(P)H (YpODH) were then added to complete the parent mix. Sodium pyruvate, glyoxylic acid, oxaloacetic acid or α-ketoglutaric acid (Sigma) were reconstituted in reaction buffer prior to serial dilution in the same buffer. The pH of glyoxylic acid and oxaloacetic acid was adjusted to 8.0 prior to serial dilution to compensate for the pH shift observed for these α-keto acids at higher concentrations. The ODH reaction was initiated by mixing an α-keto acid with the parent mix in a 1:1 ratio in the stopped flow spectrometer. Secondary plots of initial rates were fit to the Michaelis-Menten equation to determine kinetic parameters. For NAD(P)H initial rates, 2 mM α-keto acid (pyruvate – SaODH and YpODH or α-ketoglutarate – PaODH) replaced NAD(P)H in the parent mix, and each reaction was initiated with NAD(P)H at the concentrations above. The non-rate-limiting concentration of all substrates was determined by comparing full progress curves for varied concentrations of substrates and ODH enzyme. Each experiment was repeated at least three times and error was calculated as the standard deviation of these trials.

Protein Crystallization

All crystals were grown in hanging drops composed of 1.5 µl protein and 1.5 µl well solution at 24 °C. Crystals were transferred into well solution supplemented with 25% glycerol (YpODH and SaODH) or 20% ethylene glycol (PaODH) as a cryoprotectant and flash cooled in liquid nitrogen prior to data collection.

YpODH-Apo crystals were grown using 8.0 mg/ml N-terminal hexahistidine tagged purified protein in a well solution of 3.5 M sodium formate pH 6.0. Subsequent YpODH crystals were aided by microseeding from this condition. For YpODH-$NADP^+$, protein was pre-incubated with 1 mM $NADP^+$, and crystals were grown in 2.7 M sodium formate pH 6.0, 1.8% ethyl acetate aided by microseeding. YpODH-SeMet crystals were grown in 3.1 M sodium formate pH 7.5 aided by microseeding. After drops were mixed, 2-mercaptoethanol was added to the well solution to a final concentration of 1%. All crystals grew as thin plates within 2 days and reached full size within 10 days. Samples of purified YpODH and YpODH from dissolved protein crystals were submitted to the Mass Spectrometry Research Center Proteomics Laboratory at Vanderbilt University for

MALDI-TOF analysis to verify the amino acid sequence and confirm that no proteolytic cleavage had occurred.

PaODH at 7.5 mg/ml, with its N-terminal hexahistidine tag, was supplemented with 2 mM $NADP^+$ and grown in a well solution of 100 mM BisTris pH 5.45, 200 mM ammonium acetate, 26% (w/v) PEG 3350. Small, rod-shaped crystals formed within three days.

SaODH at 12 mg/ml, with its N-terminal hexahistidine tag, was supplemented with 2 mM $NADP^+$ prior to crystallization for both the SaODH-Apo and SaODH-$NADP^+$ structures. SaODH-Apo crystallized in a well solution of 100 mM sodium citrate:HCl pH 5.6, 200 mM ammonium sulfate, 25% (w/v) PEG 4000. SaODH-$NADP^+$ crystallized in a well solution of 100 mM Tris pH 8.0, 100 mM lithium sulfate, 23% (w/v) PEG 3350. In both conditions, square plates began forming within two days and reached full size in two weeks. Cryoprotectant was supplemented with 2 mM $NADP^+$ for the holo, but not the apo, structure.

Data Collection and Structure Determination

Diffraction data were collected remotely using BluIce [22] at the Stanford Synchrotron Radiation Lightsource (SSRL, Menlo Park, CA). For all structures, 180° of data with 0.15° oscillation, were collected at a temperature of 100K. Statistics for data collection and refinement are listed in **Table 3-1**. Data were processed in XDS [23].

YpODH-SeMet data were collected on beamline 12-2 at a wavelength of 0.9795 Å and 0.2 s exposure with a detector distance of 350 mm. Phasing and initial model building were performed using CRANK2 [24] in the CCP4 package [25]. Substructure determination found all 5 selenomethionine sites. Subsequent density modification and model building placed 426 out of 456 amino acids resulting in an initial R_{work} = 25.3 and an R_{free} = 29.6.

YpODH-Apo data were collected on beamline 9-2 at a wavelength of 0.9794 Å and 0.2 s exposure with a detector distance of 400 mm. The YpODH-Apo structure was solved with Phenix Phaser using YpODH-SeMet as a search model with a log likelihood gain (LLG) = 9992 and a TFZ = 85.4.

Table 3-1 Data collection and refinement statistics

All data were collected on beamline 12-2 or 9-2 at the Stanford Synchrotron Radiation Lightsource. Values in parentheses are for the highest resolution shells.

	YpODH-SeMet	YpODH-Apo	YpODH-NADP$^+$	PaODH-NADP$^+$	SaODH-Apo	SaODH-NADP$^+$
Data collection						
Spacegroup	$C222_1$	$C222_1$	$C222_1$	C2	$P2_12_12$	$P2_12_12$
Unit cell (Å)	a=98.0 b=123.9 c=88.5	a=97.9 b=124.1 c=88.0	a=98.4 b=125.7 c=88.0	a=180.0 b=53.6 c=96.8 β=99.0°	a=187.7 b=49.1 c=58.6	a=186.1 b=49.3 c=59.1
Resolution range (Å)	38.4 - 2.15	38.4 - 2.00	38.7 - 1.94	38.1 – 1.95	38.6 - 2.29	38.6 - 2.49
Completeness (%)	99.2 (98.1)	99.6 (95.7)	99.2 (95.8)	96.7 (94.5)	99.8 (96.7)	99.5 (96.2)
Total reflections	118,529	245,736	181,826	117,971	165,517	126,596
Unique reflections	29,208	36,673	40,471	64,907	25,087	19,677
I / σ	10.2 (2.2)	12.2 (2.4)	14.2 (2.0)	10.6 (2.6)	13.0 (2.0)	12.2 (2.0)
R_{merge}[a]	7.3 (50.9)	8.2 (104)	5.3 (68.8)	7.0 (77.7)	8.8 (86.0)	9.0 (88.9)
R_{pim}[b]	6.0 (43.5)	5.1 (64.7)	4.1 (55.3)	6.5 (72.3)	5.4 (55.3)	5.6 (56.8)
Multiplicity	4.1 (4.0)	6.7 (6.5)	4.5 (4.3)	3.5 (3.4)	6.6 (6.2)	6.4 (6.3)
No. of Se Sites	5					
Initial FOM[c]	22.7					
FOM after density mod[c]	50.0					
Final Mean FOM[c]	85.3					
Refinement						
Resolution range (Å)		35.89 - 2.00	38.7 - 1.94	38.1 – 1.95	37.63 – 2.29	37.8 - 2.49
No. of reflections		36,620	40,415	64,880	25,032	19,596
R_{work} / R_{free}[d]		20.0 / 24.6	19.0 / 22.9	16.7 / 20.8	20.7 / 26.8	22.0 / 26.6
No. non-hydrogen atoms		3372	3485	7099	3557	3531
Protein		3325	3296	6602	3468	3476
Ligand/ion			48	100	32	45
Water		47	141	397	57	10
Ramachandran allowed (%)		100	100	100	100	100
Wilson *B*		32.3	31.5	24.3	39.6	51.1
Average *B* (Å^2)		45.5	38.2	26.6	47.1	56.3
Protein		45.6	38.1	26.5	47.0	56.1
Ligand/ion			41.6	26.4	74.1	76.6
R.m.s. deviations						
Bond lengths (Å)		0.009	0.010	0.010	0.009	0.015
Bond angles (°)		1.01	1.01	1.09	0.97	1.26

[a] $R_{merge} = \sum_{hkl}|I_{hkl} - \langle I\rangle_{hkl}|/\sum_{hkl} I_{hkl}$ where I_{hkl} is the intensity of reflection *hkl* and $\langle I\rangle$ is the mean intensity of related reflections.

[b] $R_{pim} = \sum_{hkl}\sqrt{1/n-1}\,|I_{hkl} - \langle I\rangle_{hkl}|/\sum_{hkl} I_{hkl}$ where n is the multiplicity of related reflections.

[c] Figure of Merit (FOM) = $\langle \alpha \sum P_\alpha e^{i\alpha} / \sum P_\alpha \rangle$ where the phase = α and the phase probability distribution = P_α

[d] $R = \sum\big|F_o - |F_c|\big| / \sum|F_o|$ where F_o = to the observed structure factors and F_c = structure factors calculated from the model. 5% of the reflections were initially reserved to create an R_{free} test set used during each subsequent round of refinement.

YpODH-NADP$^+$ data were collected on beam 9-2 at a wavelength of 0.9794 Å and 0.32 s exposure with the detector distance at 350 mm. The YpODH-NADP$^+$ structure was solved using Phenix Phaser with YpODH-Apo as a search model with a LLG = 6081 and a TFZ = 66.2.

PaODH-NADP$^+$ data were collected on beamline 9-2 at a wavelength of 0.97891 Å and 0.83 s exposure with a detector distance of 410 mm. These data were processed to 2.53 Å. The YpODH-Apo structure was used as a search model for molecular replacement in Phenix Phaser resulting in a solution with a LLG = 73 and a TFZ = 8.8. Phenix Morph Model was used to improve model fit. Phenix Autobuild placed 610 out of 868 amino acid residues of the two monomers in the asymmetric unit with an initial R_{work} = 31.2 and R_{free} = 36.4. This model was then fully refined to an R_{work} = 19.3 and R_{free} = 26.4. Higher resolution PaODH-NADP$^+$ data were subsequently collected on beamline 12-2 at a wavelength of 0.9795 Å and 0.2 s exposure with a detector distance of 350 mm. The 2.53 Å PaODH model was used to determine initial phases for the higher resolution dataset using Phenix Refine resulting in an initial R_{work} = 24.4 and R_{free} = 29.6.

SaODH-NADP$^+$ data were collected on beamline 12-2 at a wavelength of 0.97937 Å and 0.2 s exposure with a detector distance of 490 mm. The YpODH-Apo structure was used as a search model for molecular replacement in Phenix Phaser resulting in a solution with a LLG = 70.8 and a TFZ = 9.8. Phenix Autobuild placed 342 out of 432 amino acid residues with an initial R_{work} = 37.4 and R_{free} = 45.0. Active site density corresponding to NADP$^+$ was incomplete for the nicotinamide ring, so the nicotinamide was omitted from the final model.

SaODH-Apo data were collected on beamline 9-2 at a wavelength of 0.9795 Å and 0.28 s exposure with a detector distance of 404 mm. The SaODH-NADP$^+$ structure was used as a search model for molecular replacement in Phenix Phaser giving a solution with a LLG = 6,672 and a TFZ = 57.3. Initial refinement in Phenix Refine had an R_{work} = 23.0 and R_{free} = 29.5.

For each structure, rounds of model building and refinement were completed in Coot [26] and Phenix Refine [27]. Waters were placed by Phenix Refine, corrected manually and verified following a round of refinement. For each NADP$^+$ bound structure, density was visible for NADP$^+$

in the initial electron density map. $NADP^+$ was added to the model by Phenix Ligandfit after polypeptide refinement was complete, followed by a round of refinement and verified by generating a simulated annealing composite omit map in Phenix with $NADP^+$ omitted from the

Crystallographic Models

Summary data for the models is provided in **Table 3-2**. Ramachandran analysis was performed by MolProbity [28] showing good geometry with no outliers for YpODH, PaODH or SaODH. A comparison of structures and calculation of rmsd values were performed using PDBeFold [29]. TM scores were determined by TM-align [30]. Interface surface areas and interacting residues for the assembled dimers were analyzed using PDBePISA [31]. The active site surface was calculated by CASTp (computed atlas of surface topography of proteins) [32]. Structure figures were generated in PyMOL (The PyMOL Molecular Graphics System, Version 2.0 Schrödinger, LLC.). The atomic coordinates and structure factors have been deposited in the Protein Data Bank (accession codes in **Table 3-2**).

Results and Discussion

Substrate specificity

We previously reported the enzymatic production of pseudopaline by the *P. aeruginosa* NAS and ODH [10], and confirmed the production of staphylopine by the homologous *S. aureus* enzymes as first demonstrated by Ghssein et al. [9]. In that work, we examined the utilization of different α-keto acids by the ODH enzymes observing differential specificity. To better define this specificity we determined steady-state kinetic parameters for the ODHs in the presence of pyruvate, oxaloacetate and glyoxylate (YpODH and SaODH) or α-ketoglutarate (PaODH). Each ODH requires D- or L-HisNA substrate made by NAS. To produce this substrate in excess, NAS was first incubated with SAM and D-His (SaNAS) or L-His (PaNAS) before adding ODH and NAD(P)H to the parent mix. Reactions were then initiated by combining the parent mix with α-keto acid and measuring a loss of absorbance at 340 nm as NAD(P)H is oxidized to $NAD(P)^+$.

Table 3-2 Model Components

Protein	PDB Code	ASU[a]	Ordered Residues	Waters	Ligands[b]
YpODH-Apo	6C4L	1	1-157, 182-348, 361-456	47	None
YpODH-$NADP^+$	6C4M	1	1-156, 181-348, 362-455	141	1 $NADP^+$
PaODH-$NADP^+$	6C4N	2	Chain A: 7-431 Chain B: 7-62, 70-431	397	2 $NADP^+$ 1 Ethylene Glycol
SaODH-Apo	6C4R	1	1-428	117	2 Glycerol 4 Sulfate
SaODH-$NADP^+$	6C4T	1	2-428	10	1 $NADP^+$ 1 Glycerol

[a] number of monomers in the asymmetric unit
[b] glycerol and ethylene glycol were used as cryoprotectants and sulfate was in the SaODH-Apo well solution

SaODH selects the α-keto acid substrate pyruvate (**Table 3-3, Fig. 3-3**), but also exhibits limited turnover with oxaloacetate and glyoxylate. The SaODH k_{cat} for oxaloacetate is equivalent to pyruvate, but k_{cat}/K_m is 49-fold lower. For glyoxylate k_{cat} is 3.5-fold lower and k_{cat}/K_m is 370-fold lower. Catalysis in the presence of α-ketoglutarate was within error of zero as previously reported[10]. In contrast, PaODH uses α-ketoglutarate (**Table 3-3, Fig. 3-3**). It is able to incorporate α-ketoglutarate with either NADH or NADPH as a substrate with a two-fold higher catalytic efficiency using NADPH. This suggests that either NADPH or NADH may be used *in vivo* dependent upon availability. We observe very limited catalysis for PaODH in the presence of glyoxylate (apparent k_{cat} = 0.015 s^{-1}; 3 fold higher than the detection limit of 0.005 s^{-1}). Catalysis is within error of zero for pyruvate and oxaloacetate as previously reported[10]. YpODH selects pyruvate as its primary substrate (**Table 3-3, Fig. 3-3**). The YpODH k_{cat} for oxaloacetate is equivalent to pyruvate, but k_{cat}/K_m is 28-fold lower. For glyoxylate k_{cat} is 1.4-fold lower and k_{cat}/K_m is 35-fold lower. Catalysis with α-ketoglutarate was within error of the detection limit. These data indicate that glyoxylate and oxaloacetate are not effective substrates for these enzymes. YpODH and SaODH are specific for pyruvate, whereas PaODH is specific for α-ketoglutarate.

SaNAS produces D-HisNA, whereas PaNAS produces L-HisNA. Amino acid specificity for the final opine metallophore could be a result of the NAS alone, or the ODH may be stereospecific for one HisNA. Therefore, each ODH was tested with HisNA produced by SaNAS and by PaNAS, with excess NADPH, and initiated by α-keto acid (Sa and Yp – pyruvate, Pa - α-ketoglutarate) (**Table 3-3**). Remarkably, while SaODH produces staphylopine *in vivo* using D-HisNA [9], it exhibits a k_{cat} 3.3-fold higher in the presence of L-HisNA with a k_{cat}/K_m 3-fold lower. Both PaODH and YpODH select L-HisNA as their substrate. In the presence of D-HisNA, PaODH exhibits a k_{cat} of 0.016 s^{-1} (3-fold above the detection limit) and YpODH k_{cat} is within error of the detection limit. Therefore, the ODHs have differing tolerances for the amino acid stereochemistry incorporated by the NAS into the HisNA substrate. Although YpNAS has not yet been purified preventing

Table 3-3 Kinetic Parameters

Protein	Initiating Substrate	NAD(P)H	HisNA Substrate	k_{cat} (s^{-1})	K_m (μM)	k_{cat}/K_m ($M^{-1}s^{-1}$)
SaODH	Pyruvate	NADPH	D-HisNA	0.26 ± 0.01	29 ± 2	8900 ± 700
SaODH	Pyruvate	NADPH	L-HisNA	0.85 ± 0.01	280 ± 2	3000 ± 40
SaODH	Oxaloacetate	NADPH	D-HisNA	0.26 ± 0.01	1400 ± 100	180 ± 10
SaODH	Glyoxylate	NADPH	D-HisNA	0.074 ± 0.003	3000 ± 200	24 ± 2
PaODH	α-Ketoglutarate	NADPH	L-HisNA	0.42 ± 0.01	14 ± 1	31000 ± 2000
PaODH	α-Ketoglutarate	NADH	L-HisNA	0.92 ± 0.01	61 ± 3	15000 ± 800
YpODH	Pyruvate	NADPH	L-HisNA	0.30 ± 0.01	73 ± 1	4200 ± 200
YpODH	Oxaloacetate	NADPH	L-HisNA	0.29 ± 0.03	1900 ± 400	150 ± 40
YpODH	Glyoxylate	NADPH	L-HisNA	0.22 ± 0.01	1900 ± 100	120 ± 8

Protein	Initiating Substrate	α-Keto acid	HisNA Substrate	k_{cat} (s^{-1})
SaODH	NADPH	Pyruvate	D-HisNA	0.26 ± 0.01
SaODH	NADH	Pyruvate	D-HisNA	0.009 ± 0.002
PaODH	NADPH	α-Ketoglutarate	L-HisNA	0.33 ± 0.02
PaODH	NADH	α-Ketoglutarate	L-HisNA	0.71 ± 0.02
YpODH	NADPH	Pyruvate	L-HisNA	0.38 ± 0.02
YpODH	NADH	Pyruvate	L-HisNA	0.013 ± 0.004

Blue color designates primary substrates, *in vivo,* corresponding to Figure 2. Reaction buffer was 50 mM potassium phosphate pH 8.0 (Yp and Pa) or Tris pH 8.0 (Sa) and 5% glycerol. HisNA was produced by reacting histidine with S-adenosyl-L-methionine and PaNAS (L-HisNA) or SaNAS (D-HisNA). For reactions initiated with α-keto acid, ODH at 2 μM and 400 μM (Pa and Sa) or 600 μM (Yp) NAD(P)H were combined with the NAS reaction mixture in one syringe and mixed 1:1 in a stopped-flow spectrometer with α-keto acid in reaction buffer in a second syringe. For reactions initiated with NAD(P)H, ODH at 2 μM and 4 mM pyruvate (Sa and Yp) or α-ketoglutarate (Pa) were combined with the NAS reaction mixture in one syringe and mixed 1:1 with 400 μM (Pa and Sa) or 600 μM NAD(P)H (Yp).

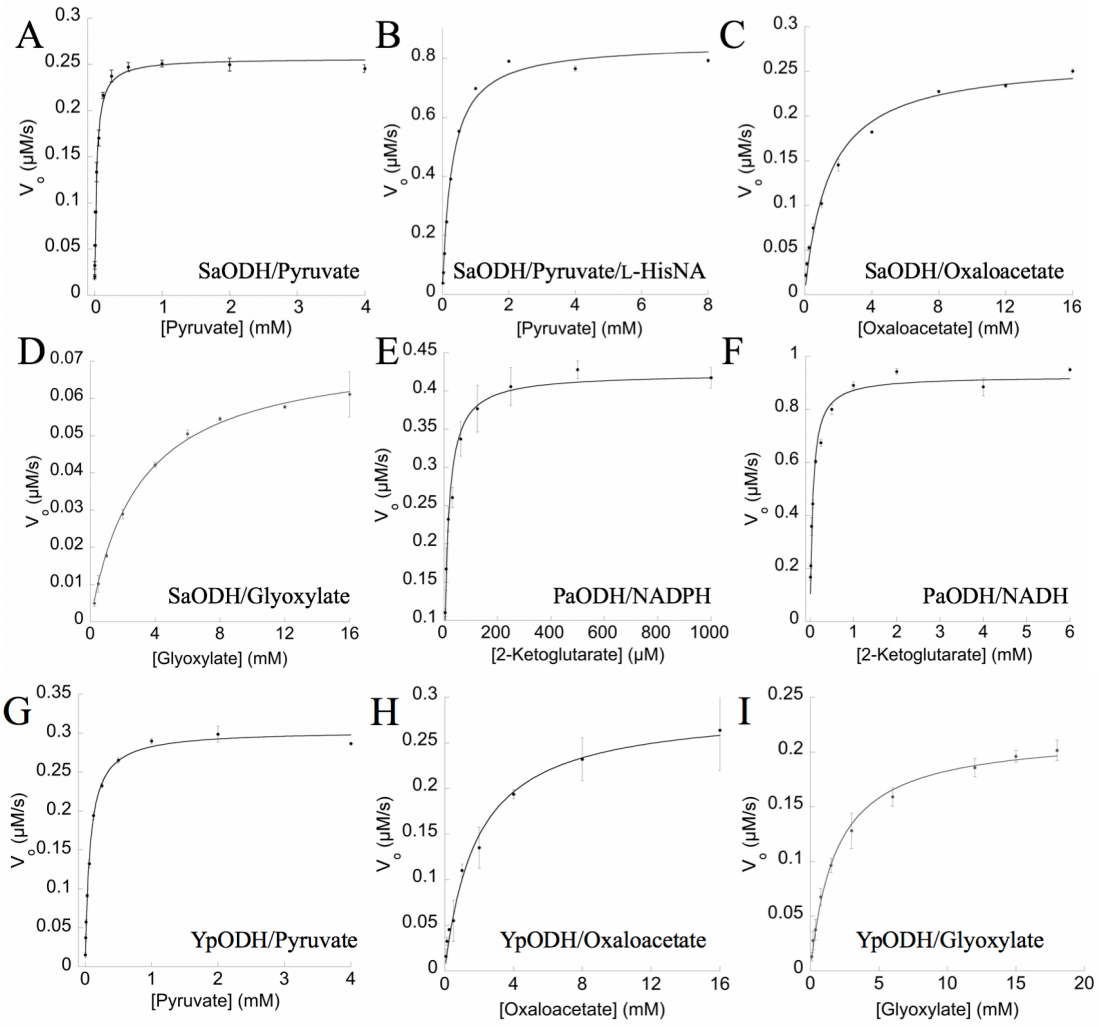

Figure 3-3. Steady-State Kinetic Plots. Initial rates were determined by applying linear fits to the primary plots of [NAD(P)H] (determined using an extinction coefficient of 6220 $cm^{-1}M^{-1}$ for NAD(P)H) vs. time. For PaODH, polynomial fits were used to determine the initial rate. Secondary plots were fit with the Michaelis-Menten equation. Error bars represent the standard deviation of at least three trials. **A)** SaODH (1 μM) with 200 μM NADPH, 2 mM D-HisNA and initiated with pyruvate. **B)** SaODH (1 μM) with 200 μM NADPH, 2 mM L-HisNA and initiated with pyruvate. **C)** Same as for A, but initiated with oxaloacetate. **D)** Same as for A, but initiated with glyoxylate. **E)** PaODH (1 μM) with 200 μM NADPH, 2 mM L-HisNA and initiated with α-ketoglutarate. **F)** PaODH (1 μM) with 200 μM NADH, 2 mM L-HisNA and initiated with α- ketoglutarate. **G)** YpODH (1 μM)

with 300 μM NADPH, 2 mM L-HisNA and initiated with pyruvate. **H)** Same as for G, but initiated with oxaloacetate. **I)** Same as for G, but initiated with glyoxylate.

analysis, catalysis by YpODH in the presence of pyruvate and L-HisNA suggests the production of a yersinopine metallophore in *Y. pestis* (**Figure 3-2**). Future kinetic analysis with purified YpNAS will determine whether L-histidine or an alternate L- amino acid is incorporated into yersinopine.

While all three ODHs use NADPH, significant catalysis is observed for PaODH with NADH (**Table 3-3**). A comparison of relative k_{cat} values for each ODH was performed in the presence of saturating amounts of α-keto acid and D- or L-HisNA product with either NADH or NADPH. While both YpODH and SaODH show little turnover with NADH, 38-fold and 26-fold lower than the k_{cat} for NADPH respectively, the PaODH k_{cat} is 2.2-fold higher than the k_{cat} for NADPH. This is consistent with the k_{cat} differences observed when α-ketoglutarate is the initiating substrate (**Table 3-3**). In summary, SaODH and YpODH show specificity for NADPH, whereas PaODH is non-specific for the NAD(P)H substrate.

ODH structure determination

X-ray diffraction data were collected to determine crystal structures for YpODH, PaODH and SaODH (**Table 3-1**). Initially, opine-family dehydrogenases from *Pecten maximus* (PmODH - PDB: 3C7A) and *Arthrobacter* Sp. Strain 1C (ArODH - PDB: 1BG6) were used as models for molecular replacement trials, but a satisfactory phasing solution was not found. This was unsurprising given low sequence identity (15-18%). Selenomethionine-labeled YpODH was produced and single wavelength anomalous dispersion data were collected to 2.15 Å with anomalous signal to 2.85 Å. Anomalous phasing and density modification were attempted with Phenix Autosol [27] and resulted in an R_{free} value of 0.64, though helices and strands were clearly visible in the electron density maps. Phasing and density modification were then performed using CRANK2 [24] in CCP4 [25]. CRANK2 generated a model placing 93% of YpODH residues with an initial R_{free} of 0.30. After refinement, YpODH-SeMet was used as a molecular replacement model for a 2.0 Å YpODH-Apo data set (**Figure 3-4A**). YpODH-Apo was used as a molecular

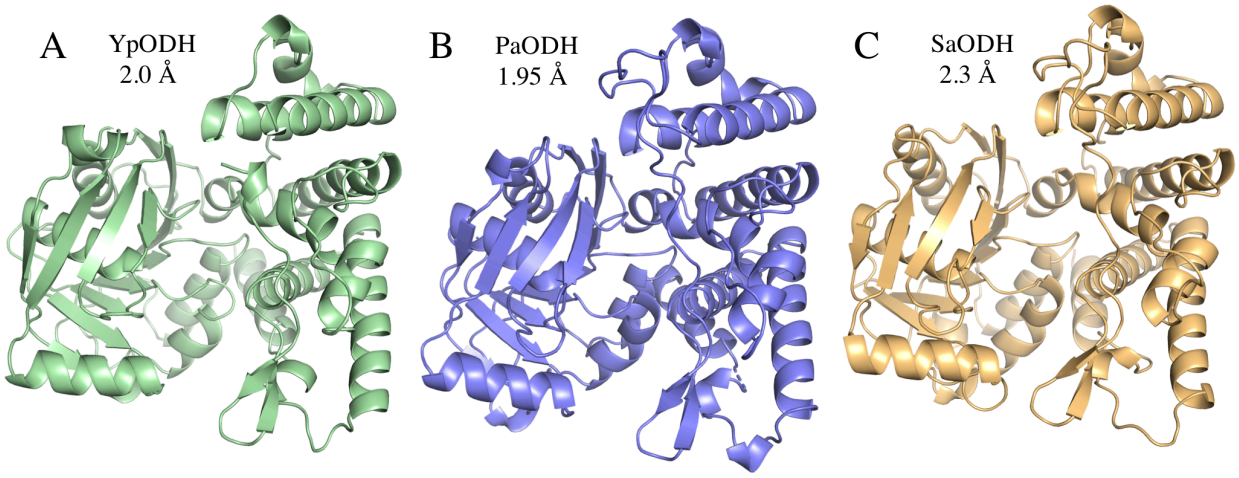

Figure 3-4. ODH Structural Comparisons. ODH Ribbon Diagrams. **A)** YpODH-Apo - 2.0 Å (green). **B)** PaODH-$NADP^+$ - 1.95 Å (blue). **C)** SaODH-Apo - 2.3 Å (yellow). All three proteins have the same secondary structural elements with TM-align scores between 0.91 and 0.93.

replacement model for the initial phasing of PaODH and SaODH (**Figure 3-4B,C**). In the subsequent discussion, amino acid numbering is for YpODH unless otherwise noted.

ODH overall structure

YpODH is composed of three domains (**Figure 3-5A**). NADPH binds along a canonical GXGXXA loop within the N-terminal NAD(P)H binding domain. This domain forms one half of the active site. The other half, and the proposed location for substrate binding, is formed by the catalytic domain. These domains are separated by a central cleft. Embedded within the catalytic domain is a third domain that forms a dimerization interface.

The NAD(P)H-binding domain has a Rossmann-like fold . This domain contains 12 β-strands (1-12), 5 α-helices (A, B, D-F) and one 3_{10} helix (C). Helix G acts as a linker connecting the NAD(P)H binding domain with the C-terminal, predominantly α-helical domains. αH-J and N-P as well as β 13-14 form the catalytic domain, while αK-M form the dimerization domain. All YpODH structures solved to date have no density for two loops comprised of residues 158-181 and 349-360. The residues from 158-181 contain three TQDIXAX sequence repeats of unknown function. The latter connects helix M to helix N between the catalytic and dimerization domains. Mass spectrometry confirmed that the missing amino acid sequences were present in both purified YpODH and YpODH crystals indicating that these loops are present but disordered in this crystal condition (**Figure 3-6**).

PaODH and SaODH share the same domain and secondary structural elements as YpODH (**Figure 3-3**). Rms deviations reflect this, ranging from 1.47-2.09 Å (PDBeFold) [29] with Tm scores [30] of 0.91-0.93 over 418-428 Cα residues. Whereas both YpODH and SaODH have one monomer in the asymmetric unit, PaODH has two. The two PaODH monomers have an rms deviation of 1.47 Å and a Tm score of 0.96 over 423 Cα. The YpODH TQDIXAX repeat sequence (158-181) is not found in PaODH or SaODH. Instead, a short, five residue loop connects β9-10. The disordered YpODH loop (349-360) connecting the dimerization and catalytic domains is

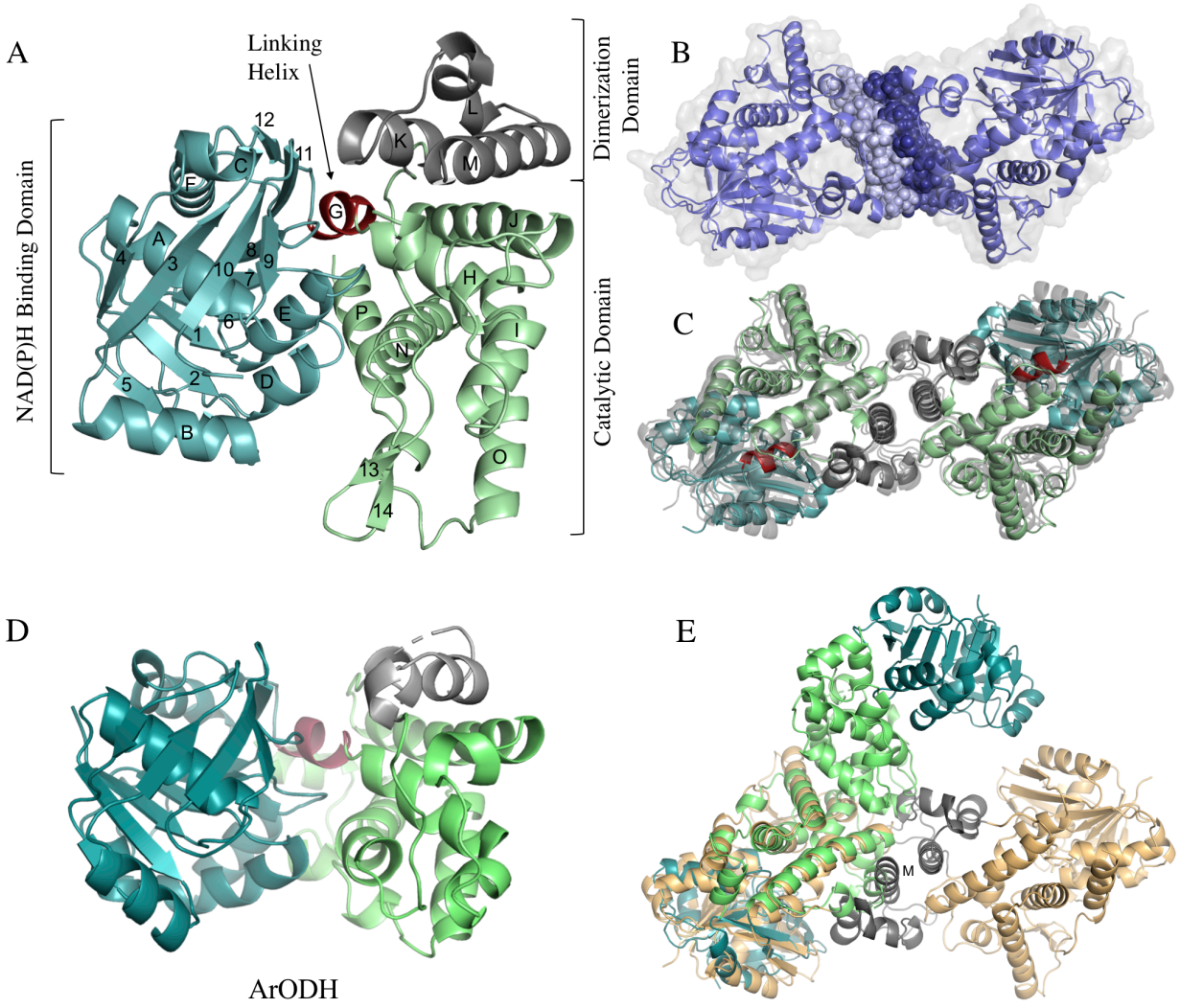

Figure 3-5. Global Structure, Assembly and Homolog Comparisons. A) YpODH structure. Helices are labeled with letters and strands with numbers beginning with the N-terminus. **B)** PaODH dimeric assembly. PISA calculated interface (1484 Å^2) between the PaODH homodimer depicted as blue spheres. **C)** Overlay of ODH Dimers. SaODH (gray) and YpODH (same color scheme as A) also form dimers with a symmetry mate using the same interface as PaODH (gray), each with a coiled coil forming the core of a largely hydrophobic interface. **D)** In ArODH (coloring as for YpODH) the dimerization domain is truncated, as is αO and β13-14. **E)** Overlay of the ArODH (colored as in D) and SaODH (yellow/gray) dimeric assemblies demonstrates the differing interface used by these homologues.

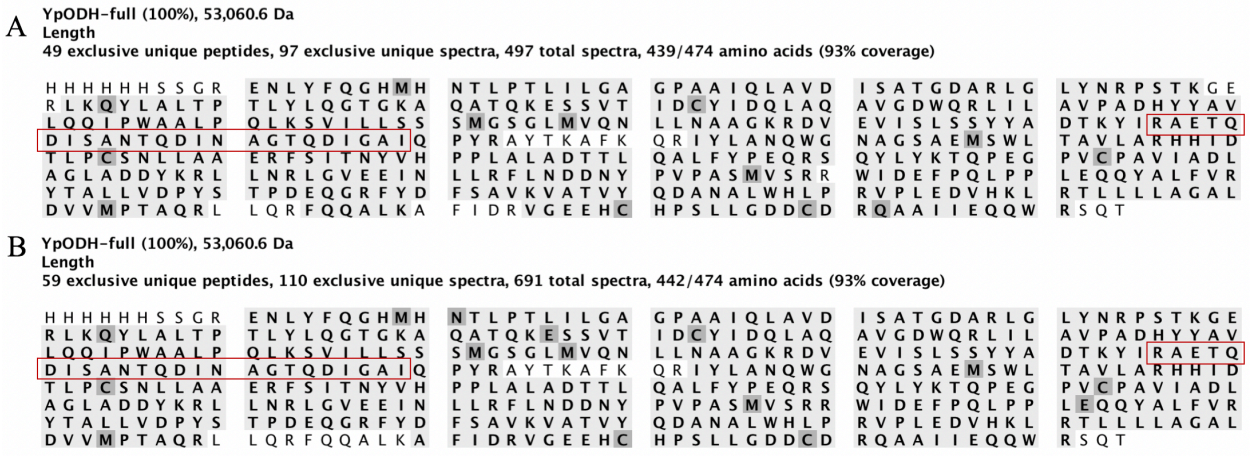

Figure 3-6. YpODH MS/MS Sequence Identification. Dark shading identifies residues that exhibit mass shifts due to sample preparation methods. Light shading identifies covered sequence. Red boxes indicate residues 158-181 missing from the X-ray crystal electron density. No shading identifies gaps in sequence coverage. **A)** YpODH sample from purified protein. **B)** YpODH sample from YpODH crystals. In both samples, residues 158-181 are present with complete sequence coverage. Criteria for peptide and protein identification: Scaffold (version Scaffold_4.8.4, Proteome Software Inc., Portland, OR) was used to validate MS/MS based peptide and protein identifications. Peptide identifications were accepted if they could be established at greater than 66.0% probability to achieve an FDR (false discovery rate) less than 1.0% by the Peptide Prophet algorithm (Keller, A et al Anal. Chem. 2002;74(20):5383-92). Protein identifications were accepted if they could be established at greater than 99.0% probability to achieve an FDR less than 1.0% and contained at least 5 identified peptides. Protein probabilities were assigned by the Protein Prophet algorithm (Nesvizhskii, Al et al Anal. Chem. 2003;75(17):4646- 58).

ordered in PaODH and SaODH and composes part of the dimerization interface. The absence of these loops in the YpODH model accounts for the slightly higher rms deviations for comparisons with YpODH, whereas the Tm-align scores suggest equivalent structural similarity between the three enzymes.

ODH dimeric assembly

All three ODHs are dimers by size exclusion chromatography (**Fig. 3-7**) and within their crystal structures (**Fig. 3-5B,C**). While the dimeric assembly is evident in the asymmetric unit of PaODH, the dimers for YpODH and SaODH are built using a crystallographic 2-fold rotation. The dimeric interface is formed by αL, αM, loop M-N and the C-terminus of αJ. PDBePISA calculates a buried surface area of 870 $Å^2$ for YpODH, 1484 $Å^2$ for PaODH and 1457 $Å^2$ for SaODH. The reduced surface area in YpODH is due to the disordered 349-360 loop. The interfaces are composed of 50-61% buried hydrophobic residues with minimal (0, 9 and 1 respectively) hydrogen bonds.

Homologous ODHs

Arthrobacter Sp. Strain 1C opine dehydrogenase (ArODH) and *Pecten maximus* opine dehydrogenase (PmODH) represent the nearest structurally characterized homologs with rms deviations of 2.43 Å and 2.85 Å over 307 Cα and 302 Cα residues. The core strands and helices of the NAD(P)H binding and catalytic domains show good alignment; however, an extended 3_{10}C, αP, αO and β13-14, found in the three ODHs described here, are absent or abridged in ArODH (**Fig. 3-5D**) and PmODH. ArODH is reported to be a dimer [33], yet its dimeric interface is formed by αJ and αO rather than αL-M as seen for Yp, Pa and SaODH (**Fig. 3-5E**). Notably, the key helices in the YpODH dimer are missing (αL), or truncated (αM), in ArODH. Glycerol-3-phosphate dehydrogenase is also a structural homolog of opine dehydrogenases. Human glycerol-3-phosphate dehydrogenase (PDB: 1XOV) has an rmsd of 3.12 Å over 240 Cα residues (compared to YpODH), demonstrating structural conservation of core elements from both the NAD(P)H-

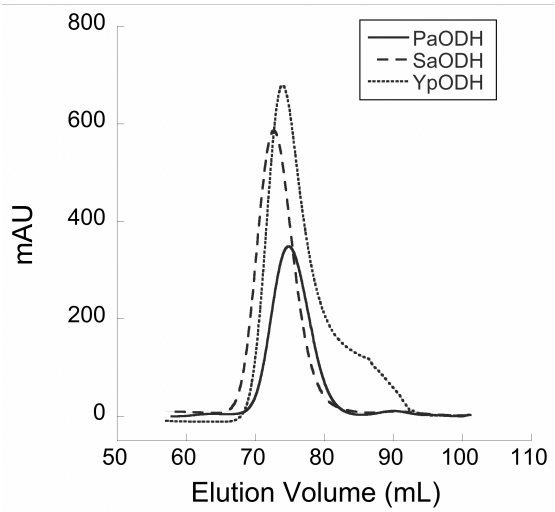

Figure 3-7. Size exclusion chromatography of YpODH, PaODH and SaODH. Overlay of ODH elution peaks from a GE Healthcare Sephadex 200 size exclusion chromatography column. YpODH (monomeric M.W. of 53.06 kDa) elutes at 74.0 mL equivalent to a M.W. of 93.1 kDa. PaODH (monomeric M.W. of 50.05 kDa) elutes at 74.9 mL equivalent to a M.W. of 86.5 kDa. SaODH (monomeric M.W. of 52.27 kDa) elutes at 72.7 mL equivalent to a M.W. of 103.0 kDa. Given molecular weights include hexahistidine tag and linker sequence.

binding and catalytic domains (**Fig. 3-8**). Any effort made in future to halt opine metallophore biosynthesis through ODH inhibition, must take care to exclude compounds active against human glycerol-3-phosphate dehydrogenase.

$NADP^+$ binding and selectivity

Structures with $NADP^+$ bound were solved for all three ODHs. The NAD(P)H binding motif, with the conserved sequence GXGXXA, is formed by the β1-αA loop. Residues within this loop (**Fig. 3-9A**) form hydrogen bonds with the adenosine ribose sugar and the phosphates spanning the nicotinamide and adenosine ribose sugars. The nicotinamide ring has good electron density in YpODH and PaODH, but was not resolved in SaODH and was omitted from the SaODH model. (**Fig. 3-9B**).

Hydrogen bonding patterns for the 2' phosphate of NADPH suggests an explanation for the differential specificity observed in our kinetic analysis. Stabilization of the phosphate differs between YpODH and SaODH, and PaODH (**Fig. 3-9C, D**). In YpODH and SaODH, K40 hydrogen bonds with the 2' phosphate, while in PaODH the structurally homologous R44 is hydrogen bonded to the backbone oxygens of P169 and L16 preventing coordination of the phosphate. Additionally, the H40 side chain in PaODH stacks with the adenosine and hydrogen bonds with the 2' phosphate turning it away from R44. In YpODH and SaODH, R36 stacks next to the adenosine and hydrogen bonds with the phosphate, but its longer side chain rotates the 2' phosphate toward K40, positioning the phosphate to form an additional hydrogen bond. Finally, S38, whose side chain forms a hydrogen bond with the 2' phosphate, is substituted with G42 in PaODH. Collectively, these features result in a much more extensive hydrogen bonding network around the 2' phosphate in YpODH and SaODH than in PaODH. This is consistent with YpODH and SaODH specificity for NADPH, while PaODH shows catalytic efficiency within two-fold with either NADPH or NADH.

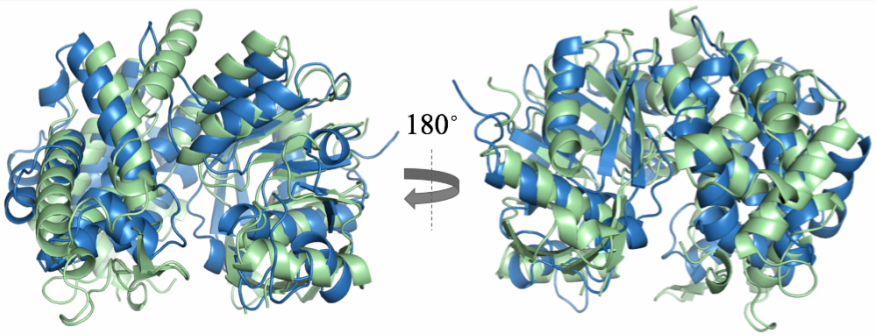

Figure 3-8. PDBeFold Overlay. YpODH (green) and Human Glycerol-3-Phosphate Dehydrogenase (blue) (PDB: 1X0V) have an rmsd of 3.12 Å over 240 residues.

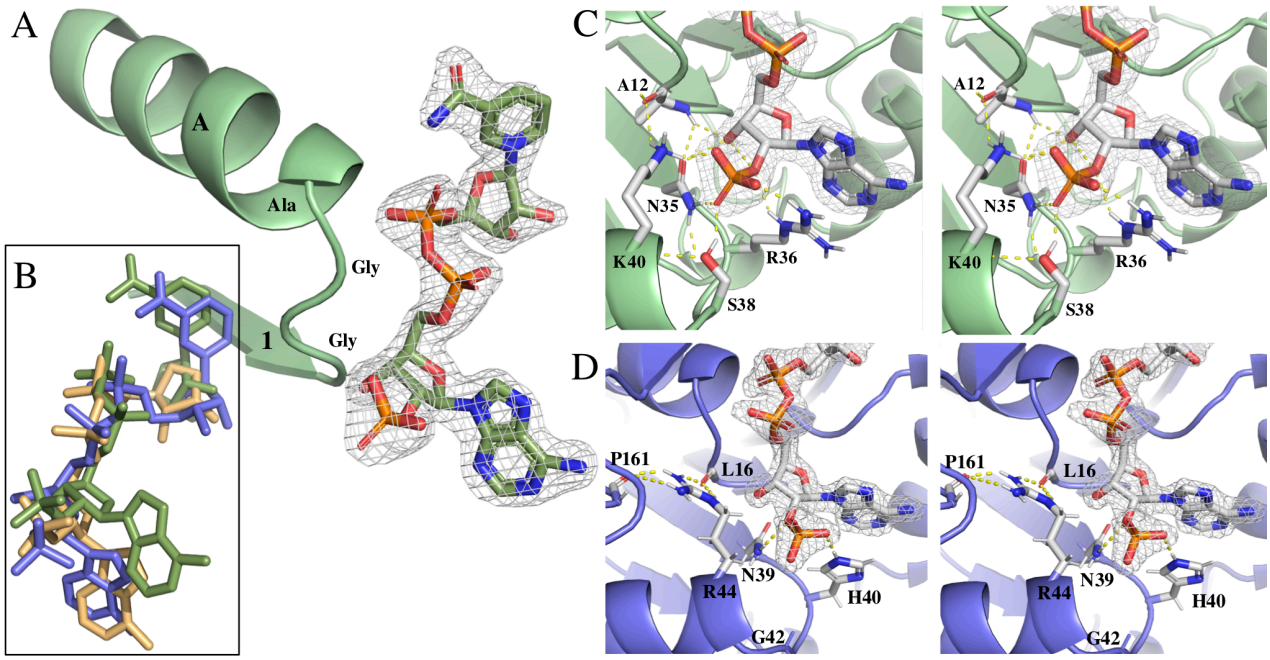

Figure 3-9. NAD(P)H Binding. YpODH electron density is displayed as $2mF_o$-DF_c simulated annealing omit map contoured at 1.5 σ and PaODH is displayed as mF_o-DF_c simulated annealing omit map contoured at 4.0 σ. **A)** YpODH bound to $NADP^+$. β1 and αA are connected by a loop in all three ODHs with the sequence GXGXXA. **B)** Overlay of $NADP^+$ from each species (Green – Yp, Blue – Pa, Yellow – Sa). SaODH has partial density for the nicotinamide ring which was left unmodeled. **C)** YpODH-$NADP^+$ Stereoview. The YpODH-$NADP^+$ 2' phosphate forms 5 hydrogen bonds with 4 amino acid side chains. **D)** PaODH-$NADP^+$ Stereoview. The PaODH-$NADP^+$ 2' phosphate forms 2 hydrogen bonds with 2 amino acid side chains.

Domain closure

The NAD(P)H and catalytic domains of all three ODHs are separated by a large central cleft with nominal dimensions of 30 Å x 16 Å x 16 Å. This place the hydrides of the nicotinamide ring 8.5 Å distant from the catalytic domain. Britton *et. al.* reported the ArODH structure as representing an open conformation and postulated that closure between the domains would be necessary for hydride transfer [33]. When describing the PmODH structures, Smits *et. al.* reported that both the open and closed forms had been captured [34]. They presented an open-form, NADH bound structure (PDB: 3C7A), and a closed-form, NADH/Arginine bound structure (PDB: 3C7C). A review of the PmODH models and electron density maps raises several concerns. First, each structure was crystallized with the C-terminal pentahistidine tag from a symmetry mate inserted into the cleft between the domains causing steric clash and preventing potential closed conformations. Second, these structures align with an rms deviation of 1.1 Å over 403 Cα residues and Dyndom [35] analysis suggests no dynamic motion between the domains which is evident by visual inspection (**Fig. 3-10A**).

Ketopantoate reductase (KPR) from *E. coli* represents a useful model for domain closure, and shows good structural homology with an rms deviation of 3.19 Å over 253 Cα residues when compared to YpODH. KPR reduces pantoate converting the ketone to an alcohol. When both NADPH and pantoate are bound, significant closure of the α-helical domain relative to the NAD(P)H binding domain is evident (calculated as 24° by Dyndom) (**Fig. 3-10B**). We would expect a similar closure (approximately 5 Å) to bring the nicotinamide ring in proximity to the catalytic domain. Unfortunately, we have not yet been successful in capturing a closed ODH structure and no significant domain motions are noted between the apo- and $NADP^+$-bound structures for YpODH (rmsd of 0.54 Å over 416 Cα residues) or SaODH (rmsd of 0.28 Å over 424 Cα residues).

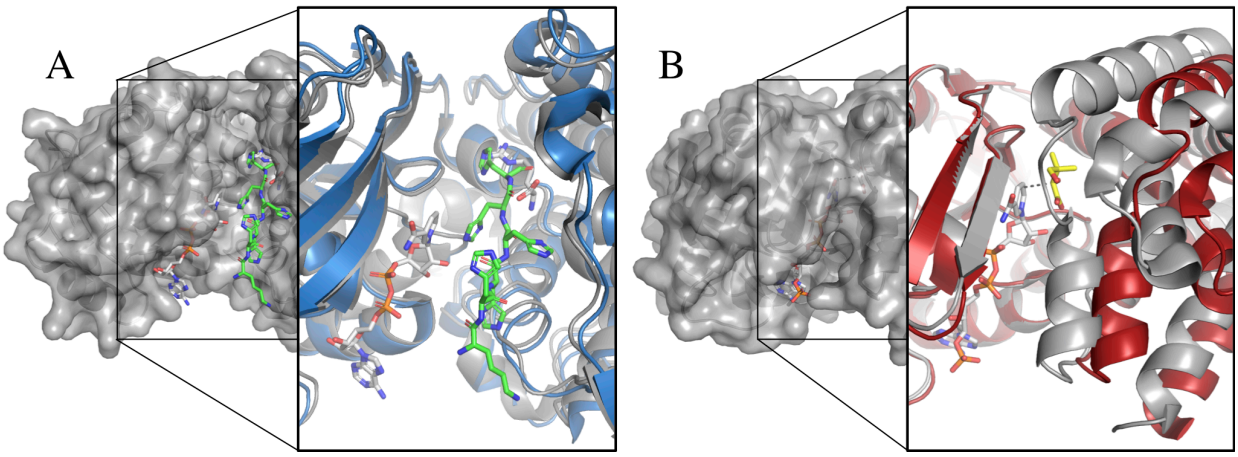

Figure 3-10. Domain Closure. A) Surface view - *Pecten maximus* ODH (PmODH) "closed form" (PDB: 3C7C) showing the active site cleft with NADH in white carbons and the pentahistidine tag in green carbons. Expanded view – ribbon diagram of PmODH "open form" active site (gray) overlaid with the "closed-form" (blue). Note the lack of conformational change indicating that both structures have open active sites. **B)** Surface view - *E. coli* ketopantoate reductase (KPR) (PDB: 2OFP) in a closed conformation with pantoate and NADPH bound. Expanded view - ribbon diagram overlay of KPR using the NADPH-binding domain for alignment. Holo form in gray, apo form in red (PDB: 1KS9). Ligands are NADPH (white) and pantoate (yellow). Dashed line is 3.3 Å. Holo form shows 24° closure of the catalytic domain as calculated by Dyndom.

Active Site

$NADP^+$ binds in a c-shaped cleft between the NAD(P)H-binding and catalytic domains (**Fig 3-11A**). The amide of the nicotinamide ring hydrogen bonds with T154 on β9 holding the ring in a *syn* conformation. A cavity adjacent to the nicotinamide ring is lined with amino acid residues largely conserved by YpODH, PaODH and SaODH producing a substrate binding site. The *syn* conformation of the nicotinamide projects the *pro*-S hydride into this space and would result in *pro*-S hydride transfer to the opine metallophore Schiff base intermediate consistent with octopine dehydrogenase [36, 37]. D153 is positioned above the hydrides of the nicotinamide ring and is conserved in SaODH. The carboxylate of D153 may electrostatically repel the carboxylate of α-ketoglutarate in YpODH and SaODH, while the A153 substitution found in PaODH allows, the longer, more negatively charged α-ketoglutarate to bind. R383 is conserved in all five structurally characterized ODHs. Smits *et al.* have suggested that the residue analogous to R383 in ArODH acts as a sensor for the NAD(P)H phosphates during domain closure, but we note that R383 has little or no density past the β carbon in any of the solved ODH structures (presented here or previously). We have modeled the side chain in a favorable rotameric conformation and we hypothesize that R383 acts to position and stabilize the α-keto acid substrate by coordinating its carboxylate.

Across from the nicotinamide ring is H242, which is hydrogen bonded to D388, both with well-defined electron density in all structures. His-Asp proton relays are common among dehydrogenases including lactate dehydrogenase [38] and glyceraldehyde-3-phosphate dehydrogenase [39]. Therefore, we propose that the histidine is positioned to act as a general acid/general base deprotonating the nucleophile and then donating the proton back to the 2-carbonyl oxygen leading to water release and Schiff base formation (**Fig 3-11B**). HisNA should be oriented with the imidazole moiety deep in the active site to confer stereoselectivity. This would place the primary amine of the amino butyrate proximal to the plane between the hydride and H242, positioning the substrate for nucleophilic attack. In our current structures, the nicotinamide

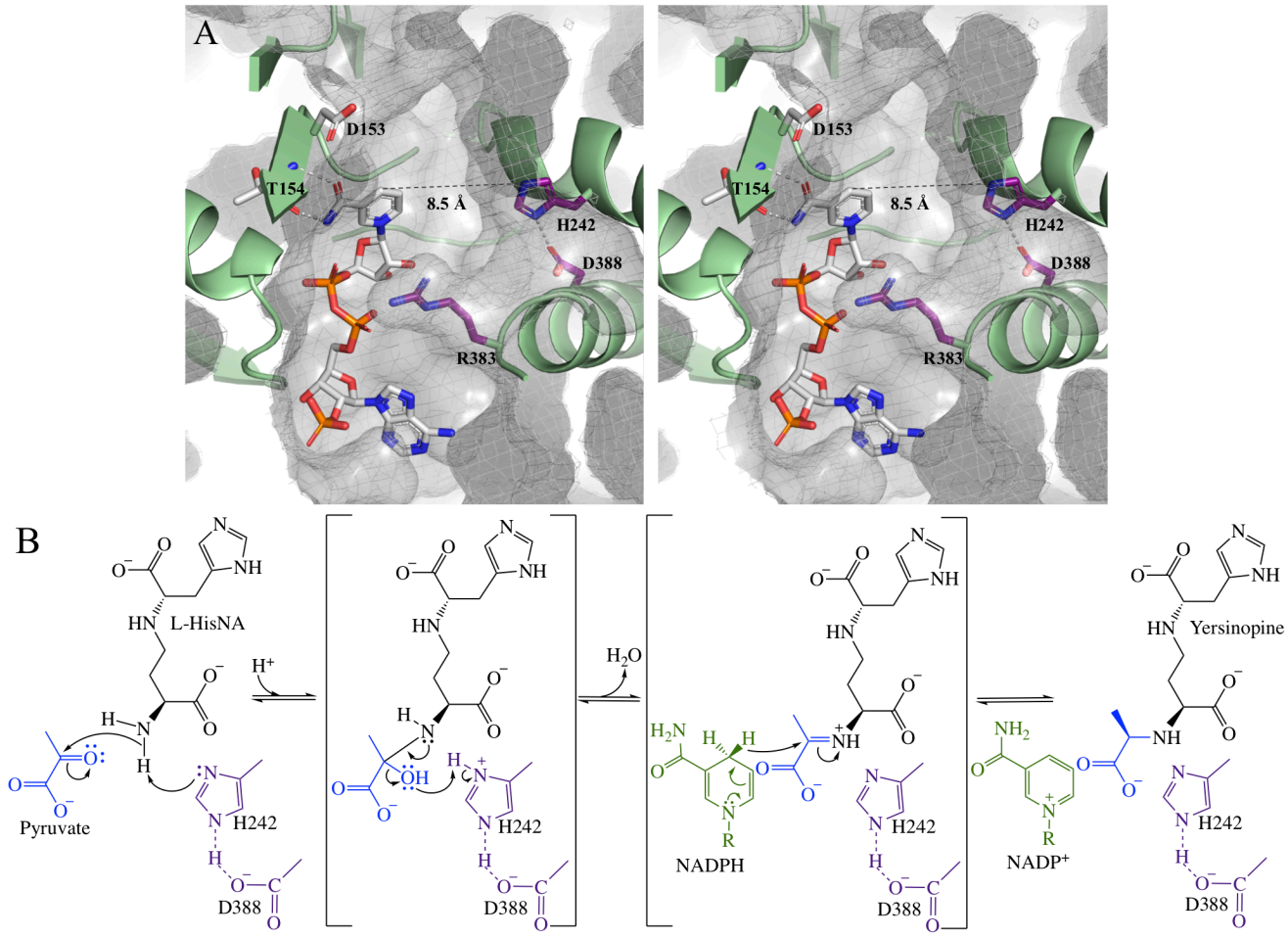

Figure 3-11. Active Site. A) Stereoview of YpODH-NADP$^+$ active site cavity with a CastP (computed atlas of surface topography of proteins) calculated surface. NADP$^+$– green carbons. Side chains conserved by YpODH, PaODH and SaODH – purple carbons. Side chains not conserved by YpODH, PaODH and SaODH – white carbons. **B)** Hypothetical mechanism for the condensation of pyruvate and L-HisNA by YpODH with H242 acting as the general acid, followed by reduction of the Schiff base by NADPH, leading to product formation.

ring hydride is 8.5 Å distant from the histidine proton, too far for catalysis and further supporting the necessity of domain closure.

Opine dehydrogenases can be categorized by the stereochemistry of their products [1]. ArODH, PmODH and their homologs produce opines with (R)-carboxyalkyl chiral centers [8, 40]. Saccharopine dehydrogenase and carboxyethyl ornithine dehydrogenase generate (S)-carboxyalkyl chiral centers [41]. YpODH, PaODH and SaODH have sequence and, indeed, structural homology with (R)-carboxylalkyl opine dehydrogenases. By contrast, saccharopine dehydrogenase (PDB: 3UH1) has an rmsd of only 5.3 Å over 96 Cα residues when compared with YpODH. While staphylopine has been synthesized with an (S)-carboxyalkyl chiral center by Toronto Research Chemicals [9] and as reported by Zhang *et. al.* [42], we propose that YpODH, PaODH and SaODH form (R)-carboxyalkyl opine metallophore products, given
their homology with (R)-carboxylalkyl opine dehydrogenases. It will be valuable to experimentally determine the full stereochemistry of the opine metallophores in future.

Yersinopine, pseudopaline and staphylopine dehydrogenase perform the final step in the production of three distinct opine metallophores. These enzymes share substantial structural homology, yet are able to distinguish differing substrate stereochemistry (L vs D-HisNA), differing α-keto acid length (pyruvate vs. α-ketoglutarate) and differing NAD(P)H substrates. Structural analysis reveals a dimeric assembly using secondary structure not conserved in previously documented opine dehydrogenases. Within the active site, R383 is expected to align substrate for Schiff base formation and hydride transfer, whereas D153 is predicted to function in α-keto acid substrate selection. H242 is positioned to act as a general acid/base promoting the formation of the Schiff base intermediate. The ODH structures determined were in an open conformation, but domain closure would be necessary to promote catalysis. The full stereochemistry of the opine metallophores is unknown, but structural homology with characterized opine dehydrogenases suggests that a (R)-carboxyalkyl opine is formed.

References

[1] Thompson, J., and Donkersloot, J. A. (1992) N-(Carboxyalkyl) Amino Acids: Occurence, Synthesis, and Functions, *Annu Rev Biochem 61*, 40.

[2] Van Thoai, N., and Robin, Y. (1959) Biosynthése de L'octopine et Répartition de L'enzyme L'opérant Chez Les Invertebrés, *Biochim Biophys Acta 35*, 446-453.

[3] Grieshaber, M. K., Hardeweig, I., Kreutzer, U., and Portner, H. O. (1994) Physiological and Metabolic Responses to Hypoxia in Invertebrates, *Rev. Physiol. Biochem. Pharmacol. 125*, 44-129.

[4] Moore, L. W., Chilton, W. S., and Canfield, M. L. (1997) Diversity of Opines and Opine-Catabolizing Bacteria Isolated from Naturally Occurring Crown Gall Tumors, *Appl Environ Microbiol 63*, 201-207.

[5] Watanabe, S., Sueda, R., Fukumori, F., and Watanabe, Y. (2015) Characterization of Flavin-Containing Opine Dehydrogenase from Bacteria, *PLoS One 10*, e0138434.

[6] Andi, B., Xu, H., Cook, P. F., and West, A. H. (2007) Crystal Structures of Ligand-Bound Saccharopine Dehydrogenase from Saccharomyces cerevisiae, *Biochemistry 46*, 12512-12521.

[7] Asano, Y., Yamaguchi, K., and Kondo, K. (1989) A New NAD^+-Dependent Opine Dehydrogenase from *Arthrobacter* sp. Strain 1C, *Journal of Bacteriology 171*, 4466-4471.

[8] Kato, Y., Yamada, H., and Asano, Y. (1996) Stereoselective synthesis of opine-type secondary amine carboxylic acids by a new enzyme opine dehydrogenase use of recombinant enzymes, *Journal of Molecular Catalysis 1*, 151-160.

[9] Ghssein, G., Brutesco, C., Ouerdane, L., Fojcik, C., Izaute, A., Wang, S. L., Hajjar, C., Lobinski, R., Lemaire, D., Richaud, P., Voulhoux, R., Espaillat, A., Cava, F., Pignol, D., Borezee-Durant, E., and Arnoux, P. (2016) Biosynthesis of a broad-spectrum nicotianamine-like metallophore in Staphylococcus aureus, *Science 352*, 1105-1109.

[10] McFarlane, J. S., and Lamb, A. L. (2017) Biosynthesis of an Opine Metallophore by Pseudomonas aeruginosa, *Biochemistry 56*, 5967-5971.

[11] Lhospice, S., Gomez, N. O., Ouerdane, L., Brutesco, C., Ghssein, G., Hajjar, C., Liratni, A., Wang, S., Richaud, P., Bleves, S., Ball, G., Borezée-Durant, E., Lobinski, R., Pignol, D., Arnoux, P., and Voulhoux, R. (2017) Pseudomonas aeruginosa zinc uptake in chelating environment is primarily mediated by the metallophore pseudopaline, *Scientific Reports 7*, 1-10.

[12] Grim, K. P., San Francisco, B., Radin, J. N., Brazel, E. B., Kelliher, J. L., Parraga Solorzano, P. K., Kim, P. C., McDevitt, C. A., and Kehl-Fie, T. E. (2017) The Metallophore Staphylopine Enables Staphylococcus aureus To Compete with the Host for Zinc and Overcome Nutritional Immunity, *MBio 8*, 1-16.

[13] Mastropasqua, M. C., D'Orazio, M., Cerasi, M., Pacello, F., Gismondi, A., Canini, A., Canuti, L., Consalvo, A., Ciavardelli, D., Chirullo, B., Pasquali, P., and Battistoni, A. (2017) Growth of Pseudomonas aeruginosa in zinc poor environments is promoted by a nicotianamine-related metallophore, *Mol Microbiol 106*, 543-561.

[14] Gi, M., Lee, K. M., Kim, S. C., Yoon, J. H., Yoon, S. S., and Choi, J. Y. (2015) A novel siderophore system is essential for the growth of Pseudomonas aeruginosa in airway mucus, *Sci Rep 5*, 1-15.

[15] Remy, L., Carriere, M., Derre-Bobillot, A., Martini, C., Sanguinetti, M., and Borezee-Durant, E. (2013) The Staphylococcus aureus Opp1 ABC transporter imports nickel and cobalt in zinc-depleted conditions and contributes to virulence, *Mol Microbiol 87*, 730-743.

[16] Hanses, F., Roux, C., Dunman, P. M., Salzberger, B., and Lee, J. C. (2014) Staphylococcus aureus gene expression in a rate model of infective endocarditis, *Genome Medicine 6*, 1-16.

[17] Damron, F. H., Oglesby-Sherrouse, A. G., Wilks, A., and Barbier, M. (2016) Dual-seq transcriptomics reveals the battle for iron during Pseudomonas aeruginosa acute murine pneumonia, *Sci Rep 6*, 39172.
[18] Bielecki, P., Puchalka, J., Wos-Oxley, M. L., Loessner, H., Glik, J., Kawecki, M., Nowak, M., Tummler, B., Weiss, S., and dos Santos, V. A. (2011) In-vivo expression profiling of Pseudomonas aeruginosa infections reveals niche-specific and strain-independent transcriptional programs, *PLoS One 6*, e24235.
[19] Bielecki, P., Komor, U., Bielecka, A., Musken, M., Puchalka, J., Pletz, M. W., Ballmann, M., Martins dos Santos, V. A., Weiss, S., and Haussler, S. (2013) Ex vivo transcriptional profiling reveals a common set of genes important for the adaptation of Pseudomonas aeruginosa to chronically infected host sites, *Environ Microbiol 15*, 570-587.
[20] Wiren, N. (1999) Nicotianamine Chelates Both FeIII and FeII Implications for Metal Transport in Plants, *Plant Physiol 119*, 1107-1114.
[21] Van Duyne, G. D., Standaert, R. F., Karplus, P. A., Schreiber, S. L., and Clardy, J. (1993) Atomic Structures of the Human Immunophilin FKBP-12 Complexes with FK506 and Rapamycin, *J Mol Biol 229*, 19.
[22] McPhillips, T. M., McPhillips, S. E., Chiu, H.-J., Cohen, A. E., Deacon, A. M., Ellis, P. J., Garman, E., Gonzalez, A., Sauter, N. K., Phizackerley, R. P., Soltis, S. M., and Kuhn, P. (2002) Blu-Ice and the Distributed Control System: software for data acquisition and instrument control at macromolecular crystallography beamlines, *Journal of Synchrotron Radiation 9*, 401-406.
[23] Kabsch, W. (2010) Xds, *Acta Crystallogr D Biol Crystallogr 66*, 125-132.
[24] Skubak, P., and Pannu, N. S. (2013) Automatic protein structure solution from weak X-ray data, *Nat Commun 4*, 2777.
[25] Winn, M. D., Ballard, C. C., Cowtan, K. D., Dodson, E. J., Emsley, P., Evans, P. R., Keegan, R. M., Krissinel, E. B., Leslie, A. G., McCoy, A., McNicholas, S. J., Murshudov, G. N., Pannu, N. S., Potterton, E. A., Powell, H. R., Read, R. J., Vagin, A., and Wilson, K. S. (2011) Overview of the CCP4 suite and current developments, *Acta Crystallogr D Biol Crystallogr 67*, 235-242.
[26] Emsley, P., Lohkamp, B., Scott, W. G., and Cowtan, K. (2010) Features and development of Coot, *Acta Crystallogr D Biol Crystallogr 66*, 486-501.
[27] Adams, P. D., Afonine, P. V., Bunkoczi, G., Chen, V. B., Davis, I. W., Echols, N., Headd, J. J., Hung, L. W., Kapral, G. J., Grosse-Kunstleve, R. W., McCoy, A. J., Moriarty, N. W., Oeffner, R., Read, R. J., Richardson, D. C., Richardson, J. S., Terwilliger, T. C., and Zwart, P. H. (2010) PHENIX: a comprehensive Python-based system for macromolecular structure solution, *Acta Crystallogr D Biol Crystallogr 66*, 213-221.
[28] Chen, V. B., Arendall, W. B., 3rd, Headd, J. J., Keedy, D. A., Immormino, R. M., Kapral, G. J., Murray, L. W., Richardson, J. S., and Richardson, D. C. (2010) MolProbity: all-atom structure validation for macromolecular crystallography, *Acta Crystallogr D Biol Crystallogr 66*, 12-21.
[29] Krissinel, E., and Henrick, K. (2004) Secondary-structure matching (SSM), a new tool for fast protein structure alignment in three dimensions, *Acta Crystallogr D Biol Crystallogr 60*, 2256-2268.
[30] Zhang, Y., and Skolnick, J. (2005) TM-align: a protein structure alignment algorithm based on the TM-score, *Nucleic Acids Res 33*, 2302-2309.
[31] Krissinel, E., and Henrick, K. (2007) Inference of macromolecular assemblies from crystalline state, *Journal of Molecular Biology 372*, 774-797.
[32] Dundas, J., Ouyang, Z., Tseng, J., Binkowski, A., Turpaz, Y., and Liang, J. (2006) CASTp: computed atlas of surface topography of proteins with structural and topographical mapping of functionally annotated residues, *Nucleic Acids Res 34*, W116-118.

[33] K.L. Britton, Y. A. a. D. W. R. (1998) Crystal structure and active site location of N-(1-D-carboxylethyl)-L-norvaline dehydrogenase, *Nature Structural Biology 5*, 9.
[34] Smits, S. H., Mueller, A., Schmitt, L., and Grieshaber, M. K. (2008) A structural basis for substrate selectivity and stereoselectivity in octopine dehydrogenase from Pecten maximus, *J Mol Biol 381*, 200-211.
[35] Girdlestone, C., and Hayward, S. (2016) The DynDom3D Webserver for the Analysis of Domain Movements in Multimeric Proteins, *J Comput Biol 23*, 21-26.
[36] Nambiar, K. P., Sauffer, D. M., Kolodziej, P. A., and Benner, S. A. (1983) A Mechanistic Basis for the Stereoselectivity of Enzymatic Transfer of Hydrogen from Nicotinamide Cofactors, *J Am Chem Soc 105*, 5886-5890.
[37] Biellmann, J. B., G; Olomucki, A. (1973) Sterochemistry of the hydrogen transfer to the coenzyme by octopine dehydrogenase, *FEBS Letters 32*, 3.
[38] Holbrook, J. J., Liljas, A., Steindel, S. J., and Rossmann, M. G. (1975) 4 Lactate Dehydrogenase, In *The Enzymes* (Boyer, P. D., Ed.), pp 191-292, Academic Press.
[39] Harris, J. I., and Waters, M. (1976) 1 Glyceraldehyde-3-phosphate Dehydrogenase, In *The Enzymes* (Boyer, P. D., Ed.), pp 1-49, Academic Press.
[40] Biellmann, J., Branlant, G., and Wallen, L. (1977) Stereochemistry of octopine and of its isomers and their enzymatic properties, *Bioorganic Chemistry 6*, 89-93.
[41] Thompson, J., and Miller, S. P. F. (1988) N6-(1-Carboxyethly)lysine Formation by Streptococcus lactis, *Journal of Biological Chemistry 263*, 2064-2069.
[42] Zhang, J., Wang, S., Bai, Y., Guo, Q., Zhou, J., and Lei, X. (2017) Total Syntheses of Natural Metallophores Staphylopine and Aspergillomarasmine A, *J Org Chem 82*, 13643-13648.

Chapter 4

Staphylopine and pseudopaline dehydrogenase catalyze reversible reactions and produce stereospecific metallophores

Introduction

Pseudopaline and staphylopine are metallophores produced by *Pseudomonas aeruginosa* and *Staphylococcus aureus*, respectively[1-3]. Both metallophores have been shown to chelate multiple transition metal ions that are then returned to the bacterial cell through dedicated transport pathways. This metal ion sequestering mechanism plays an important role in virulence in several infectious diseases[1, 4-7]. The biosynthesis of these metallophores requires a (S)-adenosyl-L-methionine-dependent aminoalkyltransferase, commonly known as a nicotianamine synthase or NAS (E.C. 2.5.1.43). The NAS links a single aminobutyrate moiety from (S)-adenosyl-L-methionine (SAM) with L-histidine (pseudopaline) or D-histidine (staphylopine; D-histidine is made from L-histidine via a racemase encoded by the staphylopine operon[8]). We have termed this product L- or D-HisNA with the NA referring to nicotianamine. In the second step, an NAD(P)H-dependent oxidoreductase (E.C. 1.5.1.52) known as an opine dehydrogenase (abbreviated PaODH for *P. aeruginosa* and SaODH for *S. aureus*) performs a condensation of the HisNA substrate with an α-keto acid (α-ketoglutarate, PaODH; pyruvate, SaODH) forming a Schiff base intermediate that is reduced by hydride transfer from NAD(P)H (**Figure 4-1A**). The term opine is historical, being derived from the common name octopine, a compound identified in *Octopus octopodia* muscle tissue in 1927[9]. Opines are compounds formed enzymatically by condensation of an amino acid and a α-keto acid. We have termed the products of these reactions opine metallophores given that they are not true nicotianamines, which incorporate three aminobutyrate moieties from SAM, and because the final enzymatic step forms an opine compound. Pseudopaline and staphylopine are representative of this metallophore class, though many other species possess the biosynthetic machinery to make opine metallophore variants[6].

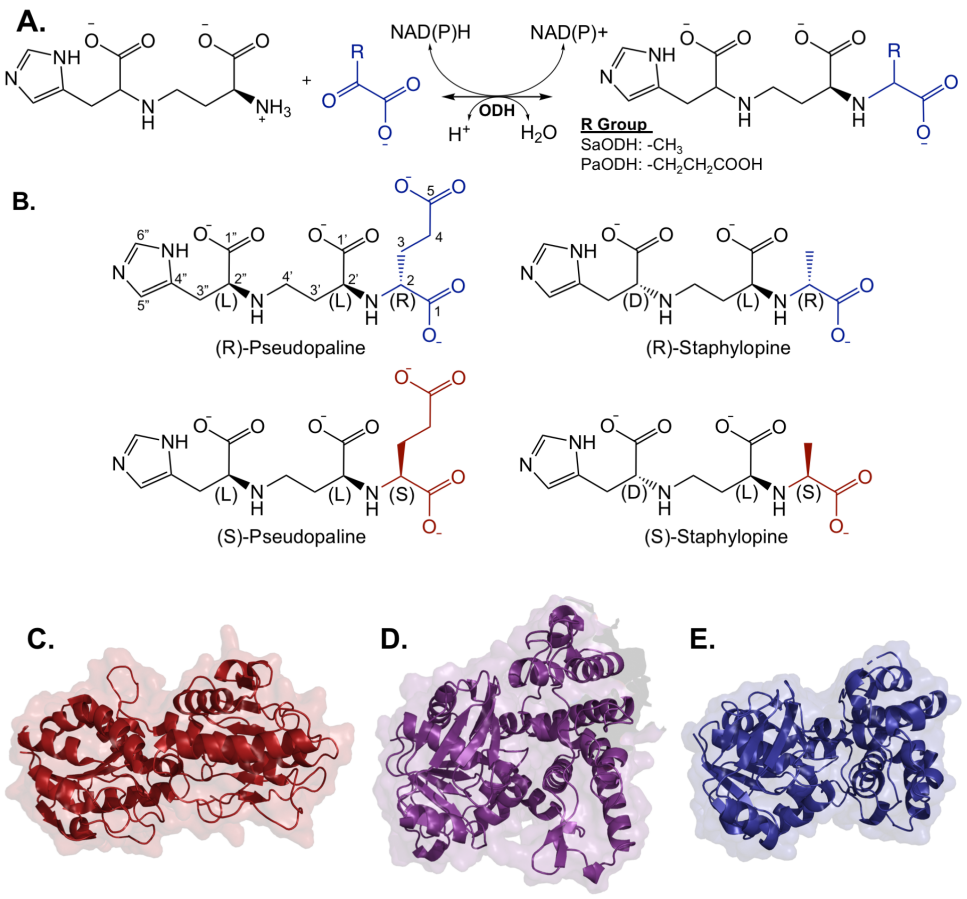

Figure 4-1. ODH reaction and product stereochemistry. A) Generalized opine metallophore-forming opine dehydrogenase reaction that condenses HisNA and an α-keto acid forming a Schiff base that is reduced by NAD(P)H. **B)** Opine metallophores. The stereo centers derived from amino acids are labeled (L) or (D) to distinguish them from the stereocenter formed by the opine dehydrogenase which is labeled (S) or (R). Numbering for the carbons of (R)-pseudopaline is used to identify specific carbons in the structural studies presented below. **C)** Saccharopine dehydrogenase (PDB: 3UH1) contains two Rossmann-like fold domains. Characterized members of this enzyme class produce (S)-opine products. PDBeFold calculates a 4.8 Å rmsd over 28% of the Cα residues in comparison to PaODH-NADP$^+$ (Panel D). **D)** Pseudopaline dehydrogenase (PaODH-NADP$^+$, PDB: 6PBM) is structurally homologous with (R)-opine and not (S)-opine ODHs such as N$^\alpha$-[1-(R)-(carboxyl)ethyl]-(L)-norvaline dehydrogenase (Panel E). **E)** N$^\alpha$-[1-(R)-(carboxyl)ethyl]-(L)-norvaline dehydrogenase (PDB: 1BG6). Characterized members of this

enzyme class produce (R)-opine products. PDBeFold calculates a 3.4 Å rmsd over 91% of the Cα residues, in comparison to PaODH-$NADP^+$.

Although the chemical composition of pseudopaline and staphylopine has been confirmed by both *in vitro*[1-3] and *in vivo*[1, 3, 10] experiments, the stereochemistry formed upon nucleophilic attack at the prochiral carbon of the α-keto acid has not been determined. Production of either the (R) or (S) diastereomer at this position is possible (**Figure 4-1B**). Opine dehydrogenases exist in two structural classes. One class is composed of enzymes with two Rossmann-like fold domains (ex. PDB: 3UH1) that form (S) opines upon reduction of the Schiff base. The other class is composed of enzymes with one Rossmann-like fold domain and one α-helical domain and produce (R) opines (**Figure 4-1C-E**). Indeed, the use of *Arthrobacter sp.* Strain 1C opine dehydrogenase, which stereoselectively produces the (R) opine N^{α}-[1-(R)-(carboxyl)ethyl]-(L)-norvaline, by condensing pyruvate and (L)-norvaline[11], is the subject of a U.S. patent[12] proposing the use of this enzyme to generate chiral secondary amines for pharmaceutical development. Full knowledge of opine metallophore stereochemis-try is important as it is likely to influence receptor recognition as well as the coordination geometry for metal complexes. This is especially important for pseudopaline, because it incorporates an extra carboxylate ligand from α-ketoglutarate. As both PaODH and SaODH belong to the (R) opine producing structural class, we have proposed that they produce (R) opine metallophores[13].

We hypothesized that PaODH and SaODH catalyze reversible reactions that specifically produce the (R) opine metallophore diastereomer. The reverse reaction would therefore use only one opine metallophore diastereomer as a substrate. In this study, we measure catalysis in the steady-state for the reverse reactions of PaODH and SaODH using both the (R) and (S) diastereomers of pseudopaline and staphylopine. We also present four X-ray crystal structures of PaODH with ligands bound. PaODH-$NADP^+$ (1.57 Å, 0.4 Å higher resolution than our previously deposited structure) has $NADP^+$ bound. PaODH-(S)-Pse (1.64 Å) has $NADP^+$ and (S)-pseudopaline bound. PaODH-(R)-Pse-1hr (1.65 Å) was crystallized with $NADP^+$ and soaked with (R)-pseudopaline, but has density for NADP+, L-HisNA and partial density for α-ketoglutarate.

PaODH-(R)-Pse-2hr (2.18 Å) was crystallized with $NADP^+$ and soaked with (R)-pseudopaline. This structure only has electron density for the $NADP^+$ and L-HisNA ligands suggesting catalysis and release of α-ketoglutarate within the crystal. Together these data define the amino acid residues involved in binding pseudopaline and support the hypothesis that PaODH and SaODH are stereoselective in the formation of the Schiff base intermediate and subsequent hydride transfer resulting in an (R) stereocenter for C2 (**Figure 4-1B**) of the respective α-keto acid. This results in (R)-pseudopaline or (R)-staphylopine products, respectively.

The kinetic mechanism for opine dehydrogenases is best understood for octopine dehydrogenase, an enzyme that was the subject of extensive study by Anna Olomucki and colleagues during the 1970s. They noted a burst phase preceding steady-state turnover at high substrate concentrations that was lost as substrate concentration dropped near the K_m value. They concluded that hydride transfer was not rate-limiting and that the enzyme most likely proceeded through an ordered-sequential mechanism with NAD(P)H binding first and $NADP^+$ dissociating last[14-15]. SaODH and PaODH have only been examined by steady-state methods that typically mask key steps in the catalytic cycle[16]. Here we use stopped-flow spectrometry to conduct transient state kinetic assays of staphylopine dehydrogenase for both the forward and reverse reactions observing absorption and fluorescence characteristics of the NADPH dihydronicotinamide ring. Absorption data reveal a reaction that is substantially slower in the steady-state than during the first turnover and fluorescence data suggest that this is due to a slow product release step for the forward reaction. It has recently been proposed that SaODH binds divalent transition metals such as Zn(II), Cu(II), Co(II) and Ni(II) resulting in an inhibition of staphylopine production[17]. It was further proposed that SaODH activity is enhanced at low concentrations of Zn(II) or Cu(II) due to preferred catalysis of D-HisNA when coordinated by these two metals. We tested this hypothesis in the transient state and found that the inhibition is due to

sequestration of available D-HisNA substrate by metal ion chelation and not due to direct inhibition of the enzyme and also found no evidence of rate enhancement in the presence of Zn(II) or Cu(II).

Methods

Protein expression and purification

SaODH and PaODH were purified as previously described[2] with the following modification. For the purification of PaODH, 1 mM octyl β-D-glucopyranoside (BOG) was added to the buffers for both the nickel affinity and size exclusion chromatography purification steps. 1 mM dithiothreitol (DTT) was added to the buffer for the size exclusion chromatography step. Protein concentration was determined by absorbance at 280 nm using the method of Pace *et. al*[18]. Previously, we used the Bradford assay to determine concentration for PaODH and SaODH, but global fitting of single turnover reactions revealed these values to be artificially high. Absorbance at 280 nm gives a concentration lower than by Bradford assay by a factor of 6.7 for both enzymes. Multiplying our previously published k_{cat} values[13] by this factor gives corrected k_{cat} and k_{cat}/K_m values.

Reagents and reaction buffer

Sodium pyruvate, NADPH and $NADP^+$ were obtained from Sigma. (R) and (S)-staphylopine, (R) and (S)-pseudopaline, D-HisNA and L-HisNA were prepared as described previously[10, 19]. Purified SaODH was stored at a concentration of 50 μM in a buffer containing 50 mM potassium phosphate pH 8.0, 100 mM sodium citrate and 20% glycerol. All transient state and steady state experiments were performed using rapid mixing with a Hi-Tech stopped-flow spectrometer (TgK Scientific). In all subsequent descriptions, we report only the final concentrations in the stopped-flow cell after mixing. SaODH was first diluted to 30 μM using reaction buffer (50 mM Tris pH 8.0) giving a concentration of 12% glycerol. Upon mixing in the stopped-flow cell, the final concentration of glycerol was diluted to 6%.

Steady-state kinetics of the reverse reaction

Initial rates were measured by observing $NADP^+$ reduction as an increase in absorbance at 340 nm using a stopped-flow spectrometer at 24 °C. The reaction buffer was 50 mM Tris pH 8.0 (SaODH) or 50 mM potassium phosphate pH 8.0 (PaODH). 300 nM ODH and 224 μM $NADP^+$ were combined in one syringe and mixed 1:1 with a second syringe containing varied concentrations of either (R)- or (S)-staphylopine (*S. aureus*) or (R)- or (S)-pseudopaline (*P. aeruginosa*). To determine kinetic parameters, plots of initial rates were fit to the Michaelis-Menten equation modified to account for the observed substrate inhibition.

Eq. 1 $$v_o = \frac{v_{max}[S]}{K_m + [S] + \left(\frac{[S]^2}{K_i}\right)}$$

Each experiment was repeated at least three times and error was calculated as the standard deviation of the parameters determined from each trial.

NADPH binding by fluorescence

The binding of NADPH to SaODH was measured as an increase in fluorescence emission at 450 nm on a stopped-flow spectrometer at 24 °C using a WG360 longpass cut-off filter. SaODH was mixed with NADPH in the stopped-flow cell to give final concentrations of 15 μM SaODH and 2.5 μM to 80 μM NADPH. Fluorescence emission was measured for 10 s in logarithmic timescale mode. Fluorescence intensity was corrected to account for the inner filter effect caused by increasing concentrations of NADPH using the following equation[20]:

Eq. 2 $$F_c = F * 10^{\frac{\varepsilon c}{2}}$$

where F_c is the corrected intensity for fluorescence (F), ε is the extinction coefficient of NADPH at the excitation wavelength of 340 nm (6220 $M^{-1}cm^{-1}$), and c is the concentration of NADPH. Duplicate data sets were collected, averaged and fit to a one-step equilibrium binding model using numerical integration in Kintek Explorer 8.0[21-22]. Fit was evaluated by FitSpace using a Chi^2 threshold limit of 0.91 from a data set with 10,240 data points. The original data and optimized simulations were replotted in Kaleidagraph.

Transient state kinetics of the forward reaction

Reaction progress in the transient state was followed as NADPH was oxidized to $NADP^+$ at 24 °C using the stopped-flow spectrometer by measuring the loss of absorbance at 340 nm or the loss of total fluorescence emission beyond a 360 nm cutoff filter. SaODH was mixed in one step with all three substrates. For reactions measuring the rate of absorption change with varied D-HisNA, the concentrations were 15 μM SaODH, 1 mM pyruvate and 160 μM NADPH with D-HisNA varied from 7.8 to 62.5 μM. For reactions measuring the rate of absorption change with varied pyruvate, the concentrations were 15 μM SaODH, 500 μM D-HisNA and 160 μM NADPH with pyruvate varied from 3.9 to 4000 μM. Concentrations for reactions measuring the rate of fluorescence change in the forward direction were 15 μM SaODH, 500 μM D-HisNA and 1 mM pyruvate with NADPH varied from 5 to 240 μM. In each experiment, data were collected for 100 s using logarithmic time-base mode. Data fitting was performed in Kintek Explorer 8.0[21-22] using numerical integration and kinetic models accounting for the conversion of D-HisNA (D) and NADPH (N) to staphylopine (S) and $NADP^+$ (N^+):

Model 1:

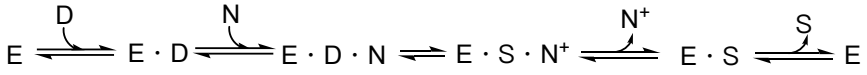

Model 2:

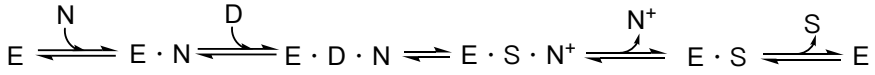

The model did not require a step for the addition of pyruvate to fit the data, suggesting pyruvate binding was rapid and that 1 mM was saturating. Rate constants determined from the NADPH binding data were used to constrain the model, with k_{off} = 26.9 s^{-1} ± 5 and k_{on} = 0.38 $M^{-1}s^{-1}$ x 10^6 ± 0.1 x 10^6. Error was calculated from the upper and lower boundaries from data fitting as evaluated in the Fitspace routine. The original data and optimized simulations were replotted in Kaleidagraph.

Transient state kinetics of the reverse reaction

Reaction progress in the transient state for the reverse reaction was followed by observing the increase in total fluorescence emission beyond 360 nm as a result of production of NADPH at 24 °C using the stopped-flow spectrometer. SaODH was mixed with (R)-staphylopine and $NADP^+$. The concentrations of reactants were 15 μM SaODH, 125 μM (R)-staphylopine and varied $NADP^+$ from 2.5 to 40 μM or 15 μM SaODH, 150 μM $NADP^+$ and varied (R)-staphylopine from 5 to 40 μM. In both experiments, data were collected for 100 s in logarithmic time-base mode.

Transient state fluorescence measurements of the reverse reaction are subject to inner filter from NADPH accumulation. We addressed this by enabling scaling factors for each concentration during global data fitting. Data fitting was performed in Kintek Explorer 8.0 using the model and constraints described above. Data for both varied $NADP^+$ and varied (R)-staphylopine were fit simultaneously to this model. The original data and optimized simulations were replotted in Kaleidagraph.

The source of metal inhibition by zinc(II), copper(II), nickel(II) and cobalt(II)

Transient state kinetic assays were performed by measuring absorbance at 340 nm as described above. Cobalt(II) chloride, copper(II) chloride, zinc(II) chloride, or nickel(II) chloride were preincubated with either SaODH or with D-HisNA at room temperature for five minutes prior to initiating the reaction. In each experiment, SaODH was combined with NADPH and pyruvate in one syringe and mixed with D-HisNA from another syringe. For reactions with metal ion preincubated with D-HisNA, the concentrations were 15 μM SaODH, 1 mM pyruvate, 180 μM NADPH and metal ion varied from 12.5 to 100 μM (Cu(II) and Ni(II)) or 6.3 to 100 μM (Co(II) and Zn(II)), and D-HisNA at 100 μM. For reactions with metal ion pre-incubated with SaODH, the concentrations were 15 μM SaODH, 1 mM pyruvate, 180 μM NADPH, 25 μM metal ion (Co(II)) or 50 μM metal ion (Cu(II), Ni(II) and Zn(II)), and 100 μM D-HisNA (Cu(II), Ni(II) and Zn(II)) or 6.3 to 100 μM D-HisNA (Co(II)). Negative controls without added metal ions were performed for each experiment. Each experiment was performed twice with representative examples shown.

Data for SaODH pre-incubated with Co(II) at D-HisNA concentrations from 0 μM to 25 μM were fit in Kintek Explorer to model 1 described above with the addition of a separate one-step equilibrium to account for the binding of D-HisNA by Co(II). Data for Co(II) pre-incubated with D-HisNA were also fit analytically in Kintek Explorer 8.0 to equations for exponential decay:

Eq. 3 $$[S] = \Delta S_1 \cdot e^{-k_1 \cdot t} + S_{final}$$

Eq. 4 $$[S] = \Delta S_1 \cdot e^{-k_1 \cdot t} + \Delta S_2 \cdot e^{-k_2 \cdot t} + S_{final}$$

These analytical fits do not define intrinsic rate constants for reaction steps; they were used to qualitatively compare rates from different experiments. Data and fits were replotted in Kaleidagraph.

Protein Crystallization

All crystals were grown in hanging drops composed of 1.5 μL protein and 1.5 μL well solution at 24 °C. PaODH at 1.2 mg/mL, with its N-terminal hexahistidine tag, was supplemented with 2 mM $NADP^+$ prior to crystallization for all structures. PaODH-$NADP^+$ crystallized in a well solution of 100 mM BisTris pH 5.45, 200 mM ammonium acetate, and 24% PEG 3350. PaODH-(S)-Pse crystallized in a well solution of 290 mM ammonium formate, and 28% PEG 3350. PaODH-(R)-Pse-2hr crystallized in a well solution of 270 mM ammonium formate, and 28% PEG 3350. PaODH-(R)-Pse-1hr crystallized in a well solution of 260 mM ammonium formate, and 25% PEG 3350. In each condition, rod-shaped crystals grew within two days and reached maximum size within two weeks. Crystals were transferred into a cryoprotectant made by supplementing well solution with 20% ethylene glycol and 2 mM $NADP^+$ for PaODH-$NADP^+$; 25% ethylene glycol, 2 mM $NADP^+$ and 10 mM (S)-pseudopaline for PaODH-(S)-Pse; and 25% ethylene glycol, 2 mM $NADP^+$ and 10 mM (R)-pseudopaline for PaODH-(R)-Pse-1hr or 20 mM (R)-pseudopaline for PaODH-(R)-Pse-2hr. PaODH-(S)-Pse crystals were soaked for one hour in their cryoprotectant solution containing 10 mM (S)-pseudopaline prior to flash cooling. PaODH-(R)-Pse-1hr crystals were soaked for one hour in their cryoprotectant solution containing 10 mM (R)-pseudopaline

prior to flash cooling. PaODH-(R)-Pse-2hr crystals were soaked for two hours in their cryoprotectant solution containing 20 mM (R)-pseudopaline prior to flash cooling.

Data Collection and Structure Determination

Diffraction data were collected remotely using BluIce[23] at the Stanford Synchrotron Radiation Lightsource (SSRL, Menlo Park, CA). For all structures, 360° of data with 0.15° oscillation were collected at a temperature of 100 °K. Statistics for data collection and refinement are listed in **Table 4-1**. Data were processed in XDS [24]. PaODH-$NADP^+$ data were collected on beamline 12-2 at a wavelength of 0.9795 Å and 0.2 s exposure with a detector distance of 325 mm. These data were processed to 1.57 Å. PaODH-(S)-Pse data were collected on beamline 9-2 at a wavelength of 0.9795 Å and 0.31 s exposure with a detector distance of 320 mm. These data were processed to 1.64 Å. PaODH-(R)-Pse-1hr data were collected on beamline 9-2 at a wavelength of 0.9795 Å and 0.2 s exposure with a detector distance of 320 mm. These data were processed to 1.65 Å. PaODH-(R)-Pse-2hr data were collected on beamline 9-2 at a wavelength of 0.9795 Å and 0.2 s exposure with a detector distance of 470 mm. These data were processed to 2.18 Å. Our previously deposited PaODH structure (PDB: 6C4N) was used as a search model for molecular replacement in phenix.phaser[25]. The two monomers from the 6C4N dimer were used as separate models in the search, placing one of each. The resulting solution had a LLG = 9,098 and a TFZ = 68.8 for PaODH-$NADP^+$, a LLG = 19,571 and a TFZ = 128.9 for PaODH-(S)-Pse, a LLG = 24,434 and a TFZ = 141.8 for PaODH-(R)-Pse-1hr, and a LLG = 13,989 and a TFZ = 107.8 for PaODH-(R)-Pse-2hr. For each structure, rounds of model building and refinement were completed in Coot[26] and phenix.refine[27]. Waters were placed by phenix.refine, corrected manually and verified, using a 2m*Fo-DFc* electron density map contoured at 1.5 σ, following a round of refinement. Density was visible for $NADP^+$ (all four structures), (S)-pseudopaline (PaODH-(S)-Pse), or L-HisNA (PaODH-(R)-Pse-1hr and 2hr) in the initial electron density map.

Table 4-1 Data collection and refinement statistics

	PaODH-NADP$^+$	PaODH-(S)-Pse	PaODH-(R)-Pse-1hr	PaODH-(R)-Pse-2hr
Data collection				
PDB ID	6PBM	6PBP	6PBN	6PBT
Spacegroup	C2	C2	C2	C2
Unit cell (Å, °)	a=180.9 b=53.9 c=96.9 β=99.1	a=180.6 b=53.8 c=96.8 β=98.7	a=181.0 b=53.8 c=96.9 β=98.8	a=181.6 b=53.9 c=96.9 β=98.8
Resolution range (Å)	38.3 - 1.57	39.9 – 1.64	40.0 - 1.65	39.8 - 2.18
Completeness (%)	98.0 (95.9)	97.1 (88.0)	98.5 (88.0)	97.9 (88.6)
Total reflections	876,519	757,987	753,247	324,135
Unique reflections	126,487	110,264	110,062	48,004
I / σ	10.2 (2.0)	12.8 (2.0)	12.9 (2.0)	11.5 (2.3)
R_{merge}[a]	9.4 (79.4)	8.1 (69.5)	7.2 (69.3)	12.0 (71.9)
R_{pim}[b]	5.7 (51.8)	5.0 (47.4)	4.5 (46.8)	7.5 (54.3)
Multiplicity	6.9 (6.3)	6.9 (5.7)	6.8 (5.7)	6.8 (5.1)
Refinement				
Resolution range (Å)	38.3-1.57	39.9 - 1.64	40.0 - 1.65	38.4 - 2.18
No. of reflections	126,475	110,120	110,060	47,989
R_{work} / R_{free}[c]	16.5/18.1	17.0 / 20.0	17.5 / 20.8	17.5 / 22.7
No. atoms				
Non-hydrogen	7299	7499	7379	6925
Protein	6625	6612	6605	6593
Ligand/ion	132	182	144	122
Water	542	705	626	210
Ramachandran favored (%)	98.6	98.7	98.9	98.9
Ramachandran outliers (%)	0.0	0.0	0.0	0.0
Wilson *B*	17.7	15.3	18.2	27.5
Average *B* (Å^2)	22.8	19.3	22.8	33.9
Protein	22.2	18.6	22.0	34.0
Ligand/ion	25.5	18.3	26.0	37.2
R.m.s. deviations				
Bond lengths (Å)	0.011	0.011	0.013	0.014
Bond angles (°)	1.15	1.11	1.17	1.31

All data were collected on beamline 12-2 or 9-2 at the Stanford Synchrotron Radiation Lightsource. Values in parentheses are for the highest resolution shells.

[a] $R_{merge} = \sum_{hkl}|I_{hkl} - \langle I\rangle_{hkl}|/\sum_{hkl} I_{hkl}$ where I_{hkl} is the intensity of reflection *hkl* and $\langle I\rangle$ is the mean intensity of related reflections.

[b] $R_{pim} = \sum_{hkl}\sqrt{1/n-1}\,|I_{hkl} - \langle I\rangle_{hkl}|/\sum_{hkl} I_{hkl}$ where n is the multiplicity of related reflections.

[c] $R = \sum\left|F_o - |F_c|\right| / \sum|F_o|$ where F_o = the observed structure factors and F_c = structure factors calculated from the model. 5% of the reflections were initially reserved to create an R_{free} test set used during each subsequent round of refinement.

L-HisNA and α-ketoglutarate density became more apparent through refinement for both PaODH-(R)-Pse structures. Ligands were placed after polypeptide refinement was complete. $NADP^+$ was added to each model by phenix.ligandfit. (S)-pseudopaline and L-HisNA were built in phenix.elbow. (S)-pseudopaline was placed in PaODH-(S)-Pse by phenix.ligandfit with CC values of 83.5 and 88.2 for chain A and B respectively. L-HisNA and α-ketoglutarate were placed by hand in chain A of PaODH-(R)-Pse-1hr, using restraints generated in phenix.elbow. L-HisNA was placed in PaODH-(R)-Pse-2hr by phenix.ligandfit in chain A with a CC value of 77.5. Density for L-HisNA is also visible in chain B for both PaODH-(R)-Pse structures, but is fragmented and was not modeled. Ligand placement was verified following a round of refinement and by generating omit maps and Polder maps in phenix with (S)-pseudopaline, L-HisNA and/or α-ketoglutarate omitted from the respective model.

Crystallographic models

Summary data for the models is provided in **Table 4-2**. Ramachandran analysis was performed by MolProbity [28] showing good geometry with no outliers for each structure. A comparison of structures and calculation of rmsd values were performed using PDBeFold[29]. Solvent accessible surface was calculated by CASTp (Computed Atlas of Surface Tomography of proteins)[30]. Structure figures were generated in PyMOL (The PyMOL Molecular Graphics System, Version 2.0 Schrödinger, LLC.). The atomic coordinates and structure factors have been deposited in the Protein Data Bank (accession codes in **Table 4-2**).

Results

SaODH and PaODH catalyze reversible reactions

We hypothesized that SaODH and PaODH would catalyze reversible reactions and that both enzymes would exclusively form the (R) product diastereomer, consistent with structurally homologous opine dehydrogenases[31-33]. To test this hypothesis, (R)- and (S)-pseudopaline and (R)- and (S)-staphylopine were synthesized as previously described[10, 19]. SaODH or PaODH were

Table 4-2 Model Components

Protein	PDB Code	ASU[a]	Ordered Residues	Ligands
PaODH-$NADP^+$	6PBM	2	Chain A: 6-431 Chain B: 7-431	2 $NADP^+$
PaODH-(S)-Pse	6PBP	2	Chain A: 7-431 Chain B: 7-431	2 $NADP^+$ 2 (S)-Pse
PaODH-(R)-Pse-1hr	6PBN	2	Chain A: 7-431 Chain B: 7-431	2 $NADP^+$ 1 L-HisNA 1 α-KG[b]
PaODH-(R)-Pse-2hr	6PBT	2	Chain A: 7-431 Chain B: 7-431	2 $NADP^+$ 1 L-HisNA

[a] number of monomers in the asymmetric unit
[b] α-KG is α-ketoglutarate

combined with $NADP^+$ and then mixed with varied concentrations of (R)- or (S)-staphylopine (SaODH) or (R)- or (S)-pseudopaline (PaODH) (**Figure 4-2**). Substantial inhibition was observed at concentrations above ~25 μM (R)-pseudopaline or (R)-staphylopine (**Table 4-3**). NADPH oxidation with (S)-pseudopaline as the varied substrate was, within error, zero at all concentrations (**Figure 4-2B**). (S)-staphylopine resulted in limited catalysis with a k_{cat} of 0.02 s^{-1}, four-fold above the rate of NADPH oxidation in the absence of opine metallophore in this assay (0.005 s^{-1}) (**Figure 4-2B**). Reverse reactions initiated with (R)-staphylopine or (R)-pseudopaline showed steady-state turnover with k_{cat} values approximately 40% of the previously published forward rates[13]. These data indicate that both SaODH and PaODH catalyze reversible reactions consistent with other characterized opine dehydrogenases such as octopine dehydrogenase from *Pecten maximus*[32]. Importantly, both enzymes specifically catalyze the reverse reaction with the (R)-diastereomer of their respective product. This provides definitive evidence that the opine product of the forward reaction is the (R)-opine metallophore.

PaODH binds (S)-pseudopaline in a non-catalytic complex

PaODH crystals were grown in the presence of $NADP^+$ and L-HisNA, (S)-pseudopaline or (R)-pseudopaline. While $NADP^+$ electron density was observed in each case, no substantial additional ligand density was visible in any of the structures, and thus they are not reported here. Co-crystals with 2 mM $NADP^+$ were also grown and soaked for increasing lengths of time with varied concentrations of either substrate or product. Structures co-crystallized with $NADP^+$ in which L-HisNA was soaked (for up to 18 hours) had no density for L-HisNA. However, a structure determined from a crystal grown with $NADP^+$ and soaked for one hour with 10 mM (S)-pseudopaline (PaODH-(S)-Pse) had clear density for both $NADP^+$ and (S)-pseudopaline immediately following molecular replacement. The comparison of this structure to a structure of PaODH grown with 2 mM $NADP^+$ revealed that the two structures are ostensibly identical with a 0.36 Å rmsd for 848 residues (the full length of the dimer). The few differences that are observed are for residues and loops surrounding the active site as described below.

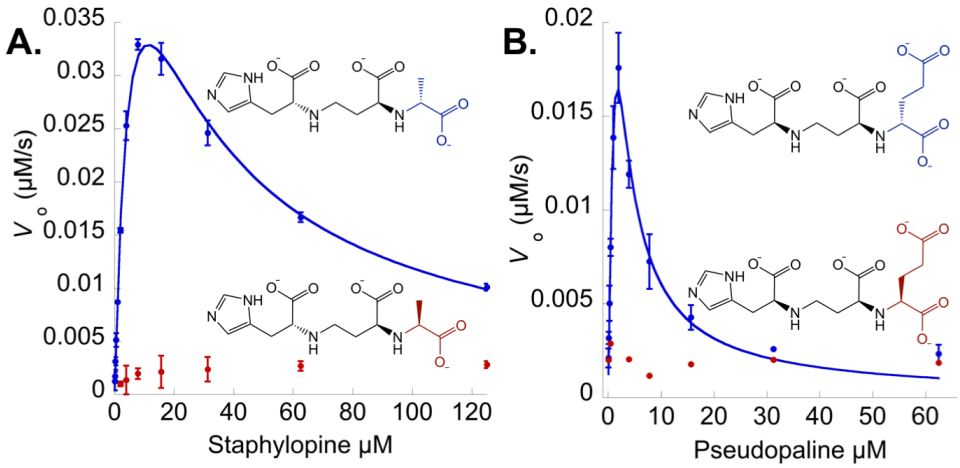

Figure 4-2. Steady-state kinetic plots for the reverse reaction. Final concentrations were 150 nM SaODH (A) or PaODH (B) and 112 µM $NADP^+$ mixed with varied concentrations of (R)- or (S)-staphylopine or (R)- or (S)-pseudopaline. **A)** Dependence of the initial rate for (R)-staphylopine (blue, fit to Eq. 1) and (S)-staphylopine (red). Structural formulas for staphylopine accompany each plot. **B)** Secondary plots of initial rates for (R)-pseudopaline (blue, fit to Eq. 1) and (S)-pseudopaline (red). Structural formulas for pseudopaline accompany each plot.

Table 4-3. Steady-state kinetic parameters

Initiating	k_{cat} (s^{-1})	K_m (μM)	k_{cat}/K_m ($M^{-1}s^{-1}$)	K_i (μM)
(R)-Staphylopine	0.45 ± 0.03	6 ± 1	80,000 ± 10,000	22 ± 2
(S)-Staphylopine	0.019 ± 0.002	4 ± 2	5,000 ± 2,000	-
(R)-Pseudopaline	1.4 ± 0.4	10 ± 4	140,000 ± 70,000	0.4 ± 0.1
(S)-Pseudopaline		Indeterminate		

(S)-Pseudopaline binds above the nicotinamide ring of $NADP^+$ (**Figure 4-3A-C**). The imidazole ring of the L-HisNA moiety of (S)-pseudopaline stacks in between Y243 and F340. F340 rotates down 30° from its position in PaODH-$NADP^+$ to stack above the imidazole ring while the position of Y243 below the imidazole is unchanged. The C2'' carboxylate of the L-histidine moiety hydrogen bonds with R319 and Y320 originating from the dimerization domain[13]. In PaODH-(S)-Pse, Y289 rotates 120° to hydrogen bond the C1 carboxylate. This serves as a "cap" that occludes solvent accessibility to the active site. H219 is proposed to be the catalytic base and is hydrogen bonded to the carboxylate of C5 and to the carboxylate of C2' in chain B. In chain A, H219 hydrogen bonds only to the C2' carboxylate and the C5 carboxylate is rotated out of the active site and hydrogen bonds instead to K168. Each of the residues described above are modeled into complete electron density.

(S)-pseudopaline does not appear to be in a catalytically competent conformation, despite stable binding within the active site. The hydride that is transferred to $NADP^+$ during the reverse reaction resides on C2. In the PaODH-(S)-Pse structure C2 is 5.3 Å (chain A) and 7.9 Å (chain B) distant from the nicotinamide hydride. In this reaction, activated water is expected to act as a nucleophile attacking C2 to hydrolyze the Schiff base intermediate, but the (S) configuration at this position results in tight packing between the C1 carboxylate and the imidazole ring providing insufficient space for a water molecule.

PaODH crystals catalyze the hydrolysis of (R)-pseudopaline

To solve structures with (R)-pseudopaline, PaODH crystals were grown in the presence of 2 mM $NADP^+$ and soaked in cryoprotectant containing 10 mM (R)-pseudopaline for 15, 45, 60 minutes or 20 mM (R)-pseudopaline for 120 minutes. Each structure was solved and two representative structures are presented here. PaODH-(R)-Pse-1hr was soaked for 1 hour and solved at 1.65 Å and PaODH-(R)-Pse-2hr was soaked for 2 hours and solved at 2.18 Å. For the

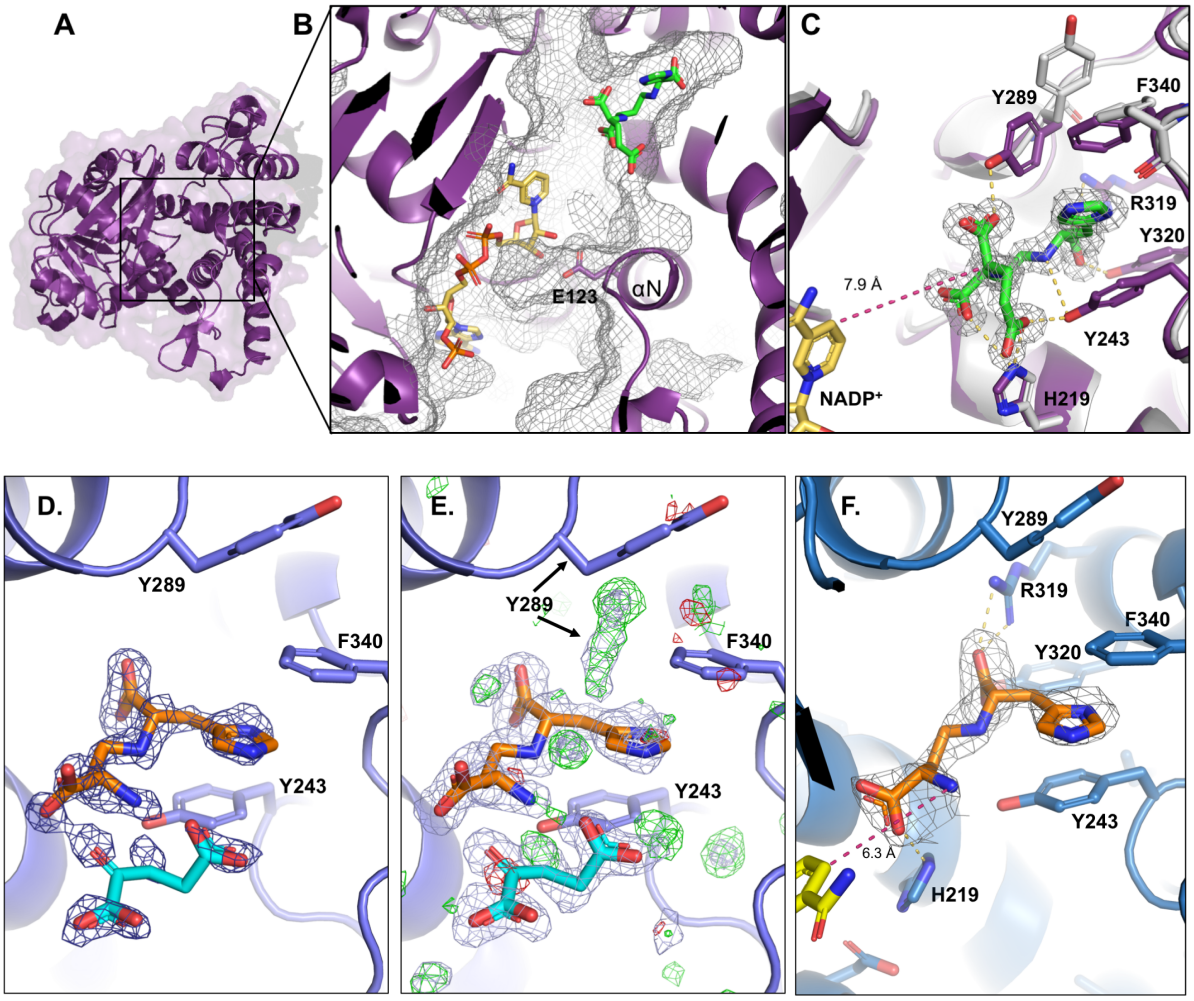

Figure 4-3. PaODH structures with (S)-pseudopaline, L-HisNA and α-ketoglutarate bound. PaODH-(S)-Pse at 1.64 Å in panels A-C; chain B shown. Ligand density for PaODH-(R)-Pse-1hr at 1.65 Å in panels D and E. Ligand density for PaODH-(R)-Pse-2hr at 2.18 Å in panel F. (S)-pseudopaline (green), $NADP^+$ (yellow), L-HisNA (orange) and α-ketoglutarate (cyan). **A)** PaODH-(S)-Pse ribbon diagram. **B)** Active site cavity with a CASTp (computed atlas of surface topography of proteins) calculated surface (gray mesh). **C)** Overlay of PaODH-$NADP^+$ (gray) and PaODH-(S)-Pse (purple). Pink dashed line is the distance between C4 of the nicotinamide ring and C2 of (S)-pseudopaline. Yellow dashed lines indicate hydrogen bonding interactions. Electron density around (S)-pseudopaline is displayed as an mF_o-DF_c omit map contoured at 3.5 σ. **D)** PaODH-(R)-Pse-1hr. Ligands overlaid with a 2mF_o-DF_c electron density map contoured at 1.5 σ as seen

following the final round of refinement (dark blue mesh). **E)** PaODH-(R)-Pse-1hr with an active site overlay with a mF_o-DF_c difference electron density map contoured at 3.0 σ (negative density is red, positive density is green). A Polder electron density map generated with L-HisNA and a-ketoglutarate omitted from the model and contoured at 4.5 σ is shown in light blue. **F)** PaODH-(R)-Pse-2hr. L-HisNA overlaid with a mF_o-DF_c omit map generated with L-HisNA omitted and contoured at 3.5 σ. There is no density for α-ketoglutarate in this structure.

PaODH-(R)-Pse-1hr structure, complete density is present for the L-HisNA and is positioned identically to the L-HisNA portion of (S)-pseudopaline as described above. Density for α-ketoglutarate is weak, suggesting low occupancy, as seen in the 2mF_o-DF_c electron density map (**Figure 4-3D**). We modeled both (R)-pseudopaline into this density and modeled L-HisNA and α-ketoglutarate separately with the latter model better accounting for the observed density. A Polder map (which eliminates solvent flattening allowing visualization of weaker electron density) generated with L-HisNA and α-ketoglutarate omitted demonstrates this, though C2 and C3 remain poorly fit to the electron density (**Figure 4-3E**). In PaODH-(S)-Pse, Y289 is in complete density and is rotated 120° into a "closed" position where it hydrogen bonds with the C2 carboxylate of (S)-pseudopaline. In PaODH-$NADP^+$, Y289 is in complete density but is rotated up in an "open" position away from the active site. In the PaODH-(R)-Pse-1hr density is evident for both rotameric positions for Y289. We have modeled Y289 in the "open" position, but display positive electron density (green) from a mF_o-DF_c map in the "closed" position (**Figure 4-3E**). This suggests that rotation of Y289 plays a role in stabilizing substrates during the catalytic cycle and that the "open" position is likely assumed only during binding or release.

Given the stability of the complex observed in PaODH-(S)-Pse, our interpretation of PaODH-(R)-Pse-1hr is that (R)-pseudopaline has been hydrolyzed into L-HisNA and α-ketoglutarate. PaODH-(R)-Pse-2hr provides additional clarity. In this structure, no density is present beyond L-HisNA, providing definitive evidence that the PaODH crystal is catalytically active resulting in a slow hydrolysis of (R)-pseudopaline over 2 hours (**Figure 4-3F**). The α-ketoglutarate, which is not well coordinated in the active site and is exposed to solution, is then able to diffuse away leaving only the L-HisNA product. This slow catalysis and/or release of α-ketoglutarate likely contributes to the weak electron density for α-ketoglutarate in the PaODH-(R)-Pse-1hr structure.

Transient state kinetic analysis of SaODH

We analyzed the kinetic mechanism of SaODH using a transient-state kinetic approach. The oxidation of NADPH to $NADP^+$ was measured at 340 nm. At 7.8 μM or below for both D-HisNA and pyruvate (**Figure 4-4A and B**), oxidation was observed as a single phase. By 31 μM, two phases of NADPH oxidation were clearly apparent; a fast phase with a small amplitude change and a slow phase with a large amplitude change. Experiments with varied D-HisNA were fit globally by numerical integration to model 1 as described in the methods section. Analytical fitting of the data for varied pyruvate from the slow phase to a two exponential decay function, and replotting the rates, illustrates the rate enhancement at low concentrations of pyruvate. This is indicative of a transition from a single turnover to an increasing number of measured turnovers (steady-state turnover at saturating substrate concentrations) as substrate is increased above SaODH concentration (**Figure 4-4, inset**).

NADPH oxidation was also observed using diode array detection to scan changes in absorbance during the reaction at wavelengths from 300-500 nm. The 340 nm slice of data from the diode array recapitulated the data measured only at 340 nm. Thus the fast and slow phases indicate only NADPH oxidation establishing that the absorption of the dihydronicotinamide was not altered by, for example, binding (**Figure 4-5**). NADPH fluoresces with an emission maximum around 450 nm when excited at 340 nm. This signal is both sensitive and known to typically increase when NADPH is sheltered from solution-based collisional quenching upon binding to an enzyme. We performed transient state fluorescence experiments measuring total emission above 360 nm to examine changes to fluorescence with binding and oxidation of NADPH. An increase in fluorescence was observed when SaODH and NADPH were mixed in the stopped-flow cell at final concentrations of 15 μM SaODH and varied concentrations of NADPH from 2.5 to 80 μM. These data were fit by numerical integration to a one-step equilibrium model, as described in the methods section, giving a forward rate constant, k_{+1} = 0.4 x 10^6 $M^{-1}s^{-1}$ ± 0.1 x 10^6 $M^{-1}s^{-1}$, a reverse rate constant k_{-1} = 27 ± 5 s^{-1} for a K_{NADPH} of 70 ± 20 μM (**Figure 4-6A**). The Fitspace contour indicates good confinement of both rate constants (**Figure 4-7**).

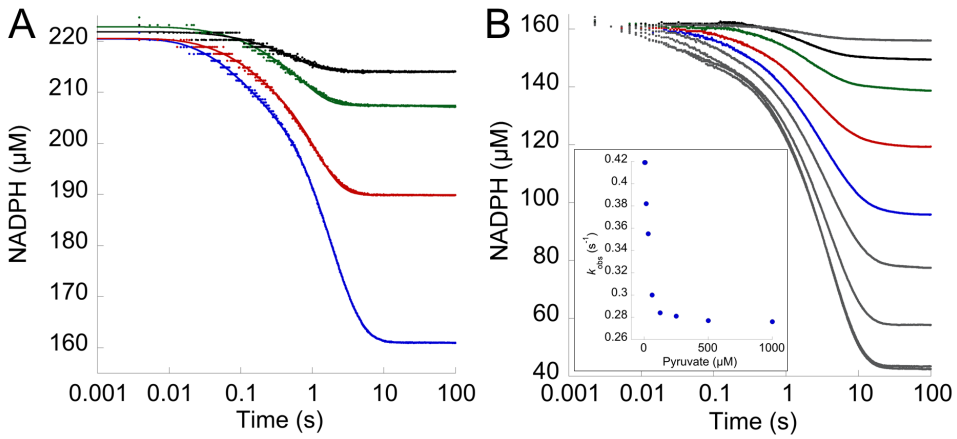

Figure 4-4. Transient state kinetics of SaODH. The oxidation of NADPH to $NADP^+$ was measured at 340 nm by stopped-flow spectrometry. Concentrations were 15 μM SaODH, 1000 μM pyruvate (A) or varied pyruvate (B), varied D-HisNA (A) or 500 μM D-HisNA (B), and 220 μM (A) or 160 μM (B) NADPH. Colors indicate equivalent concentrations of substrate; black – 7.8 μM, green - 15.6 μM, red - 31.3 μM and blue - 62.5 μM. Inset is a secondary plot of k_{obs} (s^{-1}) for the slow reaction phase . **A)** Varied D-HisNA; 7.8, 15.6, 31.3 and 62.5 μM. The global fit to model 1 overlays the data. **B)** Varied pyruvate; 3.9, 7.8, 15.6, 31.2, 62.4, 124.8, 250, 500 and 1000 μM

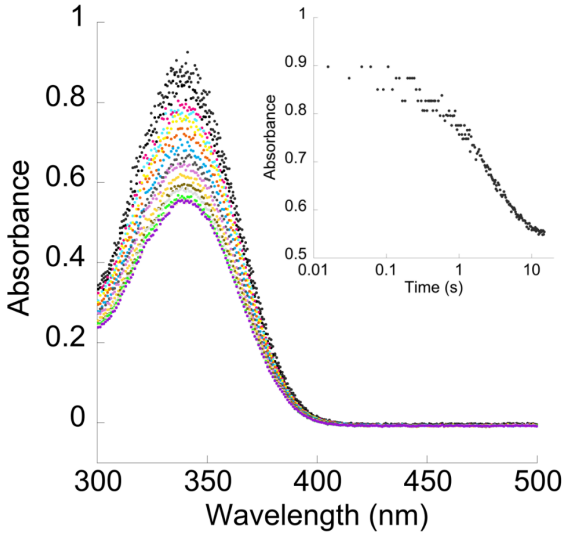

Figure 4-5. Diode array scans. Absorbance scans following mixing of SaODH and substrates. The absorbance peak at 340 nm trends down with no blue or red shift. Replot of absorbance data at 340 nm shows two reaction phases (inset). Final concentrations in the stopped-flow cell: 15 μM SaODH, 50 μM D-HisNA, 150 μM NADPH and 1000 μM pyruvate.

Evidence to explain the catalytic processes underlying the data in Figure 4 was obtained by comparing the absorption data with fluorescence signals obtained under the same conditions. The initial increase in fluorescence upon binding of NADPH in the presence of D-HisNA and pyruvate matched the increase in fluorescence upon binding of NADPH in the absence of D-HisNA and pyruvate (**Figure 4-6B – red trace**). At approximately 0.01 s the increase in fluorescence slows indicating that hydride transfer has commenced. Rather than a decay to equilibrium a second increase and decrease in fluorescence is observed with an amplitude equivalent to the binding of NADPH in the absence of substrates (**Figure 4-6B – gray trace**). This indicates saturation of SaODH by NADPH at equilibrium under the condition of saturating substrate concentration. At progressively lower concentrations of NADPH we observe an incremental loss of the amplitude of this second rise and fall in fluorescence (**Figure 4-6C**). For NADPH concentrations below that of the enzyme (15 μM), the reaction is observed as a single decrease following NADPH binding, suggestive of a net single turnover event (**Figure 4-6C – inset**). Although the fluorescence data suggests that the reaction slows or even stops with increasing concentration by about 0.3 s, the absorption data demonstrate the greatest amplitude change beginning at this time point (**Figure 4-6A and B**).

NADPH fluorescence provides two signals: an emission increase with binding and decrease with oxidation. These signals provide a clear explanation for the absorption data in **Figure 4-6**. This is made is evident by overlaying absorbance and fluorescence data from each experiment taken with the same concentrations (**Figure 4-6D**). During NADPH binding, from 0.001 to 0.02 s, little change in absorbance is observed. The initial drop in fluorescence beginning at 0.02 s correlates in time with the initial fast phase observed by absorption. This fast phase therefore correlates with the completion of one hydride transfer in single turnover consistent with the maximum amplitude of this phase (~15 μM) (**Figure 4-6C – inset)**. When the substrates are in excess of the enzyme concentration, fluorescence again increases (the signal for NADPH binding). This suggests that $NADP^+$ has been released, clearing the active site for the binding of

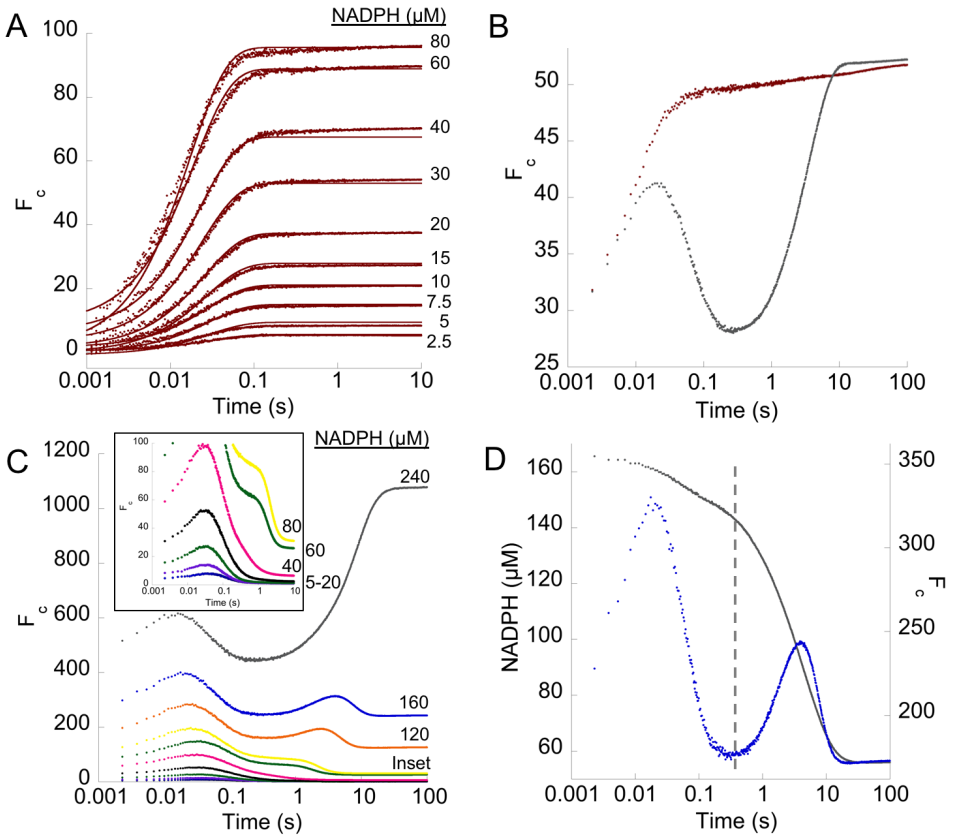

Figure 4-6. Transient state kinetics for SaODH by fluorescence. Fluorescence emission measured beyond 360 nm cut-off filter. **A)** SaODH binding NADPH. Final concentrations in the stopped-flow cell were 15 μM SaODH mixed with varied NADPH concentrations in μM as shown. Data were fit to a one-step equilibrium binding model with a forward rate constant of 0.4 x 10^6 $M^{-1}s^{-1}$ and reverse rate constant of 27 s^{-1}; giving a K_{NADPH} of 70 μM. **B)** Overlay of fluorescence binding and forward reaction data for equivalent enzyme and NADPH concentrations**.** 15 μM SaODH binding 240 μM NADPH (red trace) and 15 μM SaODH reacting with 500 μM D-HisNA, 1000 μM pyruvate and 240 μM NADPH (gray trace). The gray trace is the same as in panel C. **C)** SaODH reaction with varied NADPH**.** 15 μM SaODH reacted with 500 μM D-HisNA, 1000 μM pyruvate and varied NADPH concentrations as shown. Inset shows low concentrations proceeding as a single turnover up to 10 μM NADPH followed by a successive slowing of the progression toward equilibrium at higher NADPH concentrations. **D)** Comparison of forward reaction data by absorption and fluorescence using the same concentration of enzyme and

reactants. 15 μM SaODH reacted with 1 mM pyruvate, 500 μM D-HisNA and 160 μM NADPH. Gray trace is the absorption data from figure 4B. Blue trace is fluorescence data from figure 5C. Dashed line indicates the transition from the fast single-turnover phase to the slow steady-state phase.

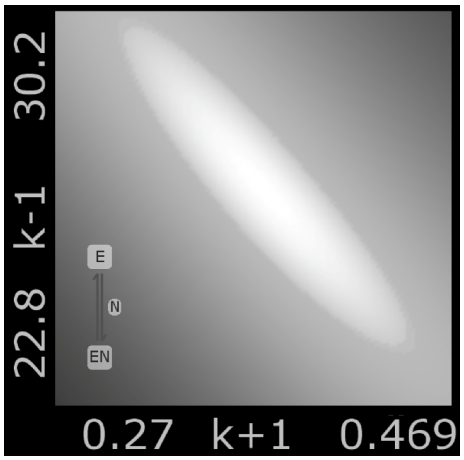

Figure 4-7. Fitspace confidence contour for NADPH binding data.

another NADPH. From this point the catalytic reaction slows substantially suggesting that turnover is contingent on the release of the nascent staphylopine that prevents access of D-HisNA and pyruvate for the next round of catalysis.

We also measured the transient state reaction in the reverse direction, that is the reduction of $NADP^+$ to NADPH followed by the hydrolysis of (R)-staphylopine into D-HisNA and pyruvate (**Figure 4-8**). Data from both experiments were fit simultaneously to model 1 (**Figure 4-8**). The reverse reaction shows no evidence of delayed release of D-HisNA or pyruvate but proceeds as a single phase. These data were also fit to model 2 which reverses the binding steps (**Figure 4-9**). Both simulations fit the data comparably suggesting that binding of NADPH and D-HisNA is independent and random.

Inhibition of SaODH by cobalt(II), nickel(II), zinc(II) and copper(II)

Recently, it was proposed that SaODH is inhibited by the transition metals Co(II), Ni(II), Zn(II) and Cu(II), and that this inhibition plays a role in the regulation of staphylopine biosynthesis[17]. The experimental data underpinning this hypothesis were derived from steady-state measurements wherein the authors observed a nearly complete loss of SaODH activity as the concentration of each metal exceeded the concentration of substrate. The cause of this inhibition was proposed to be metal binding an SaODH allosteric site. Additionally, in the presence of low concentrations of Zn(II) and Cu(II), a catalytic enhancement was reported. This enhanced rate was proposed to be due to preferential binding and/or catalysis of D-HisNA coordinated by Zn(II) or Cu(II). Our transient state assays provide a sensitive means of exploring these claims. An alternative explanation of the data presented by Hajjar *et. al.* is that all four inhibitory metal ions bind D-HisNA and that while in complex with metal, D-HisNA is not available as a substrate for SaODH.

To test this hypothesis we performed transient-state assays following the absorbance change upon NADPH oxidation for 300 s. Cobalt(II) chloride, nickel(II) chloride, zinc(II) chloride

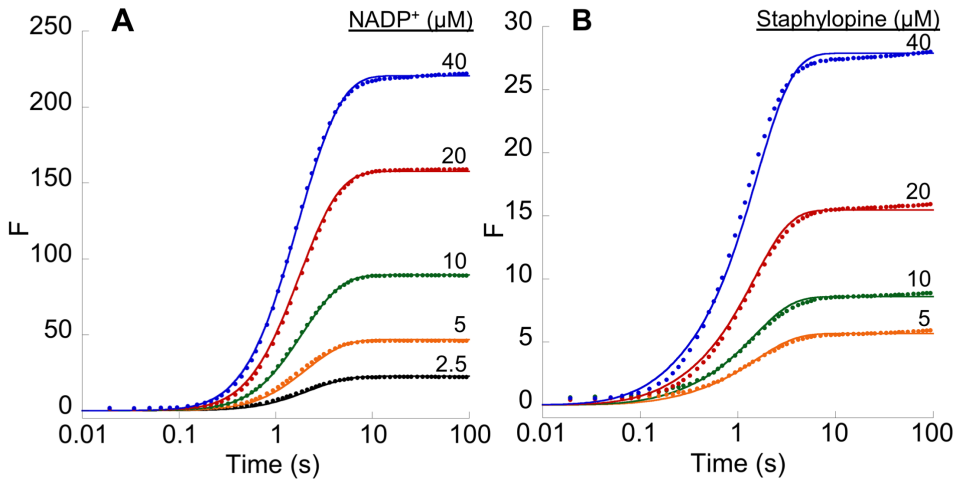

Figure 4-8. Transient state kinetics for the SaODH reverse reaction. Reverse reaction measured as an increase in fluorescence emission at 450 nm as $NADP^+$ is reduced to NADPH. **A)** Varied $NADP^+$. **B)** Varied (S)-staphylopine. Final concentrations in the stopped-flow cell were 15 μM SaODH mixed with 125 μM (R)-staphylopine (A) or varied (S)-staphylopine (B) and varied $NADP^+$ (A) or 150 μM $NADP^+$ (B). Every 10^{th} data point shown for clarity. Both data sets fit simultaneously to model 1 by numerical integration in Kintek Studio 8.0 (lines).

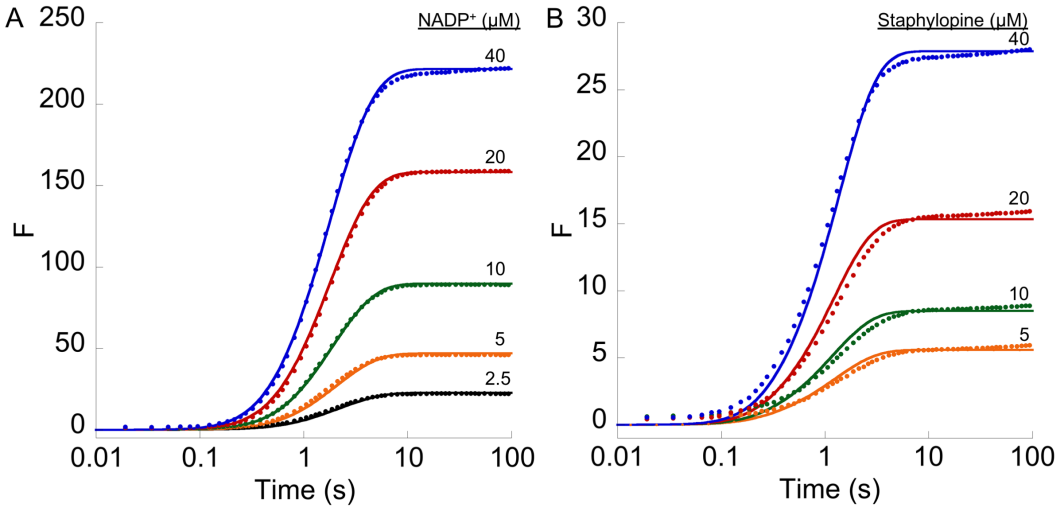

Figure 4-9. Transient state kinetics for the SaODH reverse reaction. Identical to figure 7 except fit is derived from a simulation of model 2. Reverse reaction measured as an increase in fluorescence emission at 450 nm as $NADP^+$ is reduced to NADPH. **A)** Varied $NADP^+$. **B)** Varied (S)-staphylopine. Final concentrations in the stopped-flow cell were 15 μM SaODH mixed with 125 μM (R)-staphylopine (A) or varied (S)-staphylopine (B) and varied $NADP^+$ (A) or 150 μM $NADP^+$ (B). Every 10^{th} data point shown for clarity. Both data sets fit simultaneously to model 2 by numerical integration in Kintek Studio 8.0 (lines).

or copper(II) chloride were pre-incubated with D-HisNA or with SaODH prior to initiating the reaction to compare the effect of metal association with substrate versus enzyme. Data for Co(II) were fit analytically to Eq. 3 or Eq. 4 and by numerical integration to model 1 with the addition of a one-step equilibrium binding term to account for the competition of Co(II) for D-HisNA (**Figure 4-10A, 4-11A-B, 4-12A**). Analytical fits were not intended to define intrinsic rate constants for reaction steps, but rather to descriptively compare phases of the SaODH reaction between data sets. The fast phase is unchanged in the presence of D-HisNa (100 μM) in excess over Co(II) (25μM) (**Figure 4-10A,** 1 – red, blue and green traces). When equimolar Co(II) is pre-incubated with D-HisNA, slow turnover is evident suggesting that D-HisNA is less available for binding by SaODH (**Figure 4-10A,** 1 – black trace). The slow phase traces are initially equivalent when excess unbound D-HisNA is available (**Figure 4-10A**, 2 – red, blue and green traces). In equimolar Co(II), turnover begins very slowly, as a function of the rate of dissociation of the D-HisNA-Co(II) complex (**Figure 4-10A**, 3 – gray trace). The staphylopine formed is also able to compete for Co(II) which frees additional D-HisNA. This results in a slow conversion of D-HisNA to staphylopine with an apparent rate constant of 0.02 s^{-1} (gray trace; Eq. 3 – k_1), greater than 10 times slower than the rate constant used to describe the uninhibited steady state phase of 0.23 s^{-1} (red trace; Eq. 4, k_2). By the late steady-state phase, 45 μM D-HisNA has been consumed (**Figure 4-10A**, 3 – red, blue and green traces). The free substrate concentration is lower in the presence of Co(II) and the steady-state rate declines toward the apparent off rate for the D-HisNA-cobalt complex. In all cases the reaction proceeds to the same equilibrium because the staphylopine product binds Co(II). Importantly, the inhibition due to the presence of Co(II) is equivalent whether Co(II) is pre-incubated with SaODH (**blue trace;** k_1 = 0.37 s^{-1}, k_2 = 0.03 s^{-1}) or pre-incubated with D-HisNA (**green trace;** k_1 = 0.35 s^{-1}, k_2 = 0.03 s^{-1}). Global fitting demonstrates that the data can be simulated using model 1 with only the addition of a one-step equilibrium term that accounts for Co(II) binding of D-HisNA. These data suggest that the inhibition is not due to

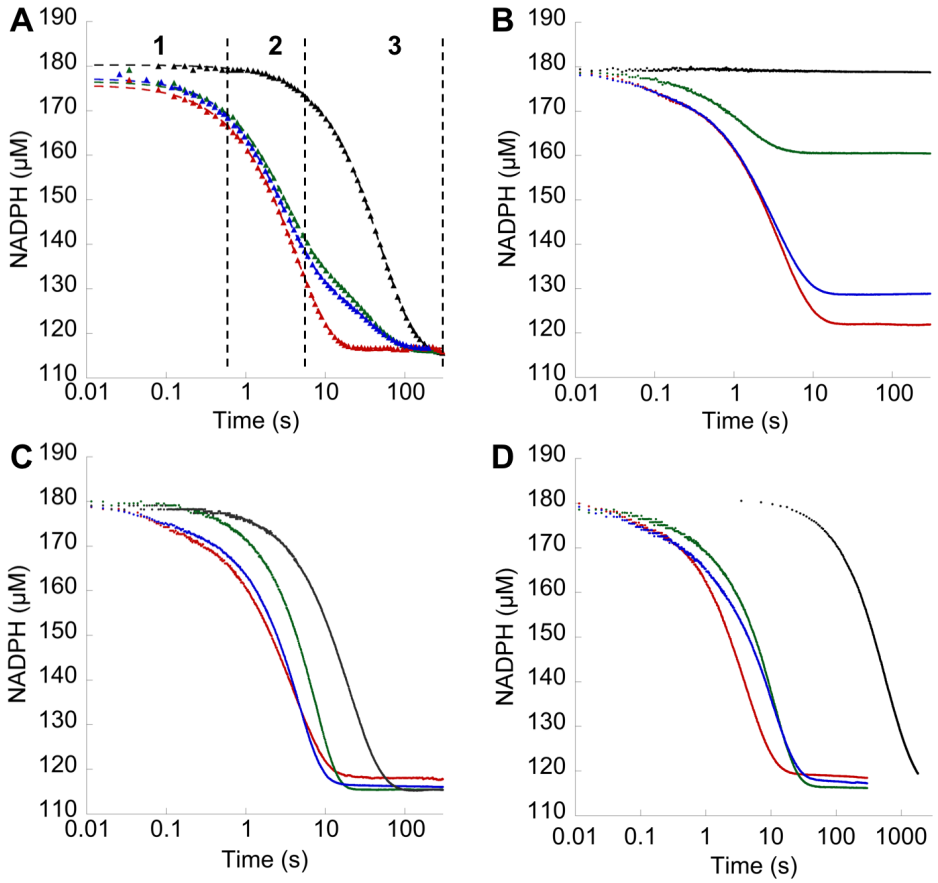

Figure 4-10. Inhibition of SaODH reaction by metal ions. Transient state kinetics for SaODH measuring NADPH oxidation. Final concentrations in the stopped-flow cell were 15 μM SaODH, 180 μM NADPH and 1 mM pyruvate mixed with a final concentration of 100 μM D-HisNA. The black traces are 100 μM metal pre-incubated with 100 μM D-HisNA. The green traces are 25 μM (Co(II) or Ni(II)) or 50 μM (Zn(II) or Cu(II)) pre-incubated with D-HisNA. The blue traces are 25 μM (Co(II) or Ni(II)) or 50 μM (Zn(II) or Cu(II)) pre-incubated with SaODH. The red trace is 0 μM metal added. **A)** Co(II); 1 - Fast phase. 2 - Early steady-state phase. 3 - Late steady-state or inhibited phase. The black trace is fit to Eq. 3 and the red, blue and green traces are fit to Eq. 4. Every 10th data point shown as triangles for clarity. **B)** Ni(II). **C)** Zn(II). **D)** Cu(II).

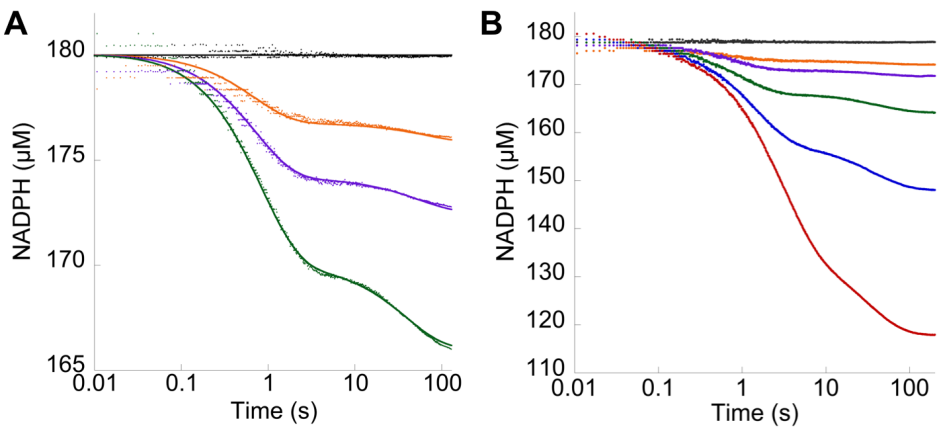

Figure 4-11. Transient kinetics of SaODH pre-incubated with cobalt(II)**.** Transient state kinetics for SaODH measuring NADPH oxidation in the presence and absence of cobalt(II) chloride pre-incubated with SaODH. Final concentrations in the stopped-flow cell were 15 μM SaODH, 180 μM NADPH, 1 mM pyruvate and 25 μM Co(II) and mixed with varied D-HisNA. D-HisNA concentrations: black – 0μM, orange – 6.3 μM, purple – 12.5 μM, green – 25 μM, blue – 50 μM, red – 100 μM. **A)** Varied D-HisNA, from 0-25 μM, overlaid with optimized simulations generated in Kintek Explorer 8.0 using model 1 with the addition of a one-step equilibrium term to account for cobalt competition for D-HisNA. **B)** Full data set with D-HisNA concentrations from 0-100 μM.

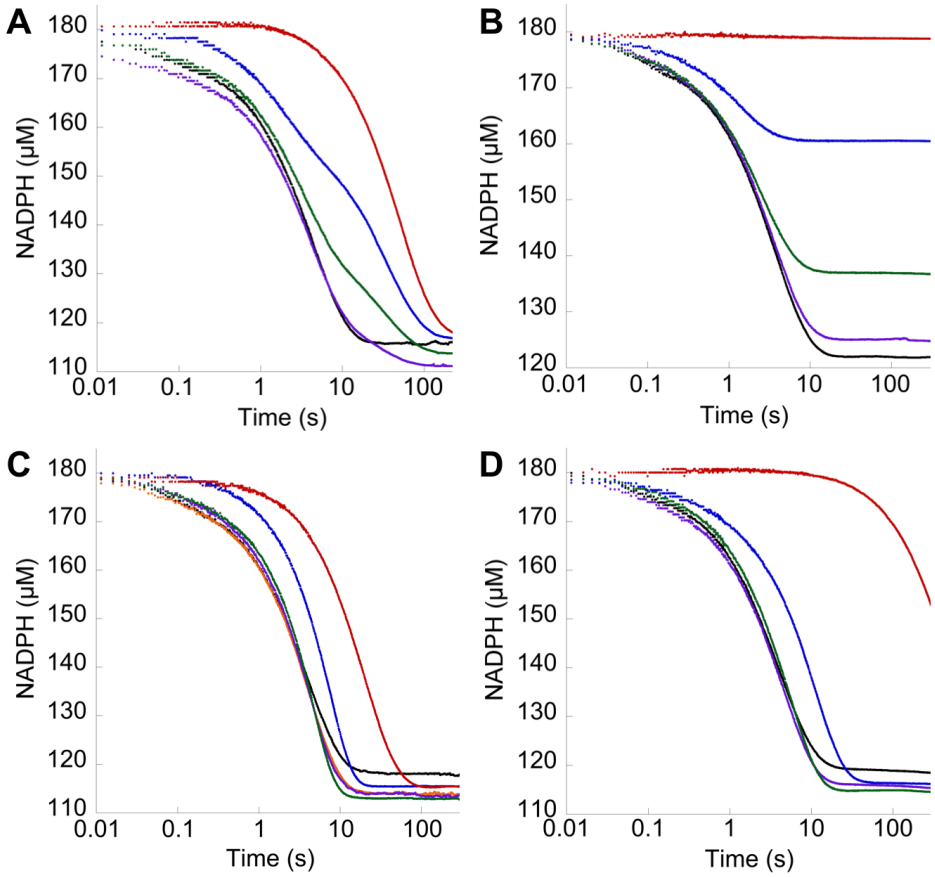

Figure 4-12. SaODH transient kinetics with varied metal ion concentrations pre-incubated with D-HisNA. Transient state kinetics for SaODH measuring NADPH oxidation in the presence and absence of metal pre-incubated with D-HisNA. Final concentrations in the stopped-flow cell were 15 μM SaODH, 180 μM NADPH and 1 mM pyruvate mixed with 100 μM D-HisNA and varied Co(II), Ni(II), Zn(II) or Cu(II) chloride. Metal concentrations: black – 0μM, orange – 6.3 μM, purple – 12.5 μM, green – 25 μM, blue – 50 μM, red – 100 μM. **A)** Varied cobalt(II). **B)** Varied nickel(II). **C)** Varied zinc(II). **D)** Varied copper(II).

an association of Co(II) with the enzyme, but instead due to the D-HisNA-Co(II) complex making D-HisNA unavailable as a substrate.

The effect of Ni(II), Zn(II) and Cu(II) were also evaluated and the data provide similar conclusions (**Figure 4-10B-D, 4-12B-D**). In no case was the reaction rate observed to be faster, regardless of preincubation of the metal ion with enzyme or with substrate. In every case, the presence of metal resulted in either equivalent rates or in inhibition. Ni(II) binds D-HisNA with sufficient affinity that equimolar Ni(II):D-HisNA resulted in no turnover on a 5 min time scale (**Figure 4-10B, 4-12B**). Reducing Ni(II)concentrations left free D-HisNA that was converted into staphylopine. The reactions did not proceed to the equilibrium observed in the absence of metal suggesting that staphylopine was unable to free D-HisNA from Ni(II). When Ni(II) was preincubated with SaODH more staphylopine was made than when Ni(II) was preincubated with D-HisNA. This suggests a slow rate of association between Ni(II) and D-HisNA that allows significant catalysis to occur prior to formation of the Ni(II):D-HisNA coordination complex.

When Zn(II) was preincubated with SaODH the initial rate was faster than for preincubation with D-HisNA, but both rates were slower than in the absence of Zn(II) (**Figure 4-10C, 4-12C**). This again suggests a slow rate of association between Zn(II) and D-HisNA allowing significant catalysis prior to complex formation. When equimolar Zn(II) was preincubated with D-HisNA the reaction was slowed approximately 10-fold. The results with Cu(II) are similar to those of Zn(II). No rate enhancement was observed. Equimolar Cu(II) preincubated with D-HisNA nearly halted the reaction with only one turnover every 7.5 minutes (**Figure 4-10D, 4-12D**). In no case is there evidence of metal-dependent allosterism or of a rate enhancement due to preferential catalysis of a metal:D-HisNA complex.

Discussion

Staphylopine was first synthesized by Toronto Chemical Company for Arnoux *et. al.*[1] and the total synthesis was later published by Lei *et. al.*[19] In both cases the (S)-staphylopine diastereomer was made, but evidence for the production of the (S) stereocenter by the opine

dehydrogenase has been absent from the literature. The stereochemistry of the opine metallophore products may affect receptor recognition, efficiency of transport and metal coordination making full stereochemical determination an important goal. Structural evidence has also been lacking for substrate and opine metallophore product ligands. As a result, the amino acid residues involved in binding and catalysis have only been hypothesized previously[13]. Steady-state kinetic methods have been employed to study substrate specificity and k_{cat} in the opine dehydrogenases, but transient-state methods have not been used to examine underlying catalytic mechanisms. Finally, a recent report suggested allosteric enhancement and inhibition for Zn(II) and Cu(II) under different conditions and allosteric inhibition by Co(II) and Ni(II). The data presented herein address each of the above areas of opine dehydrogenase research.

PaODH and SaODH, as well as octopine dehydrogenase (PDB:1BG6), have been previously observed to crystallize with open active sites[13, 34]. The holoenzyme structures of PaODH-(S)-Pse and PaODH-(R)-Pse are only slightly different. In monomer A and B of PaODH-(S)-Pse the distance between C4 of the nicotinamide ring and C2 of (S)-pseudopaline is too distant for hydride transfer at 5.3 Å and 7.9 Å respectively. The PaODH-(R)-Pse structures are similar, but the more open monomer B has weaker electron density for L-HisNA and we chose to leave this density unmodeled. These higher resolution structures do provide additional insight into the question of active site dynamics during the catalytic cycle. The stacking arrangement of F340 and the rotation of Y289 into a closed position eliminates solvent accessibility within the L-HisNA binding pocket (**Figure 4-13**). E123 hydrogen bonds with the hydroxyls of the nicotinamide ribose sugar and is found on α-helix N, as described previously[13] (**Figure 4-3B**). αN is a core helix of the catalytic domain and E123 acts from the catalytic domain to stabilize $NADP^+$ in the Rossmann-like fold domain. The position of E123, so near to $NADP^+$ suggests that αN does not move to position the substrate for hydride transfer. Rather, it may be the long loop from αM to β13 that transiently closes the active site. This loop contains F340 which is repositioned upon L-HisNA

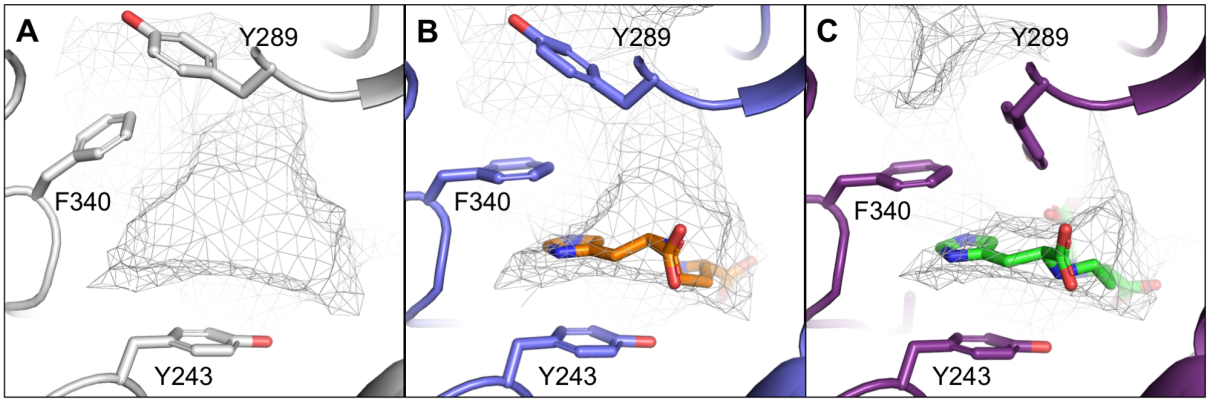

Figure 4-13. Solvent exclusion upon substrate binding by PaODH. Ligand binding site rotated 180° with respect to Figure 5B. Solvent accessible surfaces calculated by CASTp. **A)** PaODH-$NADP^+$. **B)** PaODH-R-Pse-1hr with L-HisNA bound and Y289 in the open position. **C)** PaODH-S-Pse-1hr with (S)-pseudopaline bound and Y289 in the closed position.

binding. Thus, the dihydronicotinamide ring may approach the Schiff base only transiently to affect hydride transfer.

The open character of the active site suggests that NADPH and HisNA can bind PaODH and SaODH without any dependency on order. Our kinetic data support this observation. Indeed, it is possible to reverse the first two steps of model 1 (D-HisNA and NADPH binding steps) and achieve similar fits for both the forward and reverse transient state reactions for SaODH. Once NADPH and HisNA are associated with the enzyme, the α-keto acid enters and condensation occurs forming the Schiff base intermediate. This is followed rapidly by a transient "closure" event resulting in hydride transfer. Product release is rate-limiting with $NADP^+$ released first followed by slow release of the metallophore product (**Figure 4-14**).

We have defined the residues that stabilize the L-HisNA moiety of (R)-pseudopaline. In all the structures solved for this manuscript, the electron density for the C1'' carboxylate and the imidazole ring of L-HisNA are the most well-defined features in the substrate or product electron density maps. This suggests the importance of these contact points in the recognition and binding of L-HisNA and raises the question of whether D-HisNA is bound by staphylopine dehydrogenase using the same residues. In PaODH, R319 and Y320 hydrogen bond to the C1'' carboxylate and F340 and Y243 stack above and below the imidazole group. SaODH has an rmsd of 2.2 Å over 427/432 Cα residues in a structural comparison with PaODH. The resulting overlay demonstrates that SaODH conserves all four of these residues in the same position, but to accommodate the D-HisNA diastereomer using the same contact points would require the secondary amine to be positioned at an angle 120° from the L-HisNA secondary amine. This is certainly possible within the large active site cavity. Interestingly, we have noted previously[13] that SaODH is also able to accept L-HisNA as a substrate with a k_{cat}/K_m only 3-fold lower than for D-HisNA. PaODH is specific for L-HisNA.

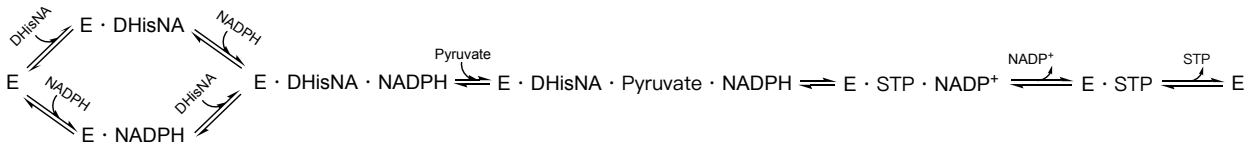

Figure 4-14. SaODH kinetic model.

Recently, Arnoux and colleagues published two structures of SaODH that were modelled with (S)-staphylopine (PDB:6H3F) and D-HisNA (PDB:6H3D) bound, respectively[17]. The difficulty with this interpretation is that the electron density modeled with (S)-staphylopine is limited to three disconnected areas (**Figure 4-15A**). Most strikingly, the C1 carboxylate of pyruvate is modeled in a position within hydrogen bonding distance of $NADP^+$. It seems more probable that this density is a water molecule or an ion. In the second structure density in the shape of D-histidine is present, but the aminobutyrate moiety for D-HisNA is not present (**Figure 4-15A**), as noted by the authors. Additionally, the D-histidine moiety is positioned very differently between the two structures with its carboxylate group in opposite orientations. An alignment of PaODH-(R)-Pse-1hr and SaODH with staphylopine bound (PDB: 6H3F), as described above, suggests that the position of D-histidine as co-crystallized with SaODH is likely correct as it hydrogen bonds with R319 in a manner similar to PaODH. The electron density presented as representing (S)-staphylopine most likely represents solvent molecules rather than the metallophore product (**Figure 4-15A and B**).

In the same paper, data are presented to demonstrate allosteric inhibition of SaODH in the presence of Co(II), Ni(II), Zn(II) and Cu(II). Our data indicate inhibition by each of these metals, but not due to an association of the metal with the enzyme. Not surprisingly, D-HisNA binds Co(II), Ni(II), Zn(II) and Cu(II) effectively, as the SaODH reaction adds only one additional ligand group, a carboxylate from pyruvate, during the biosynthesis of staphylopine. When bound by metal, the D-HisNA substrate moieties that would be recognized by the SaODH active site are instead coordinated by the metal. The metal:HisNA coordination complex results in a very different geometry than the elongated L-HisNA pose seen in our structures of PaODH. It is, therefore, unlikely that the metal:D-HisNA complex is a substrate for SaODH as was hypothesized by Hajjar *et. al.* Rather, the metal:D-HisNA coordination complex reduces the freely available D-HisNA pool and depresses the observed activity of SaODH as a function of diminished substrate concentration. The authors also report on a structural basis for metal binding to SaODH based on three X-ray crystal structures. These crystals were soaked in either 5 mM Mn(II), Zn(II) or Ni(II).

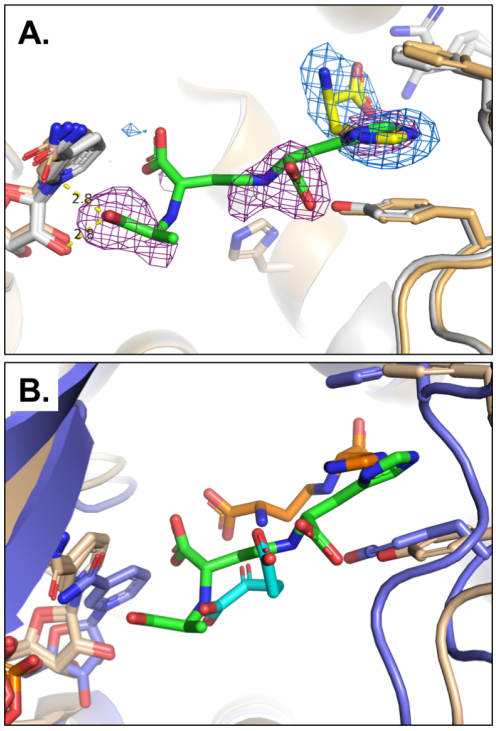

Figure 4-15. Overlay of SaODH and PaODH ligand structures. A) Overlay of SaODH structures. Yellow is SaODH with (S)-staphylopine bound (green carbons) from PDB:6H3F. Gray is SaODH with D-histidine bound (yellow carbons) from PDB: 6H3D. Purple mesh is (S)-staphylopine mF_o-DF_c omit map generated in phenix.polder and contoured at 3.5 σ using 6H3F structure factors. Blue mesh is D-histidine mF_o-DF_c omit map generated in phenix.polder and contoured at 3.5 σ using 6H3D structure factors. The C1 carboxylate of the pyruvate moiety of (S)-Staphylopine is within hydrogen bonding distance of $NADP^+$. B) Overlay of SaODH and PaODH. Yellow is SaODH with (S)-staphylopine bound (green carbons) as for A. Purple is PaODH-(R)-PSE-1hr with L-HisNA (orange carbons) and α-ketoglutarate bound (cyan carbons).

We note, however, that these data are not archived in the PDB and that no refinement statistics were included in the crystallographic data table, despite being included in the main body of the paper and featured in a figure.

Our data definitively show that SaODH and PaODH catalyze reversible reactions specific for the (R) diastereomer of the respective opine products, staphylopine and pseudopaline. To generate the (R) diastereomer and not the (S), the ODH must position the α-keto acid for nucleophilic attack on the *re* face of the sp^2-hybridized carbon C2. PaODH-(R)-Pse-1hr is valuable as it provides evidence for catalysis within the PaODH protein crystal, but the position of α-ketoglutarate during the catalytic cycle is defined by weak electron density representing low occupancy. PaODH-(R)-Pse-2hr captures the completion of catalysis prior to L-HisNA release for the reverse reaction. Thus, both our kinetic and structural data support the conclusion that PaODH and SaODH produce metallophores with (R) stereochemistry at C2.

Interestingly, it was recently shown that when 100 μM (S)-pseudopaline is added to wild type *P. aeruginosa* PAO1 grown on Vogel-Bonner minimal media with 50 μM of added EDTA the intracellular concentrations of Zn(II), Fe(II), Co(II) and Ni(II) are increased[10]. 100 μM (R)-pseudopaline did not increase metal uptake in comparison to wild type *P. aeruginosa* PAO1 grown in the absence of any added metallophore. The authors also demonstrated the uptake of a pseudopaline derivative into *P. aeruginosa* PAO1 cells via the conjugation of a fluorescence probe detected by fluorescence microscopy. These intriguing data could suggest that the presence of 100 μM (R)-pseudopaline acts as a signal that down-regulates additional (R)-pseudopaline biosynthesis while (S)-pseudopaline is treated as an exogenous metallophore and does not directly affect regulation. The $\Delta G^{\circ\prime}$ of SaODH is -1.9 $\pm$ 0.5 kJ/mol (calculated from the product formation measured in five different transient state absorbance experiments). Thus, production of staphylopine is highly dependent on the maintenance of low staphylopine concentrations in the cytosol. We assume PaODH operates similarly, so adding exogenous (R)-pseudopaline to the

media could directly slow the native production of pseudopaline. Nevertheless, the observation that (S)-pseudopaline both binds to PaODH (structures herein) and that it is taken up into *P. aeruginosa* PAO1, even with a conjugated fluorophore attached[10], has exciting implications for the possible development of an inhibitor for PaODH or for the delivery of an analog conjugated to an antibiotic.

Conclusions

SaODH and PaODH catalyze reversible reactions generating (forward biosynthetic reaction) or consuming (reverse reaction) the (R) diastereomer of staphylopine (SaODH) or pseudopaline (PaODH). L-HisNA binding is directed primarily by the histidine moiety in PaODH with a similar bindingcontacts likely in SaODH due to high structural homology. The kinetic mechanism has random association of D-HisNA and NADPH followed by the alpha-keto acid substrate. Product release is strictly ordered by slow staphylopine release and this process was found to be rate-limiting for SaODH. Metal inhibition by Co(II), Ni(II), Zn(II) and Cu(II) is due to competition for substrate rather than direct inhibition of the enzyme.

References

[1] Ghssein, G.; Brutesco, C.; Ouerdane, L.; Fojcik, C.; Izaute, A.; Wang, S. L.; Hajjar, C.; Lobinski, R.; Lemaire, D.; Richaud, P.; Voulhoux, R.; Espaillat, A.; Cava, F.; Pignol, D.; Borezee-Durant, E.; Arnoux, P., Biosynthesis of a broad-spectrum nicotianamine-like metallophore in Staphylococcus aureus. *Science* **2016,** *352* (6289), 1105-1109.

[2] McFarlane, J. S.; Lamb, A. L., Biosynthesis of an Opine Metallophore by Pseudomonas aeruginosa. *Biochemistry* **2017,** *56*, 5967-5971.

[3] Lhospice, S.; Gomez, N. O.; Ouerdane, L.; Brutesco, C.; Ghssein, G.; Hajjar, C.; Liratni, A.; Wang, S.; Richaud, P.; Bleves, S.; Ball, G.; Borezée-Durant, E.; Lobinski, R.; Pignol, D.; Arnoux, P.; Voulhoux, R., Pseudomonas aeruginosa zinc uptake in chelating environment is primarily mediated by the metallophore pseudopaline. *Scientific Reports* **2017,** *7* (1), 1-10.

[4] Mastropasqua, M. C.; D'Orazio, M.; Cerasi, M.; Pacello, F.; Gismondi, A.; Canini, A.; Canuti, L.; Consalvo, A.; Ciavardelli, D.; Chirullo, B.; Pasquali, P.; Battistoni, A., Growth of Pseudomonas aeruginosa in zinc poor environments is promoted by a nicotianamine-related metallophore. *Mol Microbiol* **2017,** *106* (4), 543-561.

[5] Remy, L.; Carriere, M.; Derre-Bobillot, A.; Martini, C.; Sanguinetti, M.; Borezee-Durant, E., The Staphylococcus aureus Opp1 ABC transporter imports nickel and cobalt in zinc-depleted conditions and contributes to virulence. *Mol Microbiol* **2013,** *87* (4), 730-43.

[6] Grim, K. P.; San Francisco, B.; Radin, J. N.; Brazel, E. B.; Kelliher, J. L.; Parraga Solorzano, P. K.; Kim, P. C.; McDevitt, C. A.; Kehl-Fie, T. E., The Metallophore Staphylopine Enables Staphylococcus aureus To Compete with the Host for Zinc and Overcome Nutritional Immunity. *MBio* **2017,** *8* (5), 1-16.

[7] Gi, M.; Lee, K. M.; Kim, S. C.; Yoon, J. H.; Yoon, S. S.; Choi, J. Y., A novel siderophore system is essential for the growth of Pseudomonas aeruginosa in airway mucus. *Sci Rep* **2015,** *5*, 1-15.

[8] Luo, S.; Ju, Y.; Zhou, J.; Gu, Q.; Xu, J.; Zhou, H., Crystal structure of CntK, the cofactor-independent histidine racemase in staphylopine-mediated metal acquisition of Staphylococcus aureus. *Int J Biol Macromol* **2019**.

[9] Morizawa, K., The extractive substances in *Octopus octopodia*. *Acta Scholae Medicinalis Universitatis Imperialis in Kioto* **1927,** *9*, 14.

[10] Zhang, J.; Zhao, T.; Yang, R.; Siridechakorn, I.; Wang, S.; Guo, Q.; Bai, Y.; Shen, H. C.; Lei, X., De novo synthesis, structural assignment and biological evaluation of pseudopaline, a metallophore produced by Pseudomonas aeruginosa. *Chemical Science* **2019**.

[11] Kato, Y.; Yamada, H.; Asano, Y., Stereoselective synthesis of opine-type secondary amine carboxylic acids by a new enzyme opine dehydrogenase use of recombinant enzymes. *Journal of Molecular Catalysis* **1996,** *1*, 151-160.

[12] Haibin, C.; Collier, S. J.; Sukumaran, J.; Smith, D.; Moore, J. C.; Hughes, G.; Janey, J.; Huisman, G.; Novick, S.; Agard, N.; Alvizo, O.; Cope, G.; Yeo, W. L.; NG, S. Engineered Imine Reductases and Methods for the Reductive Animation of Ketone and Amine Compounds. 2013.

[13] McFarlane, J. S.; Davis, C. L.; Lamb, A. L., Staphylopine, pseudopaline and yersinopine dehydrogenases: a structural and kinetic analysis of a new functional class of opine dehydrogenase. *J Biol Chem* **2018**.

[14] Doublet, M. O., A, Investigations on the Kinetic Mechanism of OctopineDehydrogenase Part 1. *European Journal of Biochemistry* **1975,** *59*, 9.

[15] Doublet, M. O., A; Baici, A; Luisi, P.L., Investigations on the Kinetic Mechanism of OctopineDehydrogenase Part 2. *European Journal of Biochemistry* **1975,** *59*, 7.

[16] Johnson, K. A., *Transient-State Kinetic Analysis of Enzyme Reaction Pathways*. Elsevier: 1992; p 61.

[17] Hajjar, C.; Fanelli, R.; Laffont, C.; Brutesco, C.; Cullia, G.; Tribout, M.; Nurizzo, D.; Borezee-Durant, E.; Voulhoux, R.; Pignol, D.; Lavergne, J.; Cavelier, F.; Arnoux, P., Control by Metals of Staphylopine Dehydrogenase Activity during Metallophore Biosynthesis. *J Am Chem Soc* **2019**.
[18] Pace, C. N.; Vajdos, F.; Fee, L.; Grimsley, G.; Gray, T., How to measure and predict the molar absorption coefficient of a protein. *Protein Science* **1995,** *4*, 12.
[19] Zhang, J.; Wang, S.; Bai, Y.; Guo, Q.; Zhou, J.; Lei, X., Total Syntheses of Natural Metallophores Staphylopine and Aspergillomarasmine A. *J Org Chem* **2017,** *82*, 13643-13648.
[20] Lakowicz, J. R., *Principles of Fluorescence Spectroscopy*. 3rd ed.; Springer: New York, 2006; p 13.
[21] Johnson, K. A.; Simpson, Z. B.; Blom, T., FitSpace explorer: an algorithm to evaluate multidimensional parameter space in fitting kinetic data. *Anal Biochem* **2009,** *387* (1), 30-41.
[22] Johnson, K. A.; Simpson, Z. B.; Blom, T., Global kinetic explorer: a new computer program for dynamic simulation and fitting of kinetic data. *Anal Biochem* **2009,** *387* (1), 20-9.
[23] McPhillips, T. M.; McPhillips, S. E.; Chiu, H.-J.; Cohen, A. E.; Deacon, A. M.; Ellis, P. J.; Garman, E.; Gonzalez, A.; Sauter, N. K.; Phizackerley, R. P.; Soltis, S. M.; Kuhn, P., Blu-Ice and the Distributed Control System: software for data acquisition and instrument control at macromolecular crystallography beamlines. *Journal of Synchrotron Radiation* **2002,** *9* (6), 401-406.
[24] Kabsch, W., Xds. *Acta Crystallogr D Biol Crystallogr* **2010,** *66* (Pt 2), 125-32.
[25] McCoy, A. J.; Grosse-Kunstleve, R. W.; Adams, P. D.; Winn, M. D.; Storoni, L. C.; Read, R. J., Phaser crystallographic software. *J Appl Crystallogr* **2007,** *40* (Pt 4), 658-674.
[26] Emsley, P.; Lohkamp, B.; Scott, W. G.; Cowtan, K., Features and development of Coot. *Acta Crystallogr D Biol Crystallogr* **2010,** *66* (Pt 4), 486-501.
[27] Adams, P. D.; Afonine, P. V.; Bunkoczi, G.; Chen, V. B.; Davis, I. W.; Echols, N.; Headd, J. J.; Hung, L. W.; Kapral, G. J.; Grosse-Kunstleve, R. W.; McCoy, A. J.; Moriarty, N. W.; Oeffner, R.; Read, R. J.; Richardson, D. C.; Richardson, J. S.; Terwilliger, T. C.; Zwart, P. H., PHENIX: a comprehensive Python-based system for macromolecular structure solution. *Acta Crystallogr D Biol Crystallogr* **2010,** *66* (Pt 2), 213-21.
[28] Chen, V. B.; Arendall, W. B., 3rd; Headd, J. J.; Keedy, D. A.; Immormino, R. M.; Kapral, G. J.; Murray, L. W.; Richardson, J. S.; Richardson, D. C., MolProbity: all-atom structure validation for macromolecular crystallography. *Acta Crystallogr D Biol Crystallogr* **2010,** *66* (Pt 1), 12-21.
[29] Krissinel, E.; Henrick, K., Secondary-structure matching (SSM), a new tool for fast protein structure alignment in three dimensions. *Acta Crystallogr D Biol Crystallogr* **2004,** *60* (Pt 12 Pt 1), 2256-68.
[30] Dundas, J.; Ouyang, Z.; Tseng, J.; Binkowski, A.; Turpaz, Y.; Liang, J., CASTp: computed atlas of surface topography of proteins with structural and topographical mapping of functionally annotated residues. *Nucleic Acids Res* **2006,** *34* (Web Server issue), W116-8.
[31] Biellmann, J.; Branlant, G.; Wallen, L., Stereochemistry of octopine and of its isomers and their enzymatic properties. *Bioorganic Chemistry* **1977,** *6*, 89-93.
[32] Van Thoai, N.; Huc, C.; Ba Pho, D.; Olomucki, A., Octopine déshydrogénase Purification et propriétés catalytiques. *Biochimica et Biophysica Acta (BBA) - Enzymology* **1969,** *191* (1), 46 - 57.
[33] Thompson, J.; Donkersloot, J. A., N-(Carboxyalkyl) Amino Acids: Occurence, Synthesis, and Functions. *Annu Rev Biochem* **1992,** *61*, 40.
[34] K.L. Britton, Y. A. a. D. W. R., Crystal structure and active site location of N-(1-D-carboxylethyl)-L-norvaline dehydrogenase. *Nature Structural Biology* **1998,** *5* (7), 9.

Chapter 5

Summary

This work has contributed many important findings to our understanding of opine metallophore biosynthesis. These include:

- The identification of pseudopaline, the opine metallophore produced by *P. aeruginosa*.
- The first steady-state kinetic analysis of a nicotianamine synthase.
- Demonstration of the specificity of *S. aureus* nicotianamine synthase for D-histidine and of *P. aeruginosa* nicotianamine synthase for L-histidine.
- X-ray crystal structures of opine dehydrogenases from *Y. pestis*, *P. aeruginosa* and *S. aureus* and the first liganded structures for any opine dehydrogenase.
- Demonstration of the reversibility and stereospecificity of the *S. aureus* and *P. aeruginosa* opine dehydrogenases.
- Transient state kinetic analysis of the *S. aureus* opine dehydrogenase revealing the rate limiting step in the catalytic cycle.

Future Directions

It is remarkable how quickly science can progress. In the fall of 2015, I sat in a lab meeting discussing the work of Gi and Choi *et. al.*[1], the paper that inspired my doctoral research, debating the hypothesis that *P. aeruginosa* was biosynthesizing a nicotianamine metallophore. Up to that point, the operon in question was the purview of geneticists and had only appeared, mostly as supplemental data, in studies of gene expression under conditions of metal limitation and/or infection. The products and broader functional roles for these pathways remained opaque. It has been a pleasure to contribute to a collective process of discovery involving scientists from three continents. Pseudopaline and staphylopine have names. Their biosynthetic schemes have been elucidated and considerably more is known about their functional roles in metal acquisition. Still,

this work remains in its infancy. Continued study of the enzymes will lead to a better understanding of the mechanisms employed by nicotianamine synthase and opine dehydrogenases. This will allow an exploration of the potential for inhibiting these enzymes as an antimicrobial target or using them as an industrial technology for the unique chemistries they perform. In this final chapter, I present a few future directions that have the potential to lead toward these goals.

Nicotianamine synthase has proven difficult to study. In *P. aeruginosa*, *S. aureus* and especially, *Y. pestis*, the purified enzyme is prone to aggregation and has not yet crystallized. The substrates have no spectroscopic signal that can be followed in a continuous assay making analysis of the kinetic mechanism more difficult. Indeed, we published the first steady-state kinetic parameters for an NAS. Nevertheless, these enzymes are fascinating and in need of further study. Different NAS enzymes are able to use one S-adenosyl-L-methionine (SAM), or two, or three, linking aminobutyrates in a processive chain. Those that use three SAMs, as in plants, are also able to form an azetidine ring, apparently from the first aminobutyrate. Azetidine rings are four-sided, nitrogen-containing heterocycles that appear in various secondary natural products. Other NAS enzymes use amino acids as initial substrates with examples established for L-glutamate, L-histidine and D-histidine. These enzymes differ in length by as much as 200 amino acids. The structural basis for all of this variability is unknown, with only one solved NAS structure in the PDB. Although NAS kinetic analysis requires end point assays, the separation of SAM and its by-product, methylthioadenosine (MTA), is straightforward using an HPLC. Employing inhibition studies, quenching techniques or kinetic isotope effect analysis could still allow a far more advanced understanding of the catalytic cycle than is currently possible. If a lab were to develop these techniques for a candidate NAS they could be employed to dissect the kinetic mechanisms that distinguish azetidine ring formation and processivity.

Only five opine dehydrogenases have been structurally characterized (we solved three of them!), but more liganded structures are needed. We have been able to produce high resolution PaODH structures with ligands bound, defining the position of the L-HisNA portion of

pseudopaline, but we have not captured the α-ketoglutarate in well-defined density, likely because the crystals are catalytically active. The determinants of α-keto acid specificity could be examined through mutagenesis coupled with additional structural studies. We proposed that amino acid position 153 (PaODH numbering) may play a role in selecting for pyruvate or α-ketoglutarate. Sa and YpODH have aspartate at this position while PaODH has an alanine. The ultimate test of such studies would be using primary sequence to predict substrate specficity. Y 243 stacks below the imidazole moiety of L-HisNA and is likely involved in substrate recognition and binding, but it is also positioned to act in catalysis though it has a much higher pKa than H219. Mutagenesis of each of these two residues would help distinguish their roles in the catalytic cycle. The high resolution possible with PaODH crystals along with the transient state kinetic assays we have developed for SaODH makes mutagenesis a feasible approach to further extend our understanding of substrate binding and catalysis. Finally, several bacterial species have a valine or aspartate substitution in place of F340 (F340 stacks above the imidazole of L-HisNA). These species may produce metallophores that do not contain histidine.

Bacteria, fungi and plants are vast reservoirs of unexplored biosynthetic diversity. Many secondary natural product pathways containing nicotianamine synthases or opine dehydrogenases exist. Most have a NAS followed by an ODH. In Firmicutes and some other gram-positive bacteria, a racemase homolog is found preceding the NAS. While the NAS followed by the ODH is the classic structure of opine metallophore producing operons, many variations exist. These variations are likely to encode unique opine metallophores as well as entirely new chemical entities. These pathways, detailed in Chapter 1, provide an excellent starting point for extending the analysis of either the nicotianamine synthase or opine dehydrogenase. I hope to read of progress in the study of both of these enzymes as I continue my academic career in years to come.

References

[1] Gi, M., Lee, K. M., Kim, S. C., Yoon, J. H., Yoon, S. S., and Choi, J. Y. (2015) A novel siderophore system is essential for the growth of *Pseudomonas aeruginosa* in airway mucus, *Sci Rep 5*, 1-15.